

M.Sc. Global Change Geography

Master Thesis

**Quantifying thaw subsidence
in a permafrost landscape
(Bayelva basin, Svalbard)**

Marie Rolf

Supervisors:

Prof. Dr. Julia Boike

Dr. Inge Grünberg

*Submitted to the
Department of Geography,
Humboldt-Universität zu Berlin*

Berlin, 02.04.2024

Quantifying thaw subsidence in a permafrost landscape (Bayelva basin, Svalbard)

Abstract

Rising temperatures have led to permafrost degradation throughout the Arctic. The melting of excess ground ice leads to a loss of structural support and consolidation of soils. As a consequence, the surface subsides seasonally when the active layer thaws, or long-term when the active layer deepens. Therefore, inter-annual thaw subsidence is an important metric for monitoring permafrost degradation. With temperature rise reaching twice the Arctic average, warming trends in Svalbard are particularly high, leading to severe impacts on permafrost conditions and periglacial landscapes. However, knowledge on subsurface permafrost changes in Svalbard is mostly limited to a few in-situ observations. In this study, I spatially expanded research on permafrost degradation by applying a two-fold approach to quantify thaw subsidence in the Bayelva basin, northwestern Svalbard. Firstly, I coregistered and differenced high-resolution digital elevation models (DEMs) for a period of more than 80 years (1936, 1995, 2008, 2010, 2019, and 2020). Secondly, during a field campaign in summer 2023, I measured Global Navigation Satellite System (GNSS) positions and calculated subsidence rates since a previous GNSS survey in 2019. In addition, I analysed how elevation change relates to landscape, terrain forms, vegetation cover, and timing of snow disappearance. Finally, I compared thaw subsidence in the Bayelva basin to the surrounding Brøgger peninsula. My findings show a clear elevation loss trend in the Bayelva basin that has persisted for decades and stretches across the entire study area. I found that periglacial terrain subsided at rates of -2.6 to -6.4 cm/year in DEM-based and -0.7 cm/year in GNSS-based analyses with larger subsidence during the 20th century than during recent observation periods. Within the periglacial landscape, I observed slightly larger subsidence in topographic depressions and for areas that are longer snow-covered. My study further suggests that the Bayelva basin is a representative subregion of the northern Brøgger peninsula as subsidence rates and patterns are generally similar. In this study, I demonstrated the challenges of thaw subsidence quantification in periglacial areas with a lack of stable reference terrain. At the same time, my results highlight the great potential of multi-temporal DEMs and repeated GNSS measurements for monitoring long-term elevation changes. This study represents a pioneering effort in the area, revealing ongoing subsidence in the Bayelva basin for the first time and indicating widespread ground ice loss, a process notoriously difficult to detect. I conclude that thaw subsidence is a crucial yet often underestimated component of permafrost landscapes in the warming Arctic.

Contents

1	Introduction	1
2	Study area	4
3	Methodology	6
3.1	Mapping general elevation change	6
3.1.1	Quantification of elevation change	6
3.1.2	Classification of landscapes	8
3.2	Mapping surface properties	8
3.3	Expansion to the Brøgger peninsula	8
4	Results	10
4.1	General elevation change in the Bayelva basin	10
4.2	Periglacial elevation change and surface properties	12
4.3	Periglacial elevation change on the Brøgger peninsula	14
5	Discussion	18
5.1	General elevation loss in the Bayelva basin	18
5.1.1	Thaw subsidence and ground ice loss	18
5.1.2	Thaw subsidence across time	19
5.1.3	Thaw subsidence in relation to other elevation loss processes	20
5.2	Thaw subsidence in relation to surface properties	21
5.2.1	Thaw subsidence in relation to topography and snow	21
5.2.2	Thaw subsidence in relation to vegetation	22
5.3	Thaw subsidence across the Brøgger peninsula	22
6	Conclusion	24
	Acknowledgement	25
	References	26
A	Extended methodology	34
A.1	Data basis	34
A.1.1	Satellite-based positioning data	34
A.1.2	Digital elevation models	35
A.1.3	Aerial imagery	37
A.1.4	Satellite imagery	37
A.1.5	Topographic data	37
A.2	Collection of GNSS data	37
A.2.1	Repeated measurements	38
A.2.2	Bedrock observations	38
A.2.3	Control points	38
A.3	Processing of GNSS data	38

A.3.1	Base data preparation	39
A.3.2	Post-processing and error correction	39
A.3.3	Validation	40
A.3.4	Implementation of quality flags	40
A.3.5	Differencing of repeated surveys	42
A.4	Processing of DEMs	43
A.4.1	Resampling	44
A.4.2	Coregistration	44
A.4.3	Differencing and vertical offset correction	46
A.4.4	Assessing the temporal component of change	46
A.5	Processing of satellite imagery	48
A.6	Landscape classification	48
A.7	Surface classifications	50
A.7.1	Terrain forms	50
A.7.2	Vegetation cover	51
A.7.3	Snow detection	52
A.8	Transfer to the surrounding Brøgger peninsula	53
B	Extended results	55
B.1	General elevation change results in the Bayelva basin	55
B.1.1	Quality of the 2019 DEM differencing results	55
B.1.2	Spatial distribution of GNSS-derived results	56
B.1.3	Comparison of DEM- and GNSS-derived elevation change results	57
B.1.4	Temporal component of general elevation change	58
B.2	Surface classifications in the Bayelva basin	60
B.2.1	Sample size per surface property class in the Bayelva basin . .	60
B.2.2	Simplification of terrain forms	60
B.2.3	Elevation change statistics across surface properties	61
B.3	Surface classifications on the Brøgger peninsula	65
B.3.1	Spatial distribution and coverage of the classes	65
B.3.2	Sample size per surface property class on the Brøgger peninsula	65
B.3.3	Elevation change statistics across surface properties	65

List of Figures

1	Location and dimensions of the study area	4
2	Elevation data sets	6
3	Annual elevation change across DEM differences and landscapes in the Bayelva basin	11
4	Comparison of GNSS and DEM differences	12
5	Comparison of periglacial elevation change and surface properties in the Bayelva basin	13
6	Annual elevation change across regions and landscapes on the Brøgger peninsula	15
7	Comparison of periglacial elevation change and surface properties on the Brøgger peninsula	17
A.1	Simplified methodological workflow	34
A.2	Schematic overview of the post-processed GNSS data sets	40
A.3	Schematic overview of the differencing and quality-flagging of repeated GNSS surveys	43
A.4	Visual and statistical comparison of coregistration algorithms	47
A.5	Schematic overview of overlapping and non-overlapping observation periods	48
A.6	SkySat imagery before and after manual georeferencing	49
A.7	Concept of Geomorphons by (Jasiewicz and Stepinski 2013)	51
B.1	Spatial patterns of general elevation change in the Bayelva basin	56
B.2	Spatial distribution of the repeated GNSS measurements	57
B.3	Temporal component of elevation change in the Bayelva basin	58
B.4	Sample size per surface property class in the Bayelva basin	60
B.5	Elevation change across terrain forms before simplification	61
B.6	Surface classification maps for the Brøgger peninsula	66
B.7	Sample size per surface property class on the Brøgger peninsula	67

List of Tables

A.1	Properties of the different DEMs	36
A.2	Positions of the GNSS reference stations	39
A.3	Validation of the GNSS measurements	41
A.4	Criteria of general quality flags for the GNSS measurements	42
A.5	Criteria of quality flags for repeated GNSS surveys	43
A.6	Overview of the aligned DEMs	46
A.7	Classification of snow cover disappearance	53
B.1	Statistics of general elevation change results in the Bayelva basin	55
B.2	Statistics of elevation change results at GNSS measurement locations in the Bayelva basin	57
B.3	Statistics of general elevation change results for non-overlapping time periods	59
B.4	Statistics of periglacial subsidence results across terrain forms in the Bayelva basin	62
B.5	Statistics of periglacial subsidence results for different vegetation in- dex values in the Bayelva basin	63
B.6	Statistics of periglacial subsidence results across snow disappearance classes in the Bayelva basin	64
B.7	Statistics of general elevation change results on the Brøgger peninsula	68
B.8	Statistics of periglacial subsidence results across terrain forms on the Brøgger peninsula	69
B.9	Statistics of periglacial subsidence results for different vegetation in- dex values on the Brøgger peninsula	70
B.10	Statistics of periglacial subsidence results across snow disappearance classes on the Brøgger peninsula	71

1 Introduction

Global warming induces widespread permafrost degradation and landscape changes throughout the Arctic. Permafrost, cryotic ground with temperatures at or below 0°C for at least two consecutive years (Van Everdingen 1998), underlays approximately 15 % of the exposed land area in the northern hemisphere (Obu 2021) with the majority located in polar regions. Permafrost temperatures are increasing and recently reached record high warming rates of roughly 0.3°C per decade (Biskaborn et al. 2019; IPCC SROCC Ch. 3.4.1.2.1, Meredith et al. 2019). All climate models and warming scenarios agree on further permafrost warming and thawing during the twenty-first century (IPCC AR6 WG2 Cross-Ch.6, Constable et al. 2022). Consequences of permafrost degradation are severe for humans and ecosystems on site and across the planet. Locally, thawing permafrost impacts topography, hydrology, and landscape stability increasing the likelihood of e.g. landslides, coastal erosion, and infrastructure damage (Philipp et al. 2021; Smith et al. 2021; Wolken et al. 2021). On a global scale, permafrost degradation accelerates climate change as unfrozen organic matter decays and releases carbon dioxide and methane, two major greenhouse gases (Smith et al. 2021). Worldwide, twice the amount of carbon is stored in permafrost as the carbon content of the atmosphere (Philipp et al. 2021). A profound understanding and monitoring of permafrost change is crucial to assess its impacts on climate and human-environment systems.

Periglacial landscapes are cold-climate but non-glaciated environments influenced by the freezing of soil (Ballantyne 2018). The depth and condition of permafrost in periglacial landscapes depends on environmental factors as the duration and magnitude of the winter freezing, physical properties of the ground material, the type of land cover, and the thickness of the insulating snow cover (Dobinski 2011). Permafrost is overlain by an active layer that is frozen in winter and thawed in summer (Van Everdingen 1998). The melting of ground ice in both permafrost and active layer induces a vertical movement of periglacial surfaces referred to as heave (upward) or subsidence (downward). When ground ice melts, the soil's volume reduces leading to cyclic elevation changes with the seasonal thawing and freezing of the active layer (Ballantyne 2018; Rouyet et al. 2021). Beyond its seasonality, the degradation of ground ice causes long-term surface subsidence as soil grains reorganise and pore volume reduces. The melting of ground ice that exceeds the pore space in the permafrost (excess ice) and the subsequent drainage of the released water further enhance this inter-annual subsidence trend (Ballantyne 2018; Cai et al. 2020). The degree of thaw-induced soil consolidation depends on the volume of excess ground ice, grain sizes, water permeability, and structural unity of the soil (Ballantyne 2018). Resulting spatial patterns are diverse ranging from the geographically distinct formations of thermokarst and patterned ground to landscape-wide subsidence. For the latter, Shiklomanov et al. (2013) introduced the term 'isotropic thaw subsidence' as widespread, gradual, and uniform subsidence phenomenon that is difficult to observe due to its slow but extensive character.

As a sub-surface feature, the state and evolution of permafrost is generally diffi-

cult to monitor. The only direct permafrost observations are ground temperatures measured in boreholes. However, the drilling of the borehole is associated with technical challenges and high costs limiting their availability in remote regions (Noetzli et al. 2021). Another sub-surface variable characterising permafrost conditions is thaw depth, often measured through mechanical probing (Boike et al. 2022). In-situ observations, limited to the research site, fall short of depicting spatial variations in permafrost degradation. To overcome this limitation, airborne and satellite-based remote sensing data have increasingly complemented in-situ measurements on a spatially extensive, relatively cheap and even up to circum-Arctic scale (Philipp et al. 2021). Remotely, permafrost can only be observed indirectly by focusing on land surface characteristics that accompany permafrost presence and degradation. Remote sensing studies from across the Arctic have derived permafrost properties from diverse variables such as surface moisture, lake areas, periglacial terrain structures, retrogressive thaw slumps, surface temperatures, seasonal ground displacements, vegetation cover dynamics, and coastal erosion rates (e.g. Epstein et al. 2012; Isaev et al. 2019; Kääb et al. 2014; Rey et al. 2019; Rouyet et al. 2021; Westermann et al. 2015; Witharana et al. 2022).

In addition, isotropic thaw subsidence can serve as valuable metric of long-term permafrost change. Often associated with the progressive deepening of the active layer into the ice-rich upper horizon of the permafrost (Liu and Larson 2018; Shiklomanov et al. 2013), subsidence observations can monitor top-of-permafrost ground ice loss in periglacial landscapes (Zwieback and Meyer 2021). Studies from across the Arctic used Interferometry Synthetic Aperture Radar (InSAR) (Antonova et al. 2018; Liu et al. 2010; Yu et al. 2024), Global Positioning System (GPS) (Shiklomanov et al. 2013; Streletskiy et al. 2016), reflective GPS (Liu and Larson 2018), digital elevation models (DEMs) (Günther et al. 2015; Oldenborger et al. 2022), and field equipment such as reference rods (Antonova et al. 2018) to detect these gradual decadal surface changes. Beyond its monitoring function, considering thaw subsidence is highly relevant when estimating the thickness and the deepening of the active layer as thaw depth measurements alone may underestimate actual thaw penetration (Antonova et al. 2018; O'Neill et al. 2023; Shiklomanov et al. 2013) and derived variables such as carbon release (Rodenhizer et al. 2020). In practice, however, it is often difficult to include subsidence when measuring thaw depth due to a lack of simple field methods and stable reference points (Boike et al. 2022).

The Arctic archipelago Svalbard is particularly affected by climate change. Mean annual air temperature increases of $1.7\text{ }^{\circ}\text{C}$ per decade since 1991 correspond to more than twice the Arctic and seven times the global average (Nordli et al. 2020). As a consequence, Svalbard experiences massive cryospheric changes in the form of glacial thinning and permafrost degradation (Boike et al. 2018; Christiansen et al. 2021; Geyman et al. 2022). While glacial mass loss has been studied on large scales (e.g. Geyman et al. 2022), permafrost research on Svalbard is generally smaller in scale and concentrated on few focus areas. At the long-term Bayelva permafrost observatory in northwestern Svalbard, measurements since 1998 show increasing soil and permafrost temperatures of $0.6\text{-}0.8\text{ }^{\circ}\text{C}/\text{decade}$ and $0.14\text{ }^{\circ}\text{C}/\text{decade}$, respectively

(Grünberg et al. under review) as well as a deepening of the active layer by approximately 1 m (Stern 2017). However, these clear indicators of permafrost degradation are limited to the research site and do not provide any information on its spatial variability.

In this study, I aimed at expanding observations on periglacial change beyond the Bayelva observatory to the surrounding Bayelva basin. I approached this aim by making use of the potential of isotropic thaw subsidence to monitor inter-annual ground ice loss in periglacial areas. Specifically, I addressed and discussed the following research questions (RQ):

- RQ1** How large is general elevation change in the Bayelva basin and how does elevation change vary spatially and temporally?
- RQ2** How does thaw subsidence relate to selected surface properties in periglacial areas of the Bayelva basin?
- RQ3** How does thaw subsidence in the Bayelva basin compare to periglacial areas of the surrounding Brøgger peninsula?

In a first step, I quantified general elevation change rates in the Bayelva basin based on multi-temporal DEMs and satellite-based positions (RQ1). I then classified landscapes to set a focus on periglacial areas and thaw subsidence (RQ1). I further investigated surface properties that potentially impact on or result from thaw subsidence and therefore mapped terrain forms, vegetation cover, and timing of snow disappearance in periglacial areas (RQ2). Finally, I transferred these analysis steps to the wider Brøgger peninsula to compare thaw subsidence in the Bayelva basin to its surrounding (RQ3).

2 Study area

The main focus area of my study was the Bayelva basin on the Brøgger peninsula in the northwest of Svalbard (Figure 1). The study area was centered on the Bayelva observatory (78.92102 °N, 11.83321 °E) (Figure 1d) - a long-term permafrost research site where multiple air, snow, soil, and permafrost parameters have been measured for up to 25 years (Boike et al. 2018; Grünberg et al. under review). In my research questions, I referred to three different spatial dimensions of the study area: 1) the Bayelva basin as the area along the Bayelva river between the Brøggerbreen glaciers in the south and the fjord in the north (RQ1) (yellow shaded area in Figure 1c), 2) the smaller Bayelva core area as the periglacial terrain surrounding the

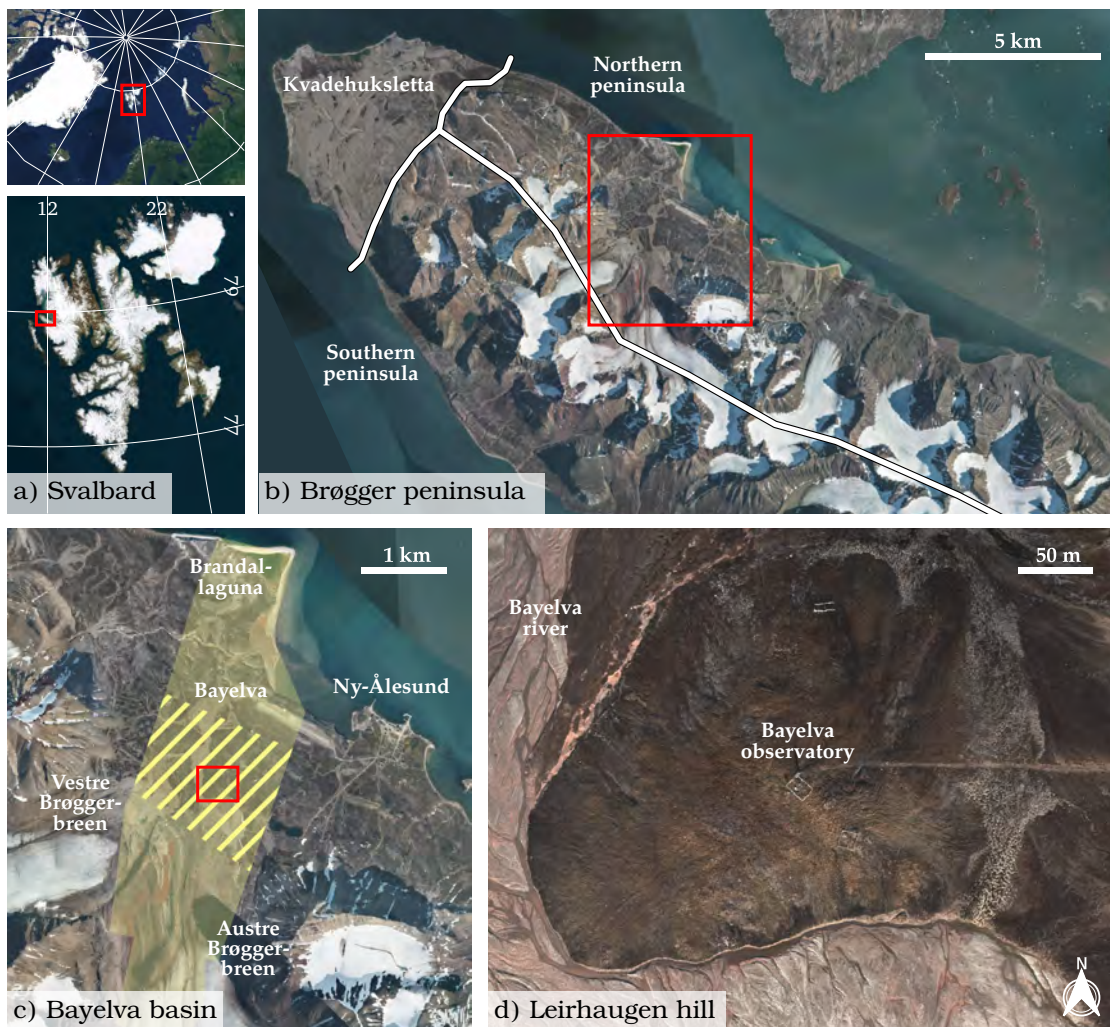


Figure 1: Location and dimensions of the study area - a) the Svalbard archipelago in the high-Arctic, b) the Brøgger peninsula in northwestern Svalbard, c) the Bayelva basin on the northern peninsula, and d) the Bayelva observatory on Leirhaugen hill in the center of the Bayelva basin. There were three spatial dimensions of the study area: 1) the Bayelva basin (yellow shaded area in c), 2) the Bayelva core area (yellow striped area in c), and 3) the wider Brøgger peninsula (b). The red frames mark the extent of the next smaller-scale subfigure. (Imagery: Bing Satellite, Norwegian Polar Institute (2014a)).

Bayelva observatory located on Leirhaugen hill (RQ1 and RQ2) (yellow striped area in Figure 1c), and 3) the wider Brøgger peninsula (RQ3) (Figure 1b).

Svalbard is a high-Arctic archipelago located midway between the northern coast of continental Norway and the North Pole (Figure 1a). Its polar tundra-climate is relatively warm for its latitude (74-81 °N) due to the influence of the West Spitsbergen oceanic current (Walczowski and Piechura 2011). About 60 % of Svalbard's land is covered by ice caps and glaciers partially calving into fjords. Ice-free terrain is mainly underlain by continuous permafrost with depths of about 100 m at the coasts and 500 m in the mountains (Humlum et al. 2003).

The Brøgger peninsula is located in the northwest of Svalbard's largest island Spitsbergen and is bordered by the Kongsfjord to the north and by the Forlandsundet to the west (Figure 1b). The Brøgger peninsula is characterised by mountain ridges with an elevation of up to 1000 m above sea level (a.s.l.). The steep mountain slopes are adjoined by gentle lowlands towards the coast with glacial and fluvial deposits. Active valley glaciers experience massive retreat and are only preserved in high elevations (Miccadei et al. 2016). The northwestern tip of the peninsula, the Kvadehuksletta, is characterised by a wide strandflat covered with marine sediments. Patterned ground features can be found throughout the periglacial lowlands and are particularly developed at the Kvadehuksletta (Kääb et al. 2014; Miccadei et al. 2016). Located at its northern coast, Ny-Ålesund is the only human settlement on the Brøgger peninsula and is considered the northernmost permanent community on Earth. It was founded as a coal mining village in the early 20th century and was then converted into an international research site in the 1980s (Paglia 2019).

With the term 'Bayelva basin', I refer to the surrounding of the Bayelva river west of Ny-Ålesund as marked in Figure 1c. Because of the study's data basis and research focus, this is not equivalent to the Bayelva watershed and rather focuses on the lower stream segment. The Bayelva basin stretches from the lower Austre Brøggerbreen glacier in the south to the Kongsfjord and the Brandallaguna in the north, mainly covering rocky moraines and hilly tundra lowlands. The southern and eastern watershed is underlain by red sandstone determining the brownish-red colour of the Bayelva river (Nowak and Hodson 2013).

The Bayelva observatory lies on Leirhaugen hill (25 m a.s.l.) at the center of the Bayelva basin (Figure 1d). The hill is half-enclosed by the Bayelva river and covered with sparse vegetation and patterned ground. Records from the Bayelva observatory show average air temperatures between -15 °C in late winter and +7 °C in summer. The annual precipitation of about 400 mm falls mainly as snow during the winter months (Boike et al. 2018). The snow cover partially persists until early July leading to snow cover duration of up to nine months. Maximal active layer thickness measurements range between 1 and 2 m and the recently measured mean permafrost temperature is -2.5 °C (Boike et al. 2018; Grünberg et al. under review). Climatic trends over the past 25 years show an increase in air, soil, and permafrost temperatures, active layer thickening, a lengthening of the thawing season, and a reduction in winter snow depth and snow cover duration at the Bayelva observatory (Grünberg et al. under review; Stern 2017).

3 Methodology

The following section summarises the methodological approach of my study (also outlined in Figure A.1). A detailed description of the data basis, data collection, and data processing can be found in appendix A. To analyse general subsidence trends in the Bayelva basin (RQ1), I quantified elevation change (Section 3.1.1) and compared different landscapes (Section 3.1.2). In order to assess the relation between subsidence and periglacial surface properties (RQ2), I classified terrain forms, vegetation cover, and snow disappearance timing in the Bayelva basin (Section 3.2). To finally compare periglacial subsidence trends in the Bayelva basin to its surrounding (RQ3), I extended the analysis to the Brøgger peninsula (Section 3.3).

3.1 Mapping general elevation change

3.1.1 Quantification of elevation change

I quantified elevation change in the Bayelva basin in a two-fold approach: 1) based on multi-temporal digital elevation models (DEMs) and 2) based on repeated satellite-based positioning surveys (Figure 2).

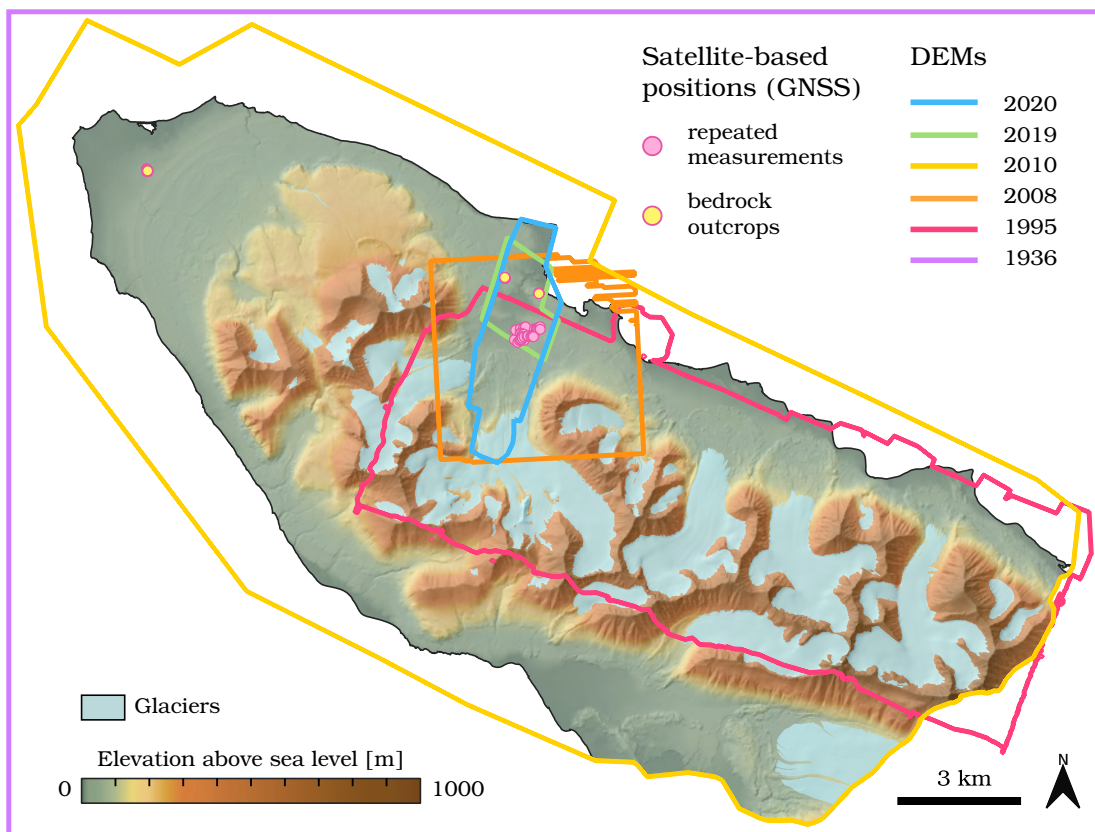


Figure 2: Elevation data sets - Location of repeated GNSS survey and GNSS bedrock measurements, as well as DEM extents that partially or fully cover the Bayelva basin (2008, 2019, and 2020 DEMs), the Brøgger peninsula (1995 and 2010 DEMs), and Svalbard (1936 DEM). Further information on the DEMs in Table A.1.

In the first approach, I used a set of multi-temporal DEMs to calculate landscape-wide elevation change. The DEMs covered a period of more than 80 years (1936, 1995, 2008, 2010, 2019, and 2020) and were generated from aerial stereo imagery (Section A.1.2). The flight campaigns took place during summer months and covered the Bayelva basin partly or fully (Figure 2). The six multi-source DEMs (Boike et al. 2018; Geyman et al. 2022; Norwegian Polar Institute 2014a) differed in coverage, spatial resolution, and coordinate reference system (Table A.1). In order to compare the DEMs to each other, I therefore first resampled all DEMs to the extent, pixel size, and coordinate system of the reference DEM (Section A.4.1). I chose the 2020 DEM (approx. 7 km² large) as reference for RQ1 and RQ2 as it was the most recent, had the highest spatial resolution (0.15 m/pixel), and covered the Bayelva basin from the Brøgger glaciers to the coast. I removed potential shifts, tilts, and rotations between the DEMs by aligning the resampled to the reference DEM using the xDEM tool (xDEM contributors 2021) (Section A.4.2). Statistical coregistration algorithms aim at minimising elevation residuals between two DEMs for terrain that is assumed to be stable. However, due to glacial, fluvial, and periglacial processes, stable terrain is generally rare in the Bayelva basin. I therefore only excluded terrain of major change (e.g. glaciers, moraines, river beds) but kept periglacial areas in the terrain mask for coregistration. I tested several statistical coregistration algorithms (Section A.4.2) and found the Nuth and Kääb algorithm (Nuth and Kääb 2011) to perform best according to its stable terrain residuals (Figure A.4). I applied the Nuth and Kääb algorithm to all DEMs and only combined it with a tilt algorithm for the 2010 DEM for better performance (Table A.6). To correct for any remaining vertical shifts, I calculated median offsets at GNSS-surveyed bedrock outcrops (Section A.2.2) and adjusted the aligned DEMs accordingly (Section A.4.3 and Table A.6). I finally subtracted the aligned and offset-corrected DEMs from the reference DEM (Section A.4.3) and calculated annual averages to compare elevation change results across DEMs. The final results referred to annual averages of cumulative elevation changes for the whole period between aligned and reference DEM (1936-2020, 1995-2020, 2008-2020, 2010-2020, and 2019-2020). To further assess the temporal component of change, I subsetted the DEM differences into three non-overlapping time periods that covered ten years or more (1936-1995, 1995-2010, and 2010-2020) (Section A.4.4 and Figure A.5).

In the second approach, I collected three-dimensional positioning data based on satellite signals from the Global Navigation Satellite System (GNSS) network. In summer 2023, I repeated elevation measurements in periglacial terrain from an earlier field campaign in 2019 (Lange et al. 2020) with a GNSS receiver (Section A.2). In addition, I surveyed control points and bedrock outcrops for later validation and offset corrections (Figure 2, Section A.2.2). I then used GNSS reference data from two permanent base stations at the Ny-Ålesund airport (Geoforschungszentrum n.d.; International GNSS Service n.d.) to correct the GNSS measurements for atmospheric disturbances (Sections A.3.1-A.3.2). I validated my post-processed positions using control point coordinates from the local mapping authority Kartverket (<https://www.kartverket.no/>) (Section A.3.3). To quantify elevation change at the

survey locations, I subtracted elevation measurements from the two repeated GNSS surveys (Section A.3.5). In order to filter low-quality measurements, I implemented quality flags for both the post-processing quality and the accuracy of the repeated measurement (Sections A.3.4-A.3.5).

3.1.2 Classification of landscapes

I analysed spatial variations in elevation change by comparing change rates in different landscapes. The Norwegian Polar Institute (2014b) provided vector data representing the outlines of glaciers, moraines, river beds, and water bodies in 2010 (Section A.1.5). I visually inspected aerial imagery and DEMs from 2010 and 2020 to furthermore identify mountains with steep and rocky slopes and areas under anthropogenic influence (i.e. the surroundings of buildings, roads and the airport runway around Ny-Ålesund). Through spatial differencing, I finally classified the remaining lowlands as periglacial landscape (Section A.6). To examine spatial patterns of general elevation change in the Bayleva basin, I sampled elevation change results and landscape class at 10000 random point locations across the footprint of the 2020 reference DEM.

3.2 Mapping surface properties

I focused on periglacial areas to further analyse the relation between elevation change and three surface properties: terrain forms, vegetation cover, and timing of snow disappearance (Section A.7). First, I applied the Geomorphons tool (Jasiewicz and Stepinski 2013) to the 2010 DEM to divide the periglacial terrain into six classes (peak/ridge, shoulder/spur, hollow/footslope, valley/pit, slope, and flat) (Figure A.7, Section A.7.1). Second, I estimated the density and productivity of periglacial vegetation cover by calculating the Normalized Difference Vegetation Index (NDVI) from a SkySat image (Planet Labs PBC 2023) from mid summer 2023 (08.08.2023) (Section A.7.2). Third, I detected snow cover on SkySat images from late spring and early summer 2023 (26.05., 06.06., 21.06., and 04.07.2023) using a blue band thresholding approach and mapped the approximate timing of snow cover disappearance (very early, early, medium, late, very late) by stacking the multi-temporal snow cover maps (Section A.7.3). The SkySat imagery featured a spatial resolution of 0.5 m and consisted of three visual (blue, green, red) and one near-infrared band (Section A.1.4). For the statistical analysis, I extracted elevation change, terrain form class, vegetation cover, and timing of snow disappearance for 5000 random sample points in the periglacial Bayelva core area (Figure 1c, Section A.7).

3.3 Expansion to the Brøgger peninsula

I extended both, the quantification of elevation change and the classification of landscapes and surface properties, to the wider Brøgger peninsula (Section A.8). To

quantify elevation change, I aligned the Svalbard-wide 1936 DEM to the peninsula-covering 2010 DEM with a spatial resolution of 5 m/pixel (approx. 280 km² in size). I used topographic data, aerial imagery, the 2010 DEM and SkySat images from 2023 to classify landscapes, terrain forms, vegetation cover, and snow disappearance timing in accordance with the classification methods applied to the Bayelva basin in Sections 3.1.2 and 3.2. Data gaps in the SkySat imagery due to cloud cover and varying illumination, slightly limited the spatial coverage of vegetation cover and snow disappearance mapping (Figure B.6).

Due to low image qualities in 1936, I excluded the southern part of the peninsula from the analysis and divided the remaining peninsula into two regions: 1) The Kvadehuksletta at the tip of the peninsula encompassing flat terrain, little vegetation, and vast patterned ground, and 2) the northern peninsula characterised by hilly and mountainous landscapes with moraines and glaciers (Figures 1 and 6). I compared both regions to the Bayelva basin as a subregion of the northern peninsula. For the statistical analysis, I sampled elevation change, and landscape in the Bayelva basin (10000 random points in the Bayelva basin and 10000 random points on the northern peninsula and Kvadehuksletta together) and periglacial elevation change, terrain form class, vegetation cover, and snow disappearance timing in the Bayelva core area (5000 random points in each of the three regions) (Section A.8).

4 Results

The following section summarises my key findings and visualises elevation change results as maps, violin plots and box plots. Average elevation change rates are reported as mean values plus/minus (\pm) the standard deviation as uncertainty range. Violin plots range from the minimum to the maximum value and show the interquartile range (dotted line) and the median (dashed line) values. The width of each violin depicts the data’s frequency. Box plots mark the median (horizontal line), the interquartile range (coloured box), and the 1.5 times extended interquartile range (whiskers). For the sake of clarity, I omitted outliers from the box plots. Appendix B includes extended results such as tables with detailed statistical parameters and complementing figures on the spatial distribution of the observed changes.

4.1 General elevation change in the Bayelva basin

I obtained DEM- and GNSS-derived elevation change results. Positive values indicated elevation gain through e.g. surface heave, material deposition or construction of objects. Negative values indicated elevation loss through e.g. surface subsidence, erosion, mass movements or glacial retreat.

DEM differencing resulted in overall negative elevation change rates between the aligned and the reference dates that varied spatially throughout the Bayelva basin. Within the same landscape, annual elevation change results from the different DEMs generally agreed on the order of magnitude (Figure 3 and Table B.1). Periglacial areas exhibited negative elevation change rates (-2.6 ± 1.7 to -6.4 ± 5.8 cm/year) comparable to those of river beds (-2.3 ± 1.6 to -10.1 ± 5.8 cm/year) and anthropogenic areas (-0.5 ± 11.4 to -2.7 ± 3.1 cm/year). Elevation loss was much larger for moraines (-20.9 ± 35.3 to -32.6 ± 41.4 cm/year) and glaciers (-119.0 ± 7.6 to -220.5 ± 33.9 cm/year).

I observed temporal variations in DEM differences within the same landscape (Figure 3 and Table B.1). Within periglacial landscapes and river beds, negative elevation change rates were stronger for 1936-2020 (-6.4 ± 5.8 and -10.1 ± 5.8 cm/year respectively) than for later observation periods ($\geq -2.6 \pm 1.7$ and $\geq -2.3 \pm 1.6$ cm/year respectively). In anthropogenic areas, the number of samples that experienced elevation gain and the maximum elevation change rate increased from -15.6 cm/year (1936-2020) to -149.9 cm/year (2010-2020). Visual inspection of elevation change maps and aerial imagery showed that the resulting net elevation gain rates of up to -15 m were mainly related to the construction of roads and buildings in the respective period. Since 1995, temporal variations were low for moraines. As the moraine area was still partly glacier-covered in 1936, this time step had to be excluded. Within the current glacier outline, elevation loss increased from -119.0 ± 7.6 (1936-2020) to -220.5 ± 33.9 cm/year (2010-2020). These observed temporal patterns of elevation change across landscapes were generally similar when subsetting the observation periods into 1936-1995, 1995-2010, and 2010-2020 (Figure B.3) instead of always comparing to the reference of 2020 and are further described in Section B.1.4.

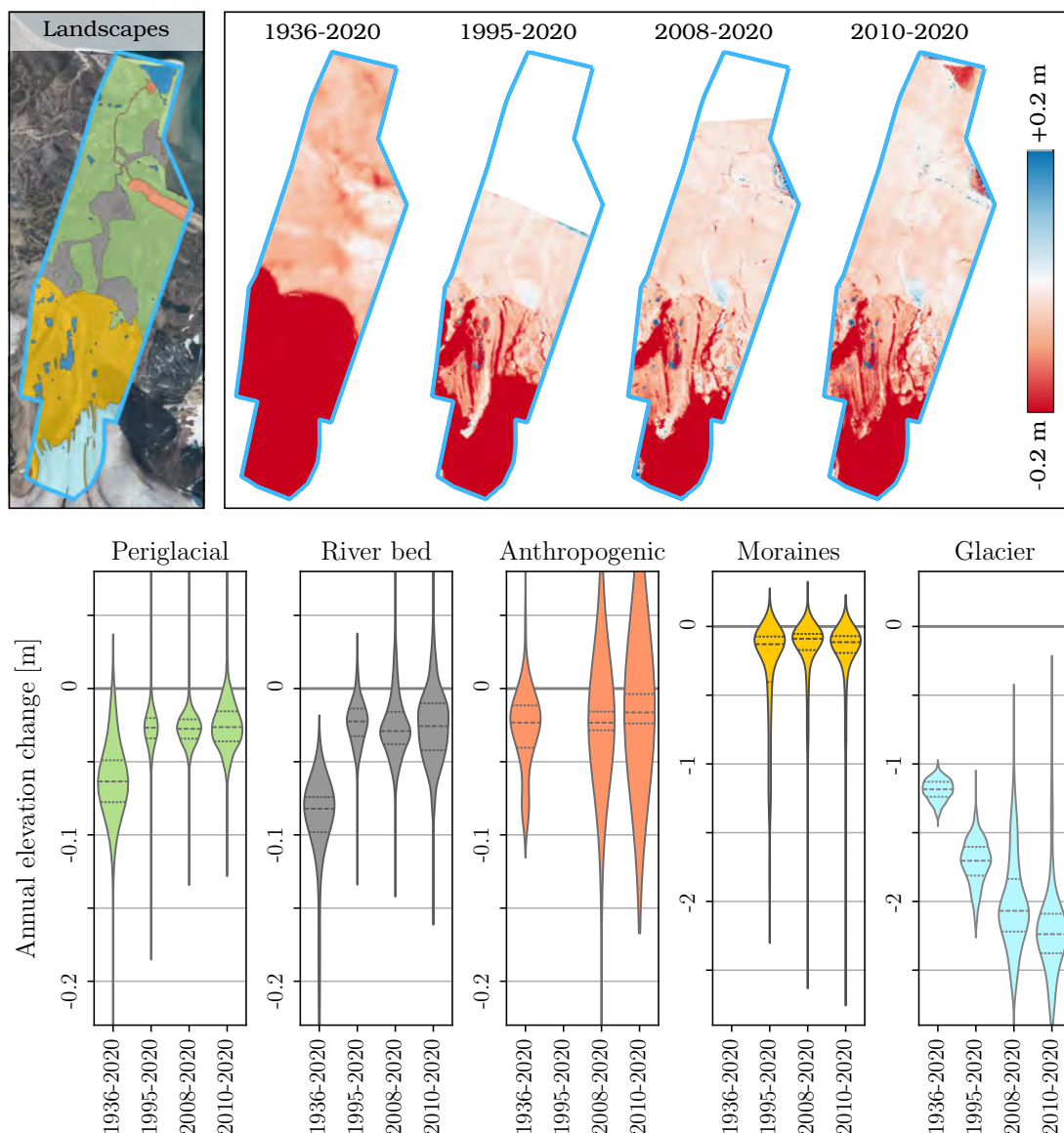


Figure 3: Annual elevation change across DEM differences and landscapes in the Bayelva basin - Landscape classification for the footprint of the 2020 reference DEM (left map), annually averaged DEM differences for each observation period (right maps), and sampled elevation change rates grouped by landscape class (violin plots). Elevation change was calculated from multi-temporal DEMs (1936, 1995, 2008, 2010, and 2020). Please note that in 1936 glaciers covered parts of the current moraine area and the moraine changes are therefore excluded at this time frame. (Landscape classification based on Norwegian Polar Institute (2014b), Aerial imagery and DEMs: Boike et al. (2018); Geyman et al. (2022); Norwegian Polar Institute (2014a), as well as unpublished DEMs by AWI, DLR, NORCE, and NPI).

Building on the DEM-based spatial differencing analysis of the Bayelva basin, I further investigated elevation change using 39 repeated GNSS measurements of high surveying and processing quality. All measurements were located in periglacial terrain around Leirhaugen hill and therefore in the immediate surrounding of the Bayelva observatory (Figure B.2). The general GNSS-derived elevation change trend was slightly negative between 2019 and 2023 with an average of -0.7 ± 0.8 cm/year

and values ranging from -2.9 to 0.7 cm/year (Figure 4 and Table B.2).

The comparison of both quantification methods showed larger surface elevation loss in DEM- than in GNSS-derived results (Figure 4 and Table B.2). Average elevation change rates were -2.0 cm/year (2010-2020) to -5.0 cm/year (1936-2020) more pronounced than the GNSS-derived average, resulting in a four- to eight-fold negative elevation trend. The 2019-2020 DEM difference was much more scattered than DEM differences for other periods (Figure 4) and therefore had to be excluded (Section B.1.1).

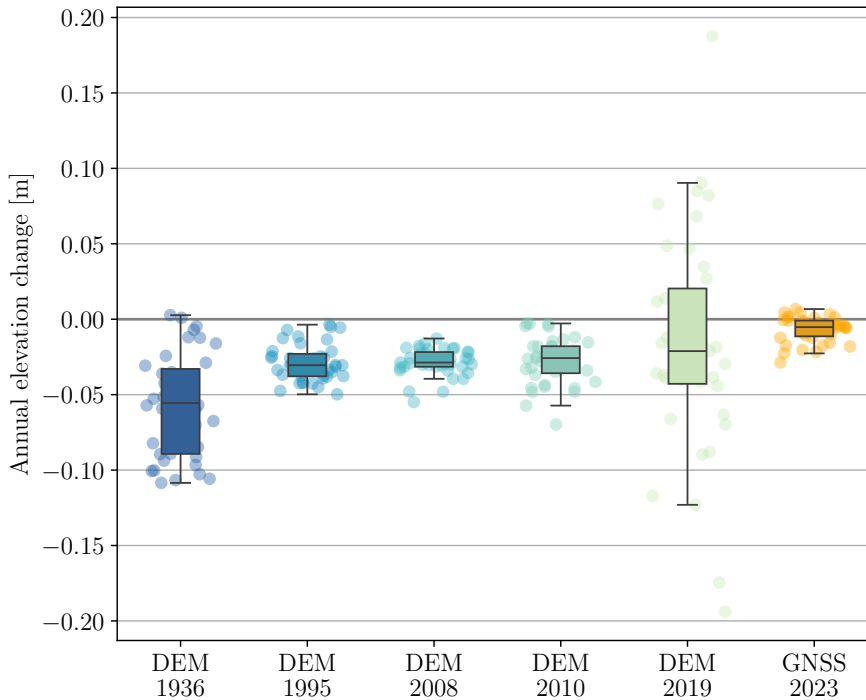


Figure 4: Comparison of GNSS and DEM differences - Annually averaged elevation change results for the DEM differences at GNSS measurement locations in blue (compared to the 2020 reference DEM) and for the repeated GNSS survey in orange (difference from 2019 measurements).

4.2 Periglacial elevation change and surface properties

I observed widespread elevation loss in periglacial landscapes in the Bayelva basin that varied spatially in magnitude with the surface’s properties. I found terrain forms, vegetation cover, and timing of snow disappearance to be partially connected to the rate of elevation change in the periglacial DEM core area of the Bayelva basin (Figure 5). In the following, I refer to negative elevation changes in periglacial areas as subsidence and to positive changes as heave due to prevailing periglacial processes.

The surface properties were unevenly distributed throughout the Bayelva core area (Figure 5 and Section B.2.1). Among the six terrain form classes, slope was the most widespread (32 %) and valley the rarest (4 %), while ridge, shoulder, slope, and footslope covered medium areas (9-16 %) (Table B.4). NDVI values were mainly

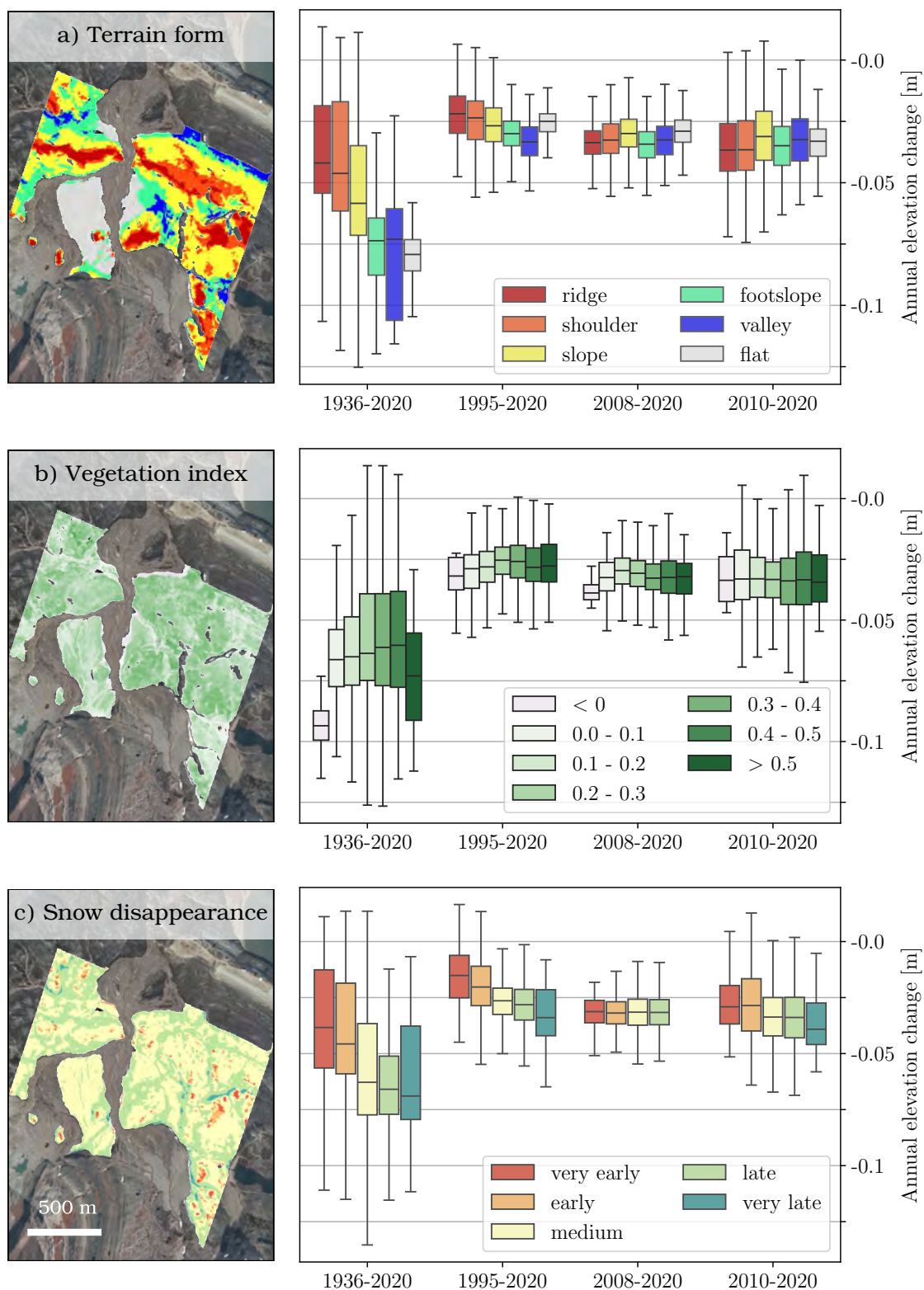


Figure 5: Comparison of periglacial elevation change and surface properties in the Bayelva basin - Surface classification in the periglacial terrain of the Bayelva core area (left maps) and annually averaged elevation change results from four observation periods (right box plots) sampled for random points within a) terrain forms, b) NDVI bins, and c) snow disappearance timings. (Terrain forms based on Jasiewicz and Stepinski (2013) and Norwegian Polar Institute (2014a), NDVI and snow cover derived from Planet Labs PBC (2023)).

positive with a peak at 0.2-0.4 (49 %) indicating photosynthetic activity and hence vegetation cover. Negative NDVI values (e.g. for water areas) and high NDVI values (>0.5) were hardly present (≤ 1 %) (Table B.5). Medium (48 %) and late (34 %) snow disappearance timing prevailed while only few patches experienced very early, early or very late snow disappearance (1-3 %) (Table B.6).

In earlier periods (since 1936 and since 1995), I observed a tendency towards less subsidence at protruding terrain forms (ridges and shoulders) than in topographic depressions (valleys and footlopes) (Figure 5a). Ridges experienced average subsidence of -3.8 ± 2.4 cm/year in 1936-2020 and -2.1 ± 1.4 cm/year in 1995-2020 while valleys subsided with -7.9 ± 2.5 cm/year and -3.3 ± 0.9 cm/year respectively (Table B.4). This spatial pattern did not apply to terrain forms in 2008-2020 and 2010-2020. Variance was generally higher within than among terrain form classes in 1995-2020, 2008-2020, and 2010-2020. Only for 1936-2020, the interquartile ranges of ridges and shoulders on the one and valleys and footslopes on the other side did not overlap (Figure 5a). While subsidence rates in 1936-2020 were comparable to later observation periods at ridges (-2.1 to -3.8 cm/year) and shoulders (-2.4 to -4.3 cm/year), subsidence was about -5 cm/year more pronounced in valleys and at footslopes.

I found only marginal relationships between vegetation cover and subsidence of the periglacial surface. For all observation periods, within-class variance was much larger than among the NDVI bins (Figure 5b). In 1936-2020, subsidence was slightly larger in areas without vegetation (-6.2 ± 2.6 cm/year for NDVI of 0-0.1 compared to -5.9 ± 2.7 cm/year for NDVI of 0.4-0.5) and for areas with relatively high vegetation density (-7.3 ± 2.4 cm/year for NDVI >0.5) (Table B.5).

My observations further indicate that periglacial areas subsided slightly more when they were longer covered by snow (Figure 5c). In 1936-2020, 1995-2020, and 2010-2020, subsidence rates were lower for very early (-3.6 ± 2.9 , -1.2 ± 2.0 , and 2.6 ± 1.8 cm/year, respectively) than for very late snow disappearance timing (-6.4 ± 2.7 , -3.2 ± 1.9 , and -4.2 ± 3.0 cm/year, respectively) (Table B.6). Within-class variance was generally higher than between-class variance for snow disappearance timing (Figure 5c). In 2008-2020, average subsidence rates were consistent among very early to late snow disappearance classes (-3.1 to -3.2 cm/year) (Table B.6). Due to the influence of remaining snow patches on the 2008 DEM, I excluded the ‘very late’ class for 2008-2020.

4.3 Periglacial elevation change on the Brøgger peninsula

Beyond the Bayelva basin, the wider Brøgger peninsula also experienced widespread elevation loss since 1936 with spatial variations across landscapes and surface properties. I compared observed elevation changes (1936-2010) at the Kvadehuksletta, the northern peninsula, and the Bayelva basin to each other. I considered Bayelva a subregion of the northern peninsula that covered the whole footprint of the 2020 DEM for landscape analyses and only the periglacial core DEM area for comparisons across surface properties.

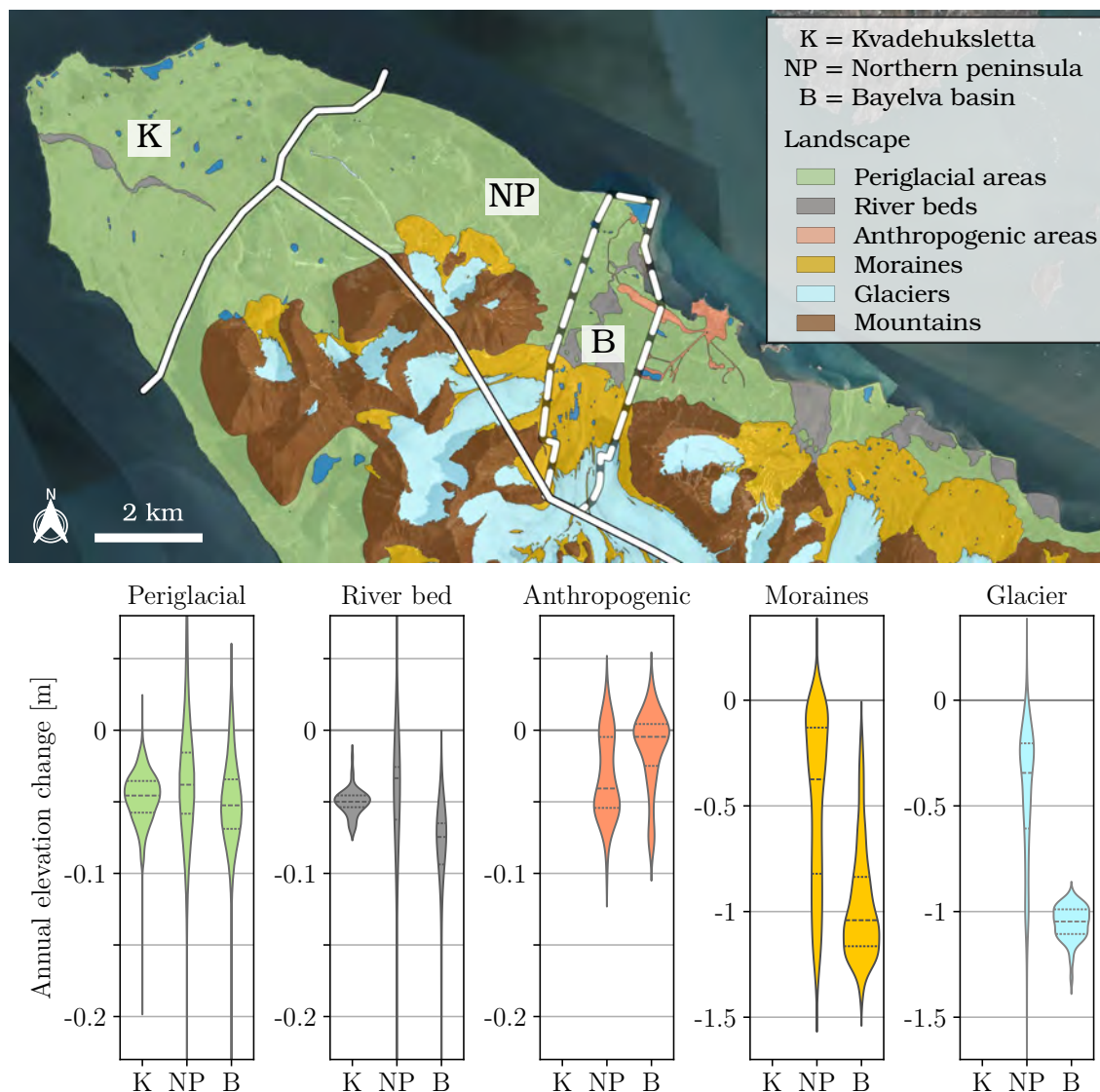


Figure 6: Annual elevation change across regions and landscapes on the Brøgger peninsula - Landscape classification for the footprint of the 2010 reference DEM (top) and annually averaged elevation change rates (1936-2010) for random samples grouped by landscape class (bottom). Subsetted into the three regions Kvadehuksletta (K), northern peninsula (NP), and Bayelva (B, footprint of the 2020 DEM). (Landscape classification based on Norwegian Polar Institute (2014b)).

I found the Bayelva basin to feature similar landscape characteristics as the rest of the northern peninsula while differing remarkably from the Kvadehuksletta. Periglacial landscapes prevailed non-steady land areas in all regions (45% of the Bayelva basin, 38% of the northern peninsula, and 98% of the Kvadehuksletta). The Kvadehuksletta furthermore encompassed one river while the Bayelva basin and the northern peninsula were both characterised extensively by glaciers (10% and 32%), moraines (32% and 25%), and river beds (11% and 5%). Anthropogenic areas were limited to the village of Ny-Ålesund and its surrounding making up 3% of the Bayelva basin and 1% of the northern peninsula (Figure 6 and Table B.7).

For 1936-2010, I observed negative elevation change trends in all regions and

landscapes (Figure 6). The average elevation loss rates of periglacial areas and river beds in the Bayelva basin (-5.7 ± 6.6 cm/year and -10.0 ± 7.5 cm/year) were slightly stronger than those on the northern peninsula (-4.2 ± 10.2 cm/year and -6.1 ± 10.7 cm/year) and the Kvadehuksletta (-4.7 ± 1.7 cm/year and -5.0 ± 0.9 cm/year) (Table B.7). In these landscapes, the spread of the elevation change observations was particularly large on the northern peninsula (indicating relative heterogeneity) and small on the Kvadehuksletta (indicating relative homogeneity) (Figure 6). Anthropogenic areas on the northern peninsula (i.e. all of Ny-Ålesund and its surrounding) showed average elevation loss rates that were on average -2.1 cm/year more pronounced than in the subregion of the Bayelva basin only (i.e. mainly the airport). The classified moraines on the northern peninsula were ice-free in 2010 but mostly still glaciated in 1936. For these proglacial areas and the bordering glaciers, I observed elevation loss rates of -96.6 ± 26.6 cm/year and -105.5 ± 8.1 cm/year in the Bayelva basin but only -48.5 ± 39.7 cm/year and -43.4 ± 31.3 cm/year on the northern peninsula indicating that the Austre Brøggerbreen was changing at higher rates than other glaciers (Figure 6 and Table B.7).

Within the periglacial landscape on the Brøgger peninsula, surface properties were spatially unevenly distributed (Figure B.6 and B.7). While the Kvadehuksletta encompassed predominantly flat terrain (43%), slopes predominated on the northern peninsula (49%) and in the Bayelva basin (38%). The periglacial terrain on the Kvadehuksletta was generally less vegetated (84% with NDVI < 0.2) and featured earlier melting of the last snow patches (95% with medium or earlier snow disappearance timing) than the northern peninsula. In the Bayelva basin, vegetation appeared to be slightly denser (75% with NDVI > 0.2) than on the northern peninsula (42% with NDVI > 0.2). Snow disappearance timing was mostly focused on the medium and late class in the Bayelva basin (95%), while all classes on the northern peninsula encompassed at least 9% of the periglacial area (Figure B.7 and Table B.10).

I observed spatial variations in periglacial surfaces subsidence (1936-2010) that were comparable for the Bayelva basin and the northern peninsula while differing slightly on the Kvadehuksletta (Figure 7). Both Bayelva basin and northern peninsula showed a tendency towards larger subsidence rates for topographic depressions (-6.9 ± 2.8 and -7.7 ± 13.2 cm/year for valleys) than for protruding terrain forms (-2.2 ± 2.9 and -2.1 ± 8.2 cm/year for ridges) (Table B.8). Likewise, periglacial areas that were longer snow-covered showed slightly more subsidence in both regions (-1.7 ± 3.0 and -3.5 ± 7.4 cm/year for very early, -5.0 ± 2.6 and -4.9 ± 7.8 cm/year for ridges) (Table B.10). However, the variance was generally higher within than among terrain form and snow disappearance classes. Subsidence rates on the Kvadehuksletta were consistent across terrain forms and snow disappearance timings. My observations furthermore suggest a possible tendency towards lower subsidence rates for vegetation-poor areas than for denser vegetation covers which is most pronounced on the Kvadehuksletta and barely present in the Bayelva basin (Figure 7).

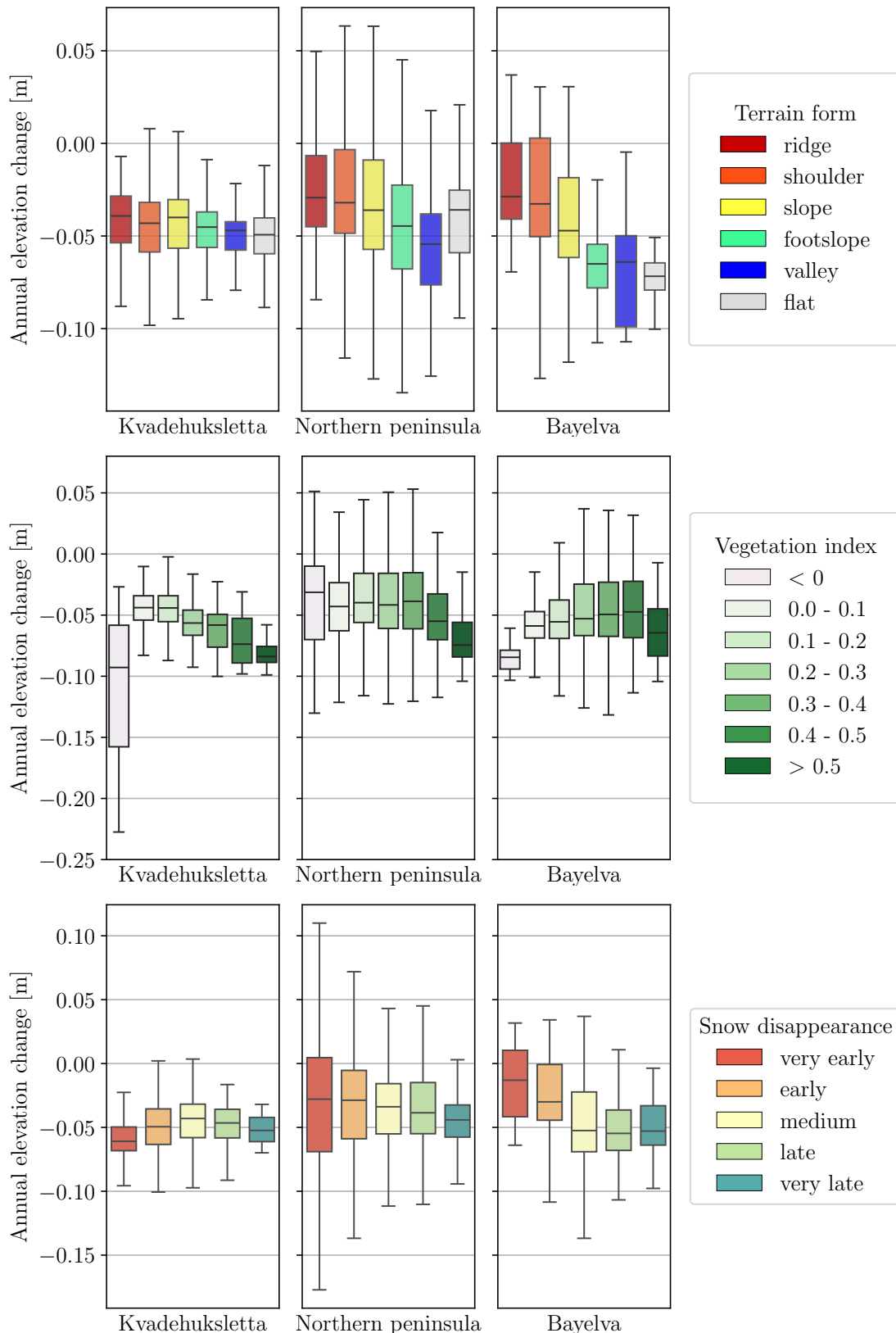


Figure 7: Comparison of periglacial elevation change and surface properties on the Brøgger peninsula - Annually averaged elevation change results (1936-2010) compared to surface properties using randomly sampled points within terrain forms (top), NDVI bins (center), and snow disappearance timings (bottom). Subsetted into the regions Kvadehuksletta, northern peninsula, and Bayelva (periglacial core DEM area). (Terrain forms based on Jasiewicz and Stepinski (2013) and Norwegian Polar Institute (2014a), NDVI and snow cover derived from Planet Labs PBC (2023)).

5 Discussion

5.1 General elevation loss in the Bayelva basin

In this study, I detected a general negative elevation change trend throughout the Bayelva basin with variations across observation periods and landscapes (RQ1, Section 4.1). Subsidence in periglacial terrain was on average more pronounced in DEM-derived (-2.6 to -6.4 cm/year) than in GNSS-derived results (-0.7 cm/year) (Figures 3 and 4).

Scientific literature reports subsidence rates over permafrost across the Arctic that are generally lower yet comparable to my findings. Chen (2019) used InSAR to detect subsidence rates of -0.3 to -0.5 cm/year (1995-2009, 2015-2019) in the Bayelva catchment. Another InSAR study found similar rates of -0.2 cm/year (2018-2021) in mid-western Spitsbergen (Yu et al. 2024). Studies from northern Alaska observed sub-centimeter subsidence rates (2001-2015) using InSAR (Liu et al. 2010) and GPS (Liu and Larson 2018; Shiklomanov et al. 2013; Streletskiy et al. 2016). Antonova et al. (2018) used InSAR and reference rods to detect -2 cm/year (2013-2017) of subsidence in the Lena delta. As the compilation of these studies shows, InSAR is a frequently used method to detect thaw subsidence. However, InSAR studies also highlight the challenges of e.g. atmospheric effects, soil moisture impacts on radar penetration, availability of reference points on the ground, and a potential loss of coherence on multi-year time spans (Antonova et al. 2018; Liu et al. 2010). Antonova et al. (2018) therefore propose DEM differencing as promising alternative for long-term subsidence monitoring. In fact, a DEM differencing study from the Siberian island Muostakh (Günther et al. 2015) reports much larger subsidence rates of -5.8 cm/year (1951-2013) which are in agreement with my observations from an historic DEM (-6.4 cm/year for 1936-2020).

The fact that differences from multiple DEMs in this study agreed on the general magnitude of change underlines the plausibility of my results. Unfortunately, a sophisticated validation was, due to the lack of ground truth data, not possible. The acquisition of direct in-situ subsidence measurements at fixed locations (e.g. reference rods or heave sleeves that are drilled and anchored in the permafrost) may complement and validate DEM- and GNSS-observations in the future.

5.1.1 Thaw subsidence and ground ice loss

Despite small-scale variations, the observed subsidence trend of the periglacial surface ranged over the entire study area (Figure 3). This ‘isotropic thaw subsidence’ (Shiklomanov et al. 2013) is commonly associated with the gradual loss of top-of-permafrost ground ice (Zwieback and Meyer 2021). Against this background, my observations are in accordance with active layer monitoring (1998-2023) at the Bayelva observatory indicating increases in soil temperatures with a stronger warming at the bottom of the active layer and trends towards an earlier thawing and a later freezing of the active layer (Grünberg et al. under review). Both soil warming and lengthening of the thawed period in the Bayelva basin foster a progressive deep-

ening of the active layer into the ice-rich transition horizon (Liu and Larson 2018). Stern (2017) modelled an active layer deepening of roughly 1 m since 1998 at the Bayelva observatory.

The ground ice content influences the subsidence potential of periglacial ground. Cable et al. (2017) analysed the ice content of frozen sediment cores from central Spitsbergen and found average subsidence potentials of 10-30 cm (maximum of 65 cm) per meter of active layer thickening. At the Bayelva basin, I found net subsidence of approximately -75 cm (1995-2020), while the active layer deepened by about 1 m (Stern 2017). These observations suggest a relatively high subsidence potential and thus excess ground ice content in the Bayelva basin compared to the findings by Cable et al. (2017). However, it is important to keep in mind that active layer thickness measurements and modelling could remarkably underestimate actual thaw penetration when not accounting for subsidence in the first place (Shiklomanov et al. 2013). Building on my study, future research may combine surface subsidence with active layer thickness measurements and sedimentary information to estimate and map landscape-wide ground ice content in the Bayelva basin.

5.1.2 Thaw subsidence across time

My study highlights the great potential of historic DEMs to quantify decadal-scale changes in permafrost landscapes as previously shown by e.g. Günther et al. (2015). For multi-decadal observation periods, as referred to in this study, a single DEM difference cannot depict elevation changes in great detail. However, historic DEMs allow for a broad estimation of ground ice changes in the 20th century when both subsurface and surface observations in the Arctic were rare.

My observations indicate that excess ground ice loss in the Bayelva basin was more pronounced during the 20th century than during the last three decades. Within periglacial areas, I found subsidence rates since 1936 that were -4 cm/year stronger than for observations after 1995 (Figures 3 and B.3). At first sight, this seems to be in contrast to long-term climate observations at Svalbard showing a strong warming trend of 1.7 °C/decade since 1991 (Nordli et al. 2020). Despite this recent trend, however, Svalbard already experienced a particularly warm period in the 1930s and 1950s (Isaksen et al. 2022) that could potentially trigger high thaw subsidence rates captured by the 1936 DEM differences. As recent warming is, nevertheless, stronger and longer lasting than the early 20th century warming (Isaksen et al. 2022; Nordli et al. 2020), I assume that air temperatures alone fail to explain temporal developments of thaw subsidence rates. Cable et al. (2017) for instance, show how ground ice content is strongly determined by cryostructure, water availability, and sedimentary history of permafrost layers. Larger subsidence rates during the 20th century may potentially be explained by an early thawing of a particularly ice-rich horizon that was underlain by permafrost layers with a lower ice content leaving less subsidence potential in recent decades.

I observed weaker ground subsidence in the Bayelva basin within the last five years. For 2019-2023, I detected subsidence rates of -0.7 cm/year based on re-

peated GNSS measurements, while earlier DEM differences showed four- to eight-fold stronger subsidence rates (Figure 4). These variations may potentially result from differences in observation methods (e.g. point- vs. pixel-based elevation data). However, Grünberg et al. (under review) show a reduced soil warming trend at the Bayelva observatory since 2010, which supports and potentially explains the weakening of subsidence rates in recent years.

The DEMs used in this study were derived from stereo images with different observation dates during the summer (Table A.1). Temporal offsets potentially introduced a bias due to seasonal elevation changes with the freezing and thawing of the active layer. An InSAR study detected average ground displacement maxima of about 2 cm within one summer with high spatial variability in the Bayelva basin (Rouyet et al. 2021). Subsidence rates were reported to be highest during an initial thawing period from mid-June to early July and reversed to surface heave at the beginning of October. However, as surfaces were observed to be relatively stable between mid-July and mid-September (Rouyet et al. 2019, 2021), when the elevation observations of this study were made, I expect the seasonal influence on my results to be marginal. With the installation of direct and automated subsidence measurements, future research could measure both seasonal and inter-annual surface changes and reduce the uncertainty of temporal offsets between elevation data sets.

5.1.3 Thaw subsidence in relation to other elevation loss processes

Periglacial surfaces showed similar centimeter-scale elevation loss rates as river beds and anthropogenic areas (Figure 3), where I assumed fluvial erosion and permafrost degradation to be key drivers of elevation change. These results are in contrast to observations by Liu et al. (2010), who observed relative stability of floodplains in northern Alaska. In the scope of this study, I classified areas as anthropogenic that covered of periglacial terrain under human influence. I therefore expect elevation loss in anthropogenic areas (-0.5 ± 11.4 to -2.7 ± 3.1 cm/year) to depict the same isotropic thaw subsidence processes as in the periglacial landscape. This assumption was supported by observations by Chen (2019), who found that buildings in Ny-Ålesund subsided at -1 to -4 cm/year. In contrast to periglacial areas, however, I detected consistent average subsidence rates across time periods for anthropogenic areas in the Bayelva basin. This observation reflects a relative stability of the airport that is further supported by the local authorities' intense runway maintenance (Sand 2024, private communication). Moreover, I detected an increasing amount of pixels experiencing elevation gain in recent observation periods reflecting the construction of roads, buildings, and infrastructure as Ny-Ålesund expanded since the 1980s with the rapid increase in scientific activities (Paglia 2019).

I observed larger decimeter-scale elevation loss rates at moraines (Figure 3) as melting of ice-cored moraines and rock fall processes prevailed. The periglacial terrain around Leirhaugen hill consists of glacial deposits from the Kongsfjorden glacier (Boike et al. 2018). Against this background, I assume that the lower Bayelva basin was influenced by proglacial processes that may be similar to those observed

at the moraines today. In that case, periglacial ground in the Bayelva basin was historically ice-rich, potentially encompassing ice-cored moraines at the time of last glacial retreat.

My results furthermore showed meter-scale elevation loss rates at the tongue of the Austre Brøggerbreen glacier (Figure 3). Elevation loss rates increased since 1936 reflecting accelerated glacial thinning and retreat (Geyman et al. 2022; Ren et al. 2021).

5.2 Thaw subsidence in relation to surface properties

In this study, I found spatial variations of thaw subsidence in periglacial areas of the Bayelva basin, that could partially be linked to terrain forms, vegetation cover, or timing of snow cover disappearance (RQ2, Section 4.2). However, my results only propose a slight relation between thaw subsidence and surface properties as within-class variance was generally higher than between-class variance (Figure 5).

5.2.1 Thaw subsidence in relation to topography and snow

I observed a tendency towards larger subsidence rates in topographic depressions and for areas that were longer covered by snow. These patterns were particularly pronounced in 1936-2020, when subsidence rates were -4 cm/year stronger in valleys than on ridges and -3 cm/year larger for areas that were longest snow-covered compared to those among the first to be snow-free (Figure 5).

The relation between thaw subsidence and topography and snow was more pronounced in earlier than in recent decades. In fact, my observations suggest that the strong subsidence rates of periglacial areas in the 20th century (as described in Section 5.1.2) was spatially mainly focused on topographic depressions with long snow covers. While subsidence rates in 1936-2020 were comparable to later observation periods at ridges and shoulders, subsidence was about -5 cm/year more pronounced in valleys and at footslopes (Figure 5).

The observed tendency is in line with a study by Yu et al. (2024) who also found enhanced subsidence rates in periglacial valleys in central Spitsbergen and by O'Neill et al. (2023) who observed high subsidence rates for sites with deep snow cover in northwestern Canada. Eckerstorfer et al. (2017) furthermore showed a direct connection between snow, topography, and elevation change in mid-western Spitsbergen. They observed that snow accumulated in valleys and pits while the neighbouring raised terrain was typically sooner blown free of snow.

I hypothesise that snow cover mainly impacts on the subsidence potential through 1) its insulating effect and 2) by steering water availability. For the first hypothesis, Jan and Painter (2020) show the impact of changes in snow timing on subsurface thermal conditions and Grünberg et al. (under review) highlight the importance of snow cover and depth for active layer properties and permafrost temperatures in the Bayelva basin. At the Bayelva observatory, Grünberg et al. (under review) associated little snow during cold winters with low active layer and permafrost temperatures due to the weak insulating effect of thin snow cover. Against this background, areas

with early snow disappearance timing are likely to experience thinner snow cover in winter which cools the permafrost and therefore leads to weaker subsidence rates. For the second hypothesis, Eckerstorfer et al. (2017) concluded that melt water availability was higher in topographic depressions where snow accumulated which enhanced periglacial processes like frost heave and thaw subsidence. This is likely to mainly affect the degree of seasonal elevation change when the active layer freezes and thaws. However, if the spatial snow patterns were similar during times when permafrost formed, high melting water availability might have intensified ground ice content in snow-rich areas.

5.2.2 Thaw subsidence in relation to vegetation

I did not observe a clear relation between vegetation index and subsidence of periglacial surfaces. Only for 1936-2020, my results showed a tendency towards slightly larger subsidence rates in areas without vegetation cover than in areas with relatively high vegetation density (Figure 5). This is in contrast to findings by Yu et al. (2024), who analysed subsidence and land cover in central Spitsbergen and detected higher subsidence rates for herbaceous wetlands, moss and lichen as compared to sparse vegetation and bare ground. They suggest that ground subsidence is associated with high soil water content, which favours vegetation.

5.3 Thaw subsidence across the Brøgger peninsula

Within the Brøgger peninsula (RQ3), I found the Bayelva basin to be a representative subregion of the northern peninsula as it covered all common landscapes (Section 4.3). Periglacial areas and river beds showed similar elevation change rates across regions (Figure 6). Anthropogenic areas on the northern peninsula (i.e. all of Ny-Ålesund and its surrounding) subsided on average -2 cm/year (1936-2010) more than within the Bayelva basin (i.e. mainly the airport) as runway maintenance supposedly leads to a relative stability of the airport (Sand 2024, private communication). The Austre Brøggerbreen glacier in the Bayelva basin appeared to face larger elevation loss rates than other glaciers on the Brøgger peninsula (Figure 6). However, this observation is likely to be biased by the fact that the Bayelva basin only covered the glacial tongue while the northern peninsula also encompassed high-elevation accumulation zones of glaciers.

Within periglacial terrain, I observed spatial thaw subsidence patterns in the Bayelva basin and on the broader northern peninsula to be comparable. Both regions showed a tendency towards enhanced subsidence in topographic depressions and longer snow-covered areas (Figure 7) as discussed in Section 5.2.1.

Thaw subsidence patterns on the Kvadehuksletta were less pronounced than those on the northern peninsula (Figure 7), supposedly due to its very different landscape characteristics. The Kvadehuksletta is a flat plateau without glacial influence or mountainous mass movements. Located at the tip of the peninsula, the Kvadehuksletta is more exposed to marine influences than the northern peninsula potentially causing the relative early disappearance of all snow patches (Figure B.7).

In terms of its geology, the Kvadehuksletta is characterised by raised beaches as response to ice unloading during Holocene deglaciation of the area (Forman et al. 1987). Consequently, sediments on the Kvadehuksletta consist of marine, fluvial, and deltaic deposits (Norwegian Polar Institute 2016; Sassenroth et al. 2020) while glacial deposits from the Kongsfjord glacier prevail on the northern peninsula (Boike et al. 2018; Forman et al. 1987). The sedimentary history may highly influence ground ice content (Cable et al. 2017) and thus subsidence rates.

6 Conclusion

In summary, this study shows an ongoing elevation loss trend that has persisted for decades and stretches across the entire Bayelva basin (RQ1). Through DEM-differencing and repeated GNSS surveys, I detected periglacial thaw subsidence rates that range from -0.7 cm/year in recent years to -6.4 cm/year since 1936. These observations reveal permafrost changes in the Bayelva basin dating back to the middle of the 20th century and proposing the early thaw of a particular ice-rich horizon. To my knowledge, this study for the first time quantifies periglacial elevation change on Svalbard for a period of more than 80 years, highlighting the great potential of historic DEMs.

The detected thaw subsidence rates exceed previously reported observations on Svalbard, suggesting a strong deepening of the active layer in the Bayelva basin. Extensive ground ice loss was therefore revealed to be a widespread phenomenon in the region impacting on surface stability in the permafrost landscape.

My findings additionally show a spatial relation between the rate of thaw subsidence and snow cover (RQ2). Slightly higher subsidence rates in areas with more snow-accumulation suggest that the insulating effect of thick snow covers in winter enhances permafrost degradation. Against this background, the removal of snow during the winter months may have a cooling effect on permafrost, potentially increasing surface and infrastructure stability.

With similar subsidence patterns and rates, I found the Bayelva basin to be a representative subregion of the northern Brøgger peninsula (RQ3). In contrast, I observed less pronounced subsidence patterns at the Kvadehuksletta showing the high influence of sedimentary history and geological structures on ground ice content and subsidence potential in periglacial landscapes.

In conclusion, this study represents a pioneering effort of thaw subsidence detection in northwestern Svalbard. For the first time, this study quantifies widespread ground ice loss in the Bayelva basin, a process notoriously difficult to detect. I therefore contribute to research on permafrost degradation by demonstrating the suitability of both multi-temporal DEMs and repeated GNSS measurements to expand in-situ observations on permafrost thaw beyond the research sites. The results highlight the importance of subsidence observations as thaw depth measurements alone underestimate actual thaw penetration by multiple centimeters each year. At the same time, my analysis identifies the lack of stable reference terrain in periglacial landscapes as major challenge for subsidence quantification. Future research may highly benefit from the implementation of direct in-situ measurements of surface elevation at fixed locations to complement and validate DEM- and GNSS-observations.

All in all, my findings present the great potential of surface subsidence as an indicator for monitoring ground ice content and permafrost degradation. I conclude that isotropic thaw subsidence is a crucial yet often underestimated component of permafrost landscapes in the warming Arctic.

Acknowledgement

This study would not have been possible without the tireless support of Julia Boike and Inge Grünberg. With their scientific ideas, contagious enthusiasm, and warm-hearted encouragement, they provided me with the exact supervision I needed. Thank you for all that time and effort, for the honesty and empowerment, for taking me on this memorable trip to Svalbard, for showing me female research perspectives, and for teaching me the beauty of science.

I am very grateful to the whole SPARC-group at the Alfred-Wegener-Institute in Potsdam, who always made me enjoy coming to work. Thank you for adopting me in the group, for the knowledge-sharing, for the lunch-brunch-cake-fun, and for showing me this scientific happy-place. Special thanks to Jennika Hammar for her initial ideas and first analyses, and to Bill Cable for helping me prepare the expedition equipment. Many thanks also to my peers at SPARC - Maybrit Goldau, Jannika Gottuk, Daniela Hollenbach Borges, Laura Berger, Luisa Näke - for the valuable feedback and exchange.

My study highly depended on previous work and achievements of the scientific community. I'd like to acknowledge everyone working at the AWIPEV research station for making our (and all the past and future) field work possible. I am grateful to researchers from DLR, NPI, NORCE and AWI who were involved in flight campaigns and DEM generation and therefore laid the foundation of my study. Many thanks also to Markus Bradke (GFZ), Susana Garcia Espada (Kartverket), and the support teams from Planet Labs and Leica Geosystems for answering my questions so patiently.

Lastly, I would like to thank everyone who has travelled this M.Sc. and thesis path with me. Thank you to Saskia, Kirsten, and Monique who have accompanied me all the way - from the beginning to the end. Thank you to Maeve, Melanie, Anna, and Benni who made sure I celebrated my achievements accordingly. Thank you to my WG for always being there for me and for being family. And thank you to Moritz for supporting, accepting, and handling all of my emotions. Thank you all, for being this beautiful moral-support network.

In loving memory of Ida and Julia.

References

- Antonova, S., Sudhaus, H., Strozzi, T., Zwieback, S., Kääb, A., Heim, B., Langer, M., Bornemann, N., and Boike, J.: Thaw Subsidence of a Yedoma Landscape in Northern Siberia, Measured In Situ and Estimated from TerraSAR-X Interferometry, *Remote Sensing*, 10, 494, <https://doi.org/10.3390/rs10040494>, 2018.
- Ballantyne, C. K.: *Periglacial geomorphology*, John Wiley & Sons, 2018.
- Biskaborn, B. K., Smith, S. L., Noetzli, J., Matthes, H., Vieira, G., Streletskiy, D. A., Schoeneich, P., Romanovsky, V. E., Lewkowicz, A. G., Abramov, A., Allard, M., Boike, J., Cable, W. L., Christiansen, H. H., Delaloye, R., Diekmann, B., Drozdov, D., Eitzelmüller, B., Grosse, G., Guglielmin, M., Ingeman-Nielsen, T., Isaksen, K., Ishikawa, M., Johansson, M., Johannsson, H., Joo, A., Kaverin, D., Kholodov, A., Konstantinov, P., Kröger, T., Lambiel, C., Lanckman, J.-P., Luo, D., Malkova, G., Meiklejohn, I., Moskalenko, N., Oliva, M., Phillips, M., Ramos, M., Sannel, A. B. K., Sergeev, D., Seybold, C., Skryabin, P., Vasiliev, A., Wu, Q., Yoshikawa, K., Zheleznyak, M., and Lantuit, H.: Permafrost is warming at a global scale, *Nature Communications*, 10, <https://doi.org/10.1038/s41467-018-08240-4>, 2019.
- Boike, J., Juszak, I., Lange, S., Chadburn, S., Burke, E., Overduin, P. P., Roth, K., Ippisch, O., Bornemann, N., Stern, L., Gouttevin, I., Hauber, E., and Westermann, S.: A 20-year record (1998–2017) of permafrost, active layer and meteorological conditions at a high Arctic permafrost research site (Bayelva, Spitsbergen), *Earth System Science Data*, 10, 355–390, <https://doi.org/10.5194/essd-10-355-2018>, 2018.
- Boike, J., Chadburn, S., Martin, J., Zwieback, S., Althuizen, I. H., Anselm, N., Cai, L., Coulombe, S., Lee, H., Liljedahl, A. K., Schneebeli, M., Sjöberg, Y., Smith, N., Smith, S. L., Streletskiy, D. A., Stuenzi, S. M., Westermann, S., and Wilcox, E. J.: Standardized monitoring of permafrost thaw: a user-friendly, multiparameter protocol, *Arctic Science*, 8, 153–182, <https://doi.org/10.1139/as-2021-0007>, 2022.
- Bundesamt für Kartographie und Geodäsie: Global Navigation Satellite System (GNSS), <https://www.bkg.bund.de/DE/Observatorium-Wetzell/Messverfahren/Global-Navigation-System/global-navigation-system.htm>, last access: 2024-03-31, n.d.
- Cable, S., Elberling, B., and Kroon, A.: Holocene permafrost history and cryostratigraphy in the High-Arctic Adventdalen Valley, central Svalbard, *Boreas*, 47, 423–442, <https://doi.org/10.1111/bor.12286>, 2017.
- Cai, L., Lee, H., Aas, K. S., and Westermann, S.: Projecting circum-Arctic excess-ground-ice melt with a sub-grid representation in the Community Land Model, *The Cryosphere*, 14, 4611–4626, <https://doi.org/10.5194/tc-14-4611-2020>, 2020.

- Chen, J.: Studying Permafrost and Active Layer Dynamics in Tibet and Arctic by Multi-temporal Radar Interferometry, The Chinese University of Hong Kong (Hong Kong), 2019.
- Christiansen, H. H., Gilbert, G. L., Neumann, U., Demidov, N., Guglielmin, M., Isaksen, K., Osuch, M., and Boike, J.: Ground ice content, drilling methods and equipment and permafrost dynamics in Svalbard 2016–2019 (PermaSval), Tech. rep., Svalbard Integrated Arctic Earth Observing System, <https://doi.org/10.5281/ZENODO.4294095>, 2021.
- Constable, A., Harper, S., Dawson, J., Holsman, K., Mustonen, T., Piepenburg, D., and Rost, B.: Cross-Chapter Paper 6: Polar Regions, in: *Climate Change 2022: Impacts, Adaptation and Vulnerability. Contribution of Working Group II to the Sixth Assessment Report of the Intergovernmental Panel on Climate Change*, edited by Pörtner, H. O., Roberts, D. C., Tignor, M., Poloczanska, E. S., Mintenbeck, K., Alegría, A., Craig, M., Langsdorf, S., Löschke, S., Möller, V., Okem, A., and Rama, B., pp. 2319–2368, Cambridge University Press, Cambridge, UK and New York, USA, <https://doi.org/10.1017/9781009325844.023>, 2022.
- Dobinski, W.: Permafrost, *Earth-Science Reviews*, 108, 158–169, <https://doi.org/10.1016/j.earscirev.2011.06.007>, 2011.
- Eckerstorfer, M., Malnes, E., and Christiansen, H.: Freeze/thaw conditions at periglacial landforms in Kapp Linné, Svalbard, investigated using field observations, in situ, and radar satellite monitoring, *Geomorphology*, 293, 433–447, <https://doi.org/10.1016/j.geomorph.2017.02.010>, 2017.
- Epstein, H. E., Raynolds, M. K., Walker, D. A., Bhatt, U. S., Tucker, C. J., and Pinzon, J. E.: Dynamics of aboveground phytomass of the circumpolar Arctic tundra during the past three decades, *Environmental Research Letters*, 7, 015 506, <https://doi.org/10.1088/1748-9326/7/1/015506>, 2012.
- Forman, S. L., Mann, D. H., and Miller, G. H.: Late Weichselian and Holocene Relative Sea-level History of Bröggerhalvöya, Spitsbergen, *Quaternary Research*, 27, 41–50, [https://doi.org/10.1016/0033-5894\(87\)90048-2](https://doi.org/10.1016/0033-5894(87)90048-2), 1987.
- GDAL/OGR contributors: GDAL/OGR Geospatial Data Abstraction software Library (software), Open Source Geospatial Foundation, <https://doi.org/10.5281/zenodo.5884351>, 2024.
- Geoforschungszentrum: NYA200NOR, <https://gnss.gfz-potsdam.de/infrastructure/network/NYA200NOR>, last access: 2023-11-17, n.d.
- Geyman, E. C., J. J. van Pelt, W., Maloof, A. C., Aas, H. F., and Kohler, J.: Historical glacier change on Svalbard predicts doubling of mass loss by 2100, *Nature*, 601, 374–379, <https://doi.org/10.1038/s41586-021-04314-4>, 2022.

- Grünberg, I., Groenke, B., Westermann, S., and Boike, J.: Permafrost and active layer temperature and freeze/thaw timing reflect climatic trends at Bayelva, Svalbard, *JGR: Earth Surface*, under review.
- Günther, F., Overduin, P. P., Yakshina, I. A., Opel, T., Baranskaya, A. V., and Grigoriev, M. N.: Observing Muostakh disappear: permafrost thaw subsidence and erosion of a ground-ice-rich island in response to arctic summer warming and sea ice reduction, *The Cryosphere*, 9, 151–178, <https://doi.org/10.5194/tc-9-151-2015>, 2015.
- Hatanaka, Y.: A compression format and tools for GNSS observation data, <https://www.gsi.go.jp/common/000045517.pdf>, last access: 2024-03-31, 2008.
- Hofmann-Wellenhof, B., Lichtenegger, H., and Wasle, E.: *GNSS—global navigation satellite systems: GPS, GLONASS, Galileo, and more*, Springer Science & Business Media, 2007.
- Humlum, O., Instanes, A., and Sollid, J. L.: Permafrost in Svalbard: a review of research history, climatic background and engineering challenges, *Polar Research*, 22, 191–215, <https://doi.org/10.3402/polar.v22i2.6455>, 2003.
- International GNSS Service: Station information - NYA100NOR, <https://network.igs.org?current=true&search=NYA100NOR&selected=NYA100NOR&zoom=10¢er=78.93390513344741¢er=11.922279946200774&popup=NYA100NOR&spin=false&bearing=0&pitch=0&style=mapbox%3A%2F%2Fstyles%2Fmapbox%2Fflight-v11&projection=globe&info=true&table=false>, last access: 2023-11-17, n.d.
- Isaev, V., Koshurnikov, A., Pogorelov, A., Amangurov, R., Podchasov, O., Sergeev, D., Buldovich, S., Aleksyutina, D., Grishakina, E., and Kioka, A.: Cliff retreat of permafrost coast in south-west Baydaratskaya Bay, Kara Sea, during 2005–2016, *Permafrost and Periglacial Processes*, 30, 35–47, <https://doi.org/10.1002/ppp.1993>, 2019.
- Isaksen, K., Nordli, Ø., Ivanov, B., Køltzow, M. A. Ø., Aaboe, S., Gjelten, H. M., Mezghani, A., Eastwood, S., Førland, E., Benestad, R. E., Hanssen-Bauer, I., Brækkan, R., Sviashchennikov, P., Demin, V., Revina, A., and Karandashva, T.: Exceptional warming over the Barents area, *Scientific Reports*, 12, <https://doi.org/10.1038/s41598-022-13568-5>, 2022.
- Jan, A. and Painter, S. L.: Permafrost thermal conditions are sensitive to shifts in snow timing, *Environmental Research Letters*, 15, 084026, <https://doi.org/10.1088/1748-9326/ab8ec4>, 2020.
- Jasiewicz, J. and Stepinski, T. F.: Geomorphons — a pattern recognition approach to classification and mapping of landforms, *Geomorphology*, 182, 147–156, <https://doi.org/10.1016/j.geomorph.2012.11.005>, 2013.

- Jasiewicz, J. and Stepinski, T. F.: r.geomorphon (Software, GRASS GIS 8.3.3dev Reference Manual), <https://grass.osgeo.org/grass83/manuals/r.geomorphon.html>, 2023.
- Kääb, A.: Remote sensing of mountain glaciers and permafrost creep, Schriftenreihe Physische Geographie, Glaziologie und Gemorphodynamik, Geographisches Institut der Universität Zürich, Zürich, ISBN 3855432449, 2005.
- Kääb, A., Girod, L., and Berthling, I.: Surface kinematics of periglacial sorted circles using structure-from-motion technology, *The Cryosphere*, 8, 1041–1056, <https://doi.org/10.5194/tc-8-1041-2014>, 2014.
- Lange, S., Cable, W. L., and Boike, J.: GNSS Measurements Ny Ålesund & Bayelva Svalbard 2019, <https://doi.org/10.1594/PANGAEA.913309>, 2020.
- Liu, L. and Larson, K. M.: Decadal changes of surface elevation over permafrost area estimated using reflected GPS signals, *The Cryosphere*, 12, 477–489, <https://doi.org/10.5194/tc-12-477-2018>, 2018.
- Liu, L., Zhang, T., and Wahr, J.: InSAR measurements of surface deformation over permafrost on the North Slope of Alaska, *Journal of Geophysical Research: Earth Surface*, 115, <https://doi.org/10.1029/2009jf001547>, 2010.
- Mannerfeld, E., Hugonnet, R., Dehecq, A., et al.: xDEM (software manual): Analysis of accuracy and precision, https://xdem.readthedocs.io/en/stable/intro_accuracy_precision.html, last access: 2024-03-31, 2021a.
- Mannerfeld, E., Hugonnet, R., Dehecq, A., et al.: xDEM (software manual): Coregistration, <https://xdem.readthedocs.io/en/stable/coregistration.html>, last access: 2024-03-31, 2021b.
- Meredith, M., Sommerkorn, M., Cassotta, S., Derksen, C., Ekaykin, A., Hollowed, A., Kofinas, G., Mackintosh, A., Melbourne-Thomas, J., Muelbert, M., Ottersen, G., Pritchard, H., and Schuur, E.: Polar Regions, in: *The Ocean and Cryosphere in a Changing Climate: Special Report of the Intergovernmental Panel on Climate Change*, edited by Pörtner, H.-O., Roberts, D., MassonDelmotte, V., Zhai, P., Tignor, M., Poloczanska, E., Mintenbeck, K., Alegría, A., Nicolai, M., Okem, A., Petzold, J., Rama, B., and Weyer, N., book section 3, p. 203–320, Cambridge University Press, <https://doi.org/10.1017/9781009157964.005>, 2019.
- Miccadei, E., Piacentini, T., and Berti, C.: Geomorphological features of the Kongsfjorden area: Ny-Ålesund, Blomstrandøya (NW Svalbard, Norway), *Rendiconti Lincei*, 27, 217–228, <https://doi.org/10.1007/s12210-016-0537-3>, 2016.
- Nischan, T.: GFZRNX - RINEX GNSS Data Conversion and Manipulation Toolbox, <https://doi.org/10.5880/GFZ.1.1.2016.002>, 2016.

- Noetzli, J., Arenson, L. U., Bast, A., Beutel, J., Delaloye, R., Farinotti, D., Gruber, S., Gubler, H., Haeberli, W., Hasler, A., Hauck, C., Hiller, M., Hoelzle, M., Lambiel, C., Pellet, C., Springman, S. M., Vonder Muehll, D., and Phillips, M.: Best Practice for Measuring Permafrost Temperature in Boreholes Based on the Experience in the Swiss Alps, *Frontiers in Earth Science*, 9, <https://doi.org/10.3389/feart.2021.607875>, 2021.
- Noh, M.-J. and Howat, I. M.: Automated stereo-photogrammetric DEM generation at high latitudes: Surface Extraction with TIN-based Search-space Minimization (SETSM) validation and demonstration over glaciated regions, *GIScience & Remote Sensing*, 52, 198–217, <https://doi.org/10.1080/15481603.2015.1008621>, 2015.
- Nordli, Ø., Wyszynski, P., Gjelten, H., Isaksen, K., Lupikasza, E., Niedźwiedź, T., and Przybylak, R.: Revisiting the extended Svalbard Airport monthly temperature series, and the compiled corresponding daily series 1898–2018, *Polar Research*, 39, <https://doi.org/10.33265/polar.v39.3614>, 2020.
- Norwegian Polar Institute: Terrengmodell Svalbard (S0 Terrengmodell), <https://doi.org/10.21334/NPOLAR.2014.DCE53A47>, 2014a.
- Norwegian Polar Institute: Kartdata Svalbard 1:100 000 (S100 Kartdata) / Map Data [Kartdata Svalbard (S100, ESRI Shapefile)], <https://doi.org/10.21334/npolar.2014.645336c7>, 2014b.
- Norwegian Polar Institute: Geological map of Svalbard (1:250000), <https://doi.org/10.21334/npolar.2016.616f7504>, 2016.
- Nowak, A. and Hodson, A.: Hydrological response of a High-Arctic catchment to changing climate over the past 35 years: a case study of Bayelva watershed, Svalbard, *Polar Research*, 32, 19 691, <https://doi.org/10.3402/polar.v32i0.19691>, 2013.
- Nuth, C. and Kääb, A.: Co-registration and bias corrections of satellite elevation data sets for quantifying glacier thickness change, *The Cryosphere*, 5, 271–290, <https://doi.org/10.5194/tc-5-271-2011>, 2011.
- Obu, J.: How Much of the Earth’s Surface is Underlain by Permafrost?, *Journal of Geophysical Research: Earth Surface*, 126, <https://doi.org/10.1029/2021jf006123>, 2021.
- Oldenborger, G. A., Bellehumeur-Génier, O., LeBlanc, A.-M., and McMartin, I.: Landform mapping, elevation modelling, and thaw subsidence estimation for permafrost terrain using a consumer-grade remotely-piloted aircraft, *Drone Systems and Applications*, 10, 309–329, <https://doi.org/10.1139/dsa-2021-0045>, 2022.
- O’Neill, H. B., Smith, S. L., Burn, C. R., Duchesne, C., and Zhang, Y.: Widespread Permafrost Degradation and Thaw Subsidence in Northwest Canada, *Journal of*

- Geophysical Research: Earth Surface, 128, <https://doi.org/10.1029/2023jf007262>, 2023.
- Paglia, E.: A higher level of civilisation? The transformation of Ny-Ålesund from Arctic coalmining settlement in Svalbard to global environmental knowledge center at 79° North, *Polar Record*, 56, <https://doi.org/10.1017/s0032247419000603>, 2019.
- Philipp, M., Dietz, A., Buchelt, S., and Kuenzer, C.: Trends in Satellite Earth Observation for Permafrost Related Analyses—A Review, *Remote Sensing*, 13, 1217, <https://doi.org/10.3390/rs13061217>, 2021.
- Planet Labs PBC: Planet Application Program Interface: In Space for Life on Earth, <https://api.planet.com>, 2023.
- Polidori, L. and El Hage, M.: Digital Elevation Model Quality Assessment Methods: A Critical Review, *Remote Sensing*, 12, 3522, <https://doi.org/10.3390/rs12213522>, 2020.
- Ren, G., Wang, J., Lu, Y., Wu, P., Lu, X., Chen, C., and Ma, Y.: Monitoring Changes to Arctic Vegetation and Glaciers at Ny-Ålesund, Svalbard, Based on Time Series Remote Sensing, *Remote Sensing*, 13, 3845, <https://doi.org/10.3390/rs13193845>, 2021.
- Rey, D. M., Walvoord, M., Minsley, B., Rover, J., and Singha, K.: Investigating lake-area dynamics across a permafrost-thaw spectrum using airborne electromagnetic surveys and remote sensing time-series data in Yukon Flats, Alaska, *Environmental Research Letters*, 14, 025 001, <https://doi.org/10.1088/1748-9326/aaf06f>, 2019.
- Rodenhizer, H., Ledman, J., Mauritz, M., Natali, S. M., Pegoraro, E., Plaza, C., Romano, E., Schädel, C., Taylor, M., and Schuur, E.: Carbon Thaw Rate Doubles When Accounting for Subsidence in a Permafrost Warming Experiment, *Journal of Geophysical Research: Biogeosciences*, 125, <https://doi.org/10.1029/2019jg005528>, 2020.
- Rouyet, L., Lauknes, T. R., Christiansen, H. H., Strand, S. M., and Larsen, Y.: Seasonal dynamics of a permafrost landscape, Adventdalen, Svalbard, investigated by InSAR, *Remote Sensing of Environment*, 231, 111 236, <https://doi.org/10.1016/j.rse.2019.111236>, 2019.
- Rouyet, L., Liu, L., Strand, S. M., Christiansen, H. H., Lauknes, T. R., and Larsen, Y.: Seasonal InSAR Displacements Documenting the Active Layer Freeze and Thaw Progression in Central-Western Spitsbergen, Svalbard, *Remote Sensing*, 13, 2977, <https://doi.org/10.3390/rs13152977>, 2021.
- Sand, V.: Surface of the airstrip in Ny-Ålesund, head of Airport Operations, Kings Bay AS, Ny-Ålesund (e-mail on 2024-03-13), 2024, private communication.

- Sassenroth, C., Hauber, E., Salvatore, M., and Baroni, C.: Geomorphological map of Kvadehuksletta, western coast of Oscar II Land (Svalbard, Norway), 2020.
- Shiklomanov, N. I., Streletskiy, D. A., Little, J. D., and Nelson, F. E.: Isotropic thaw subsidence in undisturbed permafrost landscapes, *Geophysical Research Letters*, 40, 6356–6361, <https://doi.org/10.1002/2013gl058295>, 2013.
- Śledź, S. and Ewertowski, M. W.: Evaluation of the Influence of Processing Parameters in Structure-from-Motion Software on the Quality of Digital Elevation Models and Orthomosaics in the Context of Studies on Earth Surface Dynamics, *Remote Sensing*, 14, 1312, <https://doi.org/10.3390/rs14061312>, 2022.
- Smith, S. L., Romanovsky, V. E., Isaksen, K., Nyland, K. E., Kholodov, A. L., Shiklomanov, N. I., Streletskiy, D. A., Farquharson, L. M., Drozdov, D. S., Malkova, G. V., et al.: Permafrost [in "State of the Climate in 2021"], *Bulletin of the American Meteorological Society*, 102, S293–S297, <https://doi.org/https://doi.org/10.1175/BAMS-D-22-0082.1>, 2021.
- Stern, L.: Hydraulic and Thermal properties of Permafrost in Svalbard, Analysis and Modelling using GEOtop, master's thesis, Department of Physics and Astronomy, University of Heidelberg, 2017.
- Streletskiy, D. A., Shiklomanov, N. I., Little, J. D., Nelson, F. E., Brown, J., Nyland, K. E., and Klene, A. E.: Thaw Subsidence in Undisturbed Tundra Landscapes, Barrow, Alaska, 1962–2015, *Permafrost and Periglacial Processes*, 28, 566–572, <https://doi.org/10.1002/ppp.1918>, 2016.
- Sturm, M. and Wagner, A. M.: Using repeated patterns in snow distribution modeling: An Arctic example, *Water Resources Research*, 46, <https://doi.org/10.1029/2010wr009434>, 2010.
- Thaler, E. A., Crumley, R. L., and Bennett, K. E.: Estimating snow cover from high-resolution satellite imagery by thresholding blue wavelengths, *Remote Sensing of Environment*, 285, 113 403, <https://doi.org/10.1016/j.rse.2022.113403>, 2023.
- Tucker, C. J. and Sellers, P. J.: Satellite remote sensing of primary production, *International Journal of Remote Sensing*, 7, 1395–1416, <https://doi.org/10.1080/01431168608948944>, 1986.
- Van Everdingen, R.: Multi-language Glossary of Permafrost and Related Ground-ice Terms, International Permafrost Association (IPA), revised edition 2005 edn., 1998.
- Vellut, G.: Freehand raster georeferencer (v0.8.3), <http://gvellut.github.io/FreehandRasterGeoreferencer/>, last access: 2024-03-31, 2021.
- Walczowski, W. and Piechura, J.: Influence of the West Spitsbergen Current on the local climate, *International Journal of Climatology*, 31, 1088–1093, <https://doi.org/10.1002/joc.2338>, 2011.

-
- Westermann, S., Østby, T., Gislås, K., Schuler, T., and Etzelmüller, B.: A ground temperature map of the North Atlantic permafrost region based on remote sensing and reanalysis data, *The Cryosphere*, 9, 1303–1319, <https://doi.org/10.5194/tc-9-1303-2015>, 2015.
- Witharana, C., Udawalpola, M. R., Liljedahl, A. K., Jones, M. K. W., Jones, B. M., Hasan, A., Joshi, D., and Manos, E.: Automated Detection of Retrogressive Thaw Slumps in the High Arctic Using High-Resolution Satellite Imagery, *Remote Sensing*, 14, 4132, <https://doi.org/10.3390/rs14174132>, 2022.
- Wolken, G. J., Liljedahl, A. K., Brubaker, M., Coe, J. A., Fiske, G., Christiansen, H. H., Jacquemart, M., Jones, B. M., Kääh, A., Løvholt, F., et al.: NOAA Arctic Report Card 2021: Glacier and Permafrost Hazards, <https://doi.org/10.25923/V40R-0956>, 2021.
- xDEM contributors: xDEM (software, v0.0.2), <https://doi.org/10.5281/zenodo.4809698>, 2021.
- Yu, Y., Zhou, Y., Hui, F., Cheng, X., and Wang, K.: Recent Ground Displacement Over Permafrost in Midwestern Spitsbergen, Svalbard: InSAR Measurements and Modeling, *IEEE Journal of Selected Topics in Applied Earth Observations and Remote Sensing*, 17, 573–583, <https://doi.org/10.1109/jstars.2023.3332448>, 2024.
- Zwieback, S. and Meyer, F. J.: Top-of-permafrost ground ice indicated by remotely sensed late-season subsidence, *The Cryosphere*, 15, 2041–2055, <https://doi.org/10.5194/tc-15-2041-2021>, 2021.

A Extended methodology

The following section provides a detailed description of the data basis, data collection, processing, and analysis steps. Figure A.1 outlines the methodological workflow of this study visually. A brief summary of the methodological approach can be found in section 3.

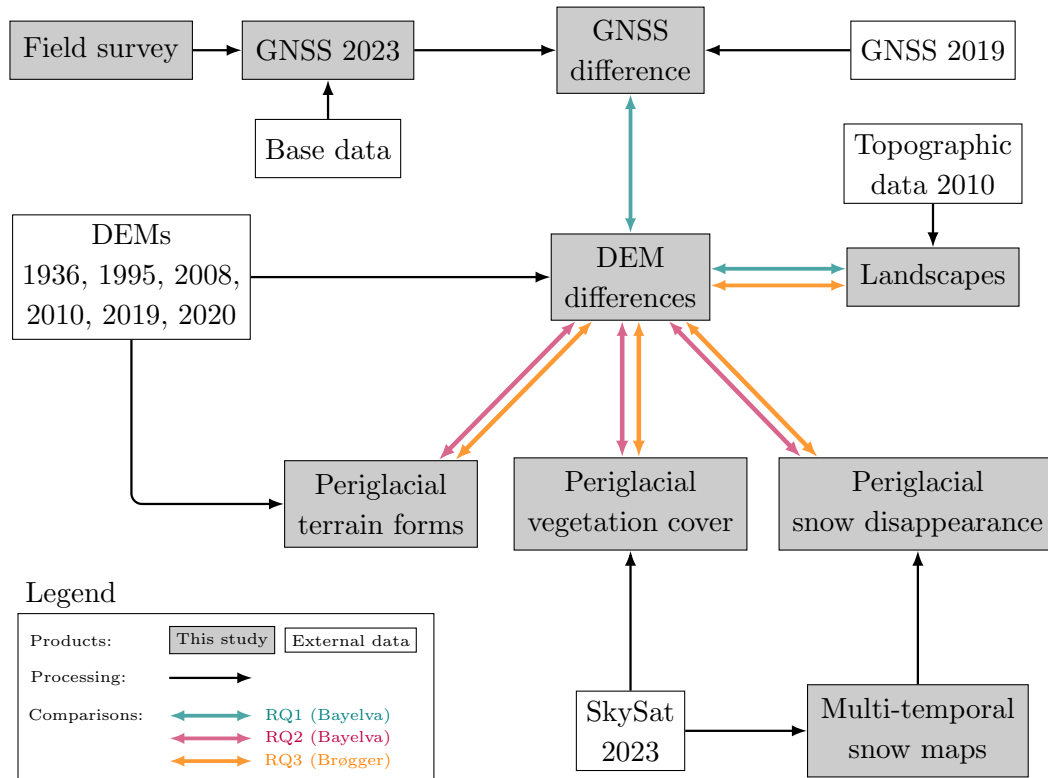


Figure A.1: Simplified methodological workflow - External data products (see section A.1), products generated in the scope of this study (see section 4) and connecting processing and comparison steps (see sections A.2-3.3).

A.1 Data basis

I based my subsidence study on two different sets of elevation data: Satellite-based positioning data and digital elevation models. I furthermore used aerial and satellite imagery as well as topographic data to derive surface and landscape characteristics.

A.1.1 Satellite-based positioning data

Space-borne satellites enable the determination of positions on Earth. Each satellite transmits its position in space and the time of measurement to the receiver on ground. The receiver then calculates the geometric distance to each satellite based on the time the satellite signal requires to reach the receiver. With signals from at least four satellites - three for the 3D-position and one for the clock bias - the receiver can determine its accurate position (Hofmann-Wellenhof et al. 2007). The Global Navigation Satellite System (GNSS) is a network of satellites that transmit this

positioning and timing data to GNSS receivers with global coverages. The most-known GNSS include the US-American GPS, the European Galileo, the Russian GLONASS and the Chinese BeiDou Navigation Satellite System. GNSS rovers usually receive data from a combination of these systems (Bundesamt für Kartographie und Geodäsie n.d.).

There are many factors that can affect the accuracy of coordinate determination, such as atmospheric disturbances or the reflection of signals from objects. A differential GNSS (DGNSS) therefore uses a network of GNSS receivers to account for potential errors. At least one of the GNSS receivers is built at a fixed and known location and functions as base station. The other GNSS receiver (or receivers) - the rover - is mobile and can be used for location measurements in the field. Both base and rover measure their positions at the same time. The atmospheric error can then be calculated for each point in time from the changes in GNSS signal at the fixed position base station. It can then be used to correct the GNSS signal received by the moving rover. The correction can be applied directly (real-time kinematic, RTK) if base and rover are connected to each other or later (post-processed kinematic, PPK) if a connection is not possible.

In the scope of this study, I collected and post-processed GNSS points from July and August 2023 which is further described in Sections A.2-A.3. I used GNSS measurements from an earlier field campaign in 2019 (Lange et al. 2020) to calculate elevation change. For the atmospheric error correction, I used reference data from two external base stations - both located at the Ny-Ålesund airport and therefore within a distance of 2 km from most measurements. NYA1 is run by the local mapping authority Kartverket (<https://www.kartverket.no/>) since 1997 (International GNSS Service n.d.) and NYA2 by the Geoforschungszentrum (GFZ) since 2000 (Geoforschungszentrum n.d.). All field measurements and reference data had the same temporal resolution of 1 Hz. For validation, Kartverket also provided control point coordinates from 2016.

A.1.2 Digital elevation models

A Digital Elevation Model (DEM) is the digital representation of the Earth's surface with respect to a reference system. Widely used in geoscience, DEMs offer a powerful tool to analyse terrain characteristics and changes. Most terrain mapping techniques first compute the altitude for a large amount of terrain points that are then being resampled to fit the grid resolution of the output DEM (Polidori and El Hage 2020). Since the early 20th century, photogrammetry has become a widely used and relatively low-cost technique to generate DEMs. Stereo photogrammetry combines overlapping and georeferenced images of the surface to identify and locate characteristic terrain points. In a multi-step approach, first a sparse and then a dense point cloud is derived as basis for the DEM generation (Śledź and Ewertowski 2022).

There are six DEMs from the Bayelva basin that formed the core of my study's elevation change quantification (Boike et al. 2018; Geyman et al. 2022; Norwegian

Polar Institute 2014a). All DEMs were derived from stereo images captured at flight campaigns between 1936 and 2020. All flight campaigns were held during summer months and images were mostly snow-free. The DEMs cover different extents ranging from Svalbard-wide to just a few square kilometers in the center of the Bayelva basin. Spatial resolutions and coordinate reference systems also vary between DEMs. Table A.1 provides an overview of the key characteristics of each DEM.

Table A.1: Properties of the different DEMs - Year and date of the flight campaign capturing the underlying stereo imagery, spatial resolution and extent of the DEM, original coordinate reference system, institute running the flight campaign, and data publication.

Flight campaign	Pixel size	Spatial extent	Coordinate reference system	Source
1936 (Summer)	5.00 m	Svalbard (61000 km ²)	EPSG:25833 (ETRS89 / UTM zone 33N)	NPI, Geyman et al. (2022)
1995 (18.08.)	5.00 m	North-eastern Brøgger (105 km ²)	EPSG:32633 (WGS 84 / UTM zone 33N)	NPI (not published)
2008 (17.07.)	0.50 m	Most of the Bayelva basin (23 km ²)	EPSG:9001 (IGS97)	DLR, Boike et al. (2018)
2010 (Summer)	5.00 m	Brøgger peninsula (280 km ²)	EPSG:25833 (ETRS89 / UTM zone 33N)	Norwegian Polar In- stitute (2014a)
2019 (03.09.)	0.50 m	Parts of the Bayelva basin (3 km ²)	EPSG:32633 (WGS 84 / UTM zone 33N)	NORCE (not published)
2020 (13.09.)	0.15 m	Bayelva basin (7 km ²)	EPSG:32632 (WGS 84 / UTM zone 32N)	DLR, AWI (not published)

The quality of photogrammetrically derived DEMs depends on a large variety of environment-, sensor- or algorithm-related factors such as the surveying conditions on the ground, the sensor stability, the geometric quality and resolution of the image, the overlap of the flight path and the accuracy of the image matching algorithm. High-contrasts in shaded areas in high-latitudes or mountains pose another challenge for photogrammetry (Noh and Howat 2015; Nuth and Kääb 2011). The generation of historical DEMs can be particularly challenging due to poor image qualities or unknown image parameters (Günther et al. 2015).

Unfortunately, I cannot adequately assess the vertical and horizontal accuracy of the six DEMs used in this study as metadata was insufficient. However, I expect to have eliminated systematic errors and increased relative accuracy through coregistration and offset correction (Mannerfeld et al. 2021a) as described in Sections 3 and A.4. Furthermore, I used multiple DEMs covering different time steps to assess the robustness of my results. Due to its noise, I excluded the 2019 DEM from the analysis (Section B.1.1).

A.1.3 Aerial imagery

Each DEM was supplied with a georeferenced orthophoto generated from the aerial images taken at the respective flight campaign (Boike et al. 2018; Geyman et al. 2022; Norwegian Polar Institute 2014a). I used these orthophotos for visualisation and to identify specific surface features or landscape changes between the years. Due to its high resolution and topicality, the 2020 orthophoto was most suited to inspect infrastructure and surface constitutions in areas of change (e.g. Section 3.1.2). I used the 2008 orthophoto to filter remnant snow patches from most analyses as its flight campaign took place earlier in summer than for the other orthophotos (Section A.7.3). Due to its spatial extent, I used the 2010 orthophoto whenever I had to examine surface features on the wider Brøgger peninsula (e.g. Section 3.3).

A.1.4 Satellite imagery

I was furthermore granted access and tasking rights to SkySat imagery (Planet Labs PBC 2023) in the scope of a Svalbard Integrated Arctic Earth Observing System (SIOS) proposal (BrøggerPlanet project). I tasked the SkySat satellites to capture the Bayelva basin and the Brøgger peninsula every two weeks between May and October 2023. Due to the region's cloudiness, the satellites did not successfully capture some tasking periods but provided useful imagery for snow and vegetation cover analyses (Sections 3.2-3.3) for early and mid summer. The imagery had a spatial resolution of 0.5 m per pixel and consists of three visible bands (blue, green, red) and one near-infrared band. Planet Labs PBC (2023) supplied each scene with an observation quality mask.

A.1.5 Topographic data

The Norwegian Polar Institute (2014b) provides Svalbard-wide topographic data as vector files. I used outlines for land areas, glaciers, moraines, river beds, and water bodies to classify landscapes on the Brøgger peninsula (Sections 3.1.2 and 3.3).

A.2 Collection of GNSS data

I surveyed a total of 901 satellite-based positions in the Bayelva basin, in Ny-Ålesund, and on the Kvadehuksletta during a field campaign in July and August 2023. I used a GS18 rover and a CS20 field controller (both from Leica Geosystems, <https://leica-geosystems.com/>) to measure the GNSS points. Due to radio silence regulations around Ny-Ålesund, I used a cable instead of Bluetooth to connect rover and field controller. For most measurements, the rover was mounted on a 1.8-m rover pole with a 20-cm diameter PVC plate attached to the bottom of the pole in order to keep the tip from sinking into moist soil. I chose a measurement frequency of 1 Hz and measured each GNSS point for 10 seconds. In order to increase the measurement accuracy, I enabled raw data logging and established initialisation periods at the beginning of each measurement chain. As the tilt compensation feature

was not available while logging raw data, I used a bubble level at the rover pole to ensure that the pole was straight during the measurements.

A.2.1 Repeated measurements

The main goal of the measurement campaign was to repeat GNSS measurements from an earlier field campaign in 2019 (Lange et al. 2020). I therefore filtered the measurements from 2019 in advance to only include high-quality post-processing results and composed overviews with maps and photos to retrieve the measurement locations in the field. At the locations, I repeated the measurement, took another photo and marked the location with a plastic pin for potential future analyses. The repeated measurements were all located close to the Bayelva permafrost observatory (Figure 2).

The main difficulty during data collection was to find the exact measurement location of the 2019 GNSS survey. Due to radio silence regulations, I was not able to measure in RTK mode and therefore relied on less precise GPS devices and photos to identify the respective locations. I implemented quality flags to account for the resulting uncertainty and filtered the measurements accordingly (Section A.3.5).

A.2.2 Bedrock observations

Mapping and masking stable terrain is an important step in DEM alignment and differencing. However, most terrain in the Bayelva basin is unstable. During the field campaign, I therefore searched for, documented, and GNSS-surveyed bedrock locations. The three bedrock outcrops that I used in my analysis were located at and west of the Ny-Ålesund airport as well as at the Kvadehuksletta (Figure 2).

A.2.3 Control points

The local mapping authority Kartverket provided me with coordinates of seven control points that were also located at or close to the Ny-Ålesund airport. I surveyed the control points during the field campaign for later validation of my measurements. Most control points were equipped with fixed screw threads on barrels or bedrock so that I screwed the rover with a 30-cm pole on the control point.

A.3 Processing of GNSS data

I corrected and validated my GNSS measurements based on reference data from permanent base stations (Section A.3.1) and control point measurements (Section A.3.3). In order to filter low-quality points, I implemented quality flags for each measurements (Section A.3.4). I finally subtracted height measurements from 2019 from my results for 2023 in order to quantify elevation change at GNSS measurement locations close to the Bayelva observatory (Section A.3.5).

A.3.1 Base data preparation

I used reference data from two external base stations for the error-correction of my GNSS measurements (Section A.1.1). While NYA1 data was provided as daily RINEX files by Kartverket (International GNSS Service n.d.), the GFZ provides NYA2 data as 15-minutes CRX files (Geoforschungszentrum n.d.). I used the CRX2RNX (Hatanaka 2008) and GFZRNX (Nischan 2016) tools to convert and merge NYA200NOR data for the time periods of my measurements. Although the base stations are permanently installed, their positions change slightly over time due to plate tectonics and continental uplift (Table A.2). The exact position also depends on the reference frame used for the coordinate determination. In order to compare coordinates, all coordinates had to refer to the same base position and reference frame. Before post-processing, I calculated the positions of the reference stations based on their moving speed and the reference frame ITRF14/IGb14 for both the actual date of measurement in 2023 and the date of Kartverket’s control point measurement in 2016 (Table A.2).

Table A.2: Positions of the GNSS reference stations - Cartesian coordinates of NYA1 and NYA2 within the IGb14 reference frame: (a) positions and velocities for the reference date in 2010, and (b) positions for the dates of Kartverket’s control point measurements in 2016 and my measurements in 2023.

(a) Positions and velocities at the reference date

Station	Date	Positions [m]			Velocities [m/year]		
		X	Y	Z	V_X	V_Y	V_Z
NYA1	2010-01-01	1202433.769	252632.326	6237772.642	-0.0145	0.0074	0.0109
NYA2	2010-01-01	1202379.425	252474.602	6237786.475	-0.0145	0.0074	0.0109

(b) Positions at the dates of measurement (used for post-processing)

Date	NYA1			NYA2		
	X	Y	Z	X	Y	Z
2016-09-01	1202433.672	252632.375	6237772.715	1202379.328	252474.651	6237786.548
2023-08-01	1202433.571	252632.426	6237772.790	1202379.227	252474.702	6237786.623

A.3.2 Post-processing and error correction

The post-processing of satellite locations corrects the measured GNSS signal for potential errors such as atmospheric disturbances. I used the Leica Infinity software to post-process the measurements based on the reference data from both base stations and with respect to the ITRF14/IGb14 reference frame. I post-processed the measurements twice in order to compare them with both earlier measurements from 2019 and Kartverket’s control point measurements from 2016 (Figure A.2). After the automatic correction with Leica Infinity, I manually identified and adjusted incorrect measurements (e.g. measurement next to instead of on top of a pipe).

Moreover, the tip of the rover pole was not aligned with the bottom side of the PVC plate but protruded the PVC plate by 1.5 cm. This offset impacted on the height measurements in locations where the tip sank into the ground. I therefore accounted for this offset for height measurements that were - according to the comments and photos taken in the field - not located on rocks or solid surfaces.

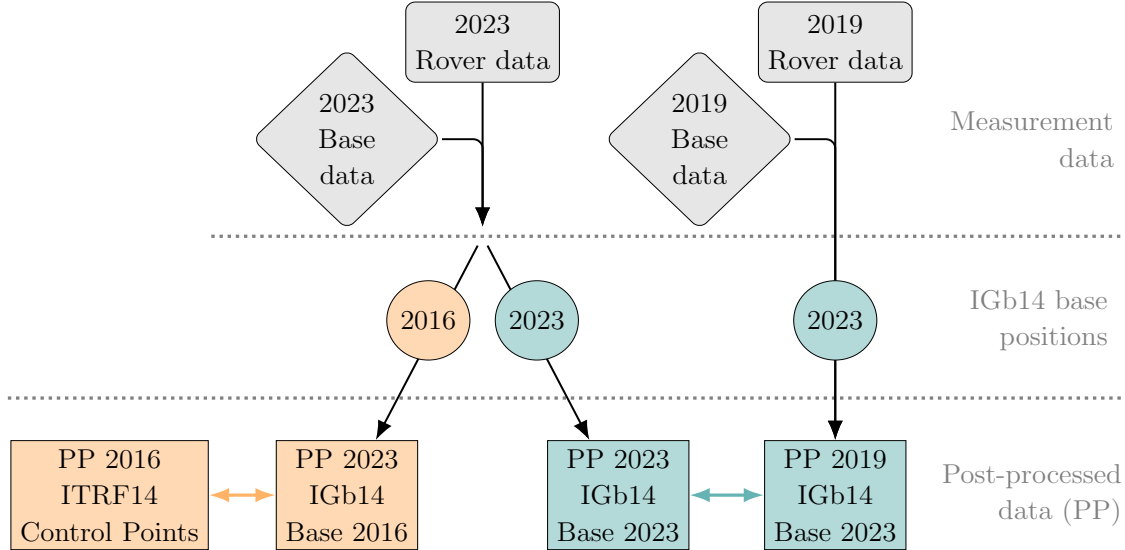


Figure A.2: Schematic overview of the post-processed GNSS data sets - Base and rover measurements from 2019 and 2023 (gray shapes) were post-processed using base position coordinates that were corrected for the years of comparison (blue and orange circles). The post-processed measurements from 2023 were compared to Kartverket’s control point measurements from 2016 for validation (orange rectangles) and to post-processed measurements from 2019 to calculate elevation change (blue rectangles).

A.3.3 Validation

I validated the GNSS measurements from 2023 by comparing the post-processed results to Kartverket’s control point coordinates (Figure A.2). The post-processing of my GNSS measurements showed very good results for NYA1 and good results for NYA2 (Table A.3). All validation points except for one were post-processed with a fixed phase solution ensuring a centimeter-accuracy. Only the NYA2 processing result of the FLYM measurement featured a code solution leading to low accuracies specifically in the height dimension (Table A.3). KLOK was the only control point not equipped with a fixed screw thread. During the GNSS survey, the exact location of KLOK was therefore not apparent, which could explain medium accuracies of the KLOK coordinates for both reference stations.

A.3.4 Implementation of quality flags

There are many factors that can affect the accuracy of GNSS coordinates, such as atmospheric disturbances, the reflection of signals from objects or the distance to

Table A.3: Validation of the GNSS measurements - Easting (E), Northing (N) and Elevation/Height (H) for the seven control points measured by Kartverket in 2016 and during the field campaign in 2023, as well as their differences: Very high accuracies in dark blue ($E/N < 0.005$ m, $H < 0.01$ m), high accuracies in light blue ($E/N 0.005-0.01$ m, $H 0.01-0.02$ m), medium accuracies in yellow ($E/N 0.01-0.05$ m, $H 0.02-0.1$ m), low accuracies in orange ($E/N > 0.05$ m, $H > 0.1$ m).

ID	NYA1			NYA2		
	E [m]	N [m]	H [m]	E [m]	N [m]	H [m]
FLYM (2016)	431803.886	8764495.806	81.271	431803.886	8764495.806	81.271
FLYM001 (2023)	431803.884	8764495.796	81.265	431803.891	8764495.828	80.852
Difference	0.0017	0.0101	0.0058	-0.0051	-0.0218	0.4192
FLYV (2016)	432475.104	8764184.567	64.812	432475.104	8764184.567	64.812
FLYN001 (2023)	432475.095	8764184.588	64.826	432475.088	8764184.589	64.832
Difference	0.0087	-0.0209	-0.0138	0.0162	-0.0222	-0.0202
KAIA (2016)	434364.642	8763578.940	42.017	434364.642	8763578.940	42.017
KAIA005 (2023)	434364.638	8763578.941	42.009	434364.630	8763578.941	42.018
Difference	0.0045	-0.0007	0.0085	0.0119	-0.0012	-0.0011
KLOK (2016)	434190.336	8763592.034	48.535	434190.336	8763592.034	48.535
KLOK002 (2023)	434190.318	8763592.059	48.499	434190.310	8763592.060	48.506
Difference	0.0182	-0.0248	0.030	0.0260	-0.0256	0.0292
OBSV (2016)	432195.604	8764523.447	54.438	432195.604	8764523.447	54.438
OBSV001 (2023)	432195.600	8764523.441	54.424	432195.593	8764523.441	54.430
Difference	0.0040	0.0063	0.0139	0.0108	0.0059	0.0081
QPKT (2016)	432623.966	8764069.509	74.500	432623.966	8764069.509	74.500
QPKT01 (2023)	432623.964	8764069.506	74.488	432623.956	8764069.507	74.494
Difference	0.0025	0.0034	0.0119	0.0096	0.0017	0.0059
SNYE (2016)	432999.112	8763822.749	75.769	432999.112	8763822.749	75.769
SNYE001 (2023)	432999.113	8763822.748	75.764	432999.105	8763822.750	75.770
Difference	-0.0012	0.0008	0.0048	0.0073	-0.0005	-0.0014

the reference stations. The Leica Infinity software outputs different quality parameters for each post-processed GNSS point such as the quality in three dimensions (CQ3D). Low CQ3D values indicated a high post-processing quality. Furthermore, I calculated the differences between each GNSS point's post-processing results from the two different reference stations as an additional parameter to estimate the quality of the post-processing results. If the post-processed coordinates from NYA1 and NYA2 were very close, I assumed that the result was accurate. If the reference stations did not agree, the post-processing result may be less reliable.

For further analyses, I decided to weigh the results according to their quality parameters and to choose the post-processed coordinate from the superior base station for each measurement. I therefore implemented three different sets of quality flags based on a) the three-dimensional quality parameter (QF_CQ3D), b) the vertical offset between NYA1 and NYA2 coordinates (QF_dH) and c) both (QF). QF_CQ3D defined quality classes based on the CQ3D parameter of the higher quality base

station. QF_dH took the absolute height difference (abs_dH) between the two post-processing results from NYA1 and NYA2 into account. And the overall quality flag QF referred to the quality class from QF_CQ3D adjusted to QF_dH by accepting QF_dH classes of 1 and 2 while weighting QF_dH classes of 3 and 4 as negative impact on the overall quality flag. The quality flag criteria are listed in Table A.4.

Table A.4: Criteria of general quality flags for the GNSS measurements - General quality flag (QF) of the post-processed GNSS measurements as a combination of the post-processing quality parameter (QF_CQ3D) and the height difference between the post-processing results from the two base stations (QF_dH).

Quality flag	QF_CQ3D	QF_dH	QF
QF = 1	$CQ3D < 0.01\text{ m}$	$abs_dH < 0.01\text{ m}$	$QF_CQ3D = 1$ and $QF_dH \leq 2$
QF = 2	$0.01\text{ m} < CQ3D < 0.05\text{ m}$	$0.01\text{ m} < abs_dH < 0.1\text{ m}$	$QF_CQ3D = 1$ and $QF_dH > 2$, or $QF_CQ3D = 2$ and $QF_dH \leq 2$
QF = 3	$0.05\text{ m} < CQ3D < 0.1\text{ m}$	$0.1\text{ m} < abs_dH < 1\text{ m}$	$QF_CQ3D = 2$ and $QF_dH > 2$, or $QF_CQ3D = 3$ and $QF_dH \leq 3$
QF = 4	$CQ3D > 0.1\text{ m}$	$abs_dH > 1\text{ m}$	$QF_CQ3D = 3$ and $QF_dH > 3$, or $QF_CQ3D = 4$

A.3.5 Differencing of repeated surveys

To compare the repeated GNSS measurements, I post-processed the raw 2019 measurements based on reference data from both base stations and according to the 2023 base station positions (Figure A.2). I then assigned quality flags (QF_CQ3D, QF_dH and QF) as described above for both the 2023 and the 2019 post-processing results (Table A.4). I subtracted the 2019 from the 2023 coordinates and assigned the highest (i.e. worse) of the two quality flag values (2019_QF or 2023_QF) as combined quality flag (QF_worse) (Figure A.3). In order to obtain annual elevation change values, I averaged the differencing results over the time span of four years between the two measurements. To also account for inaccuracies in the process of locating the exact position of the 2019 survey in the field, I added another component to the overall quality flag of the difference result (QF_diff) by including the absolute horizontal distance between the coordinates from 2019 and 2023 according to the threshold values in Table A.5. I considered measurements with overall quality flags of 1 or 2 to be of high quality. Figure A.3 summarises the subtraction and quality flagging of the repeated measurements.

Table A.5: Criteria of quality flags for repeated GNSS surveys - Quality flag of the differencing result (QF_{diff}) as combination of the general quality flag (QF_{worse}) and the horizontal distance ($diff_distance$) between the repeated measurements as visualised in Figure A.3.

Quality flag	QF_{diff}
$QF_{diff} = 1$	$QF_{worse} = 1$ and $diff_distance \leq 0.1\text{ m}$
$QF_{diff} = 2$	$QF_{worse} < 2$ and $0.1\text{ m} < diff_distance \leq 0.2\text{ m}$, or $QF_{worse} = 2$ and $diff_distance \leq 0.2\text{ m}$
$QF_{diff} = 3$	$QF_{worse} < 3$ and $0.2\text{ m} < diff_distance \leq 0.5\text{ m}$, or $QF_{worse} = 3$ and $diff_distance \leq 0.5\text{ m}$
$QF_{diff} = 4$	$QF_{worse} < 4$ and $diff_distance > 0.5\text{ m}$, or $QF_{worse} = 4$

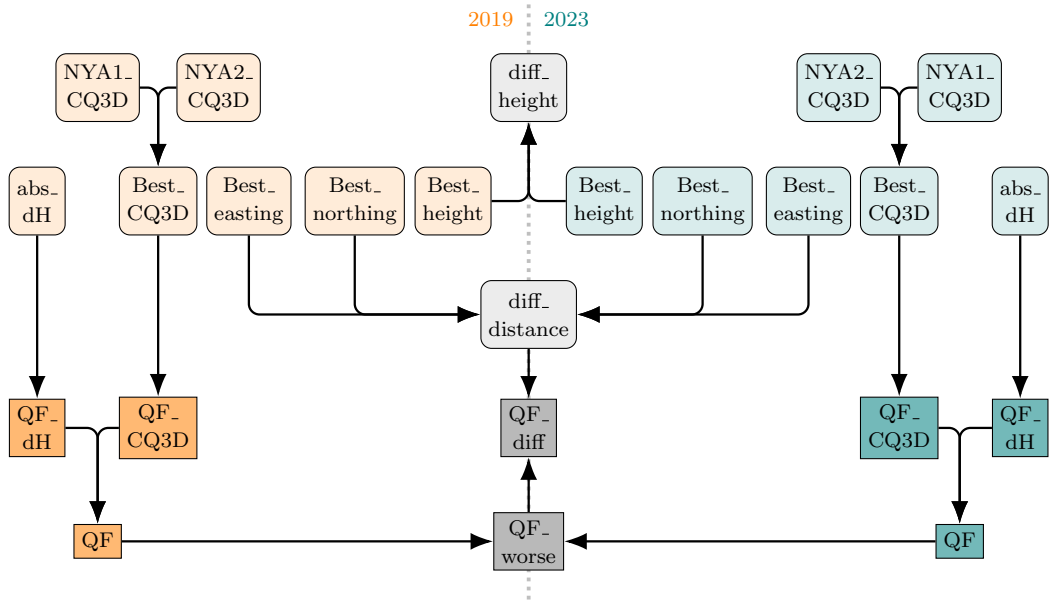


Figure A.3: Schematic overview of the differencing and quality-flagging of repeated GNSS surveys - Variables (light rectangles with rounded corners) and quality flags (darker rectangles) involved in the differencing (gray) of the post-processed GNSS coordinates from 2019 (orange) and 2023 (blue).

A.4 Processing of DEMs

Multi-source DEMs can contain three-dimensional shifts relative to each. However, in order to compare two DEMs, the pixels of each DEM need to represent the same area and location of the surface. Before subtracting the DEMs from each other (Section A.4.3), I therefore resampled (Section A.4.1) and aligned (i.e. coregistered) (Section A.4.2) the DEMs using the Python package xDEM (xDEM contributors 2021).

A.4.1 Resampling

The six DEMs used in this study covered different extents, featured different spatial resolutions, and were based on different coordinate reference systems (Table A.1). Before further processing, all DEMs had to be resampled to fit the geographical information of the reference DEM. For the analyses in the Bayelva basin, I decided to compare the older DEMs to the most recent DEM of 2020. Due to potential sub-meter variations of subsidence (Antonova et al. 2018), I decided to resample all DEMs to the high resolution of the reference DEM. Resampling to lower resolutions may improve comparability among DEMs but would result in a loss of detail. I therefore used the xDEM tool to resample and to reproject the older DEMs to the reference DEM with a pixel size of 0.15 m and the coordinate system EPSG:32632.

A.4.2 Coregistration

The multi-level processing of stereo-imagery to generate DEMs potentially leads to errors that can not easily be determined or reconstructed. Differences in image matching algorithm, DEM resolution and extent or simply the vertical and horizontal reference system can cause offsets between two DEMs. Coregistration aims at removing shifts, scales, tilts or rotations between the DEMs. Most approaches use statistical methods to minimize stable terrain elevation residuals (Nuth and Kääb 2011). Due to glacial, fluvial, and periglacial processes, stable terrain in the Bayelva basin is rare. I therefore included terrain with relative little vertical movement in the coregistration and only masked glaciers, moraines and the Bayelva river bed. I used, combined and compared the following statistical coregistration methods implemented in the xDEM tool (xDEM contributors 2021):

Nuth and Kääb

The coregistration approach by Nuth and Kääb (2011) uses a cosine equation to model and correct the most likely offset between DEMs and is recommended for noisy data with low rotational differences (Mannerfeld et al. 2021b). The approach is based on the assumption that two DEMs that are not perfectly aligned experience a characteristic relationship between elevation error and terrain aspect and slope. Elevation errors are negative on western slopes, positive on eastern slopes and larger on steeper slopes. This relation can be described as:

$$dh = a \cdot \cos(b - \Psi) \cdot \tan(\alpha) + \bar{d}h \quad (1)$$

where for each pixel, dh is the elevation error, a and b are magnitude and direction of the horizontal shift, Ψ is the terrain aspect in degrees circular from the north, α is the terrain slope in degrees, and $\bar{d}h$ is the overall elevation bias between the two DEMs (Kääb 2005). In order to reduce the elevation error, Nuth and Kääb (2011) calculate the difference of the unaligned DEMs and create slope and aspect maps from the reference DEM. Then the slope-dependent shift is being normalized in order to solve Equation 1 using least squares minimization on a pixel-level. The

process is being iterated to continuously refine the total offset until an iteration limit is reached or the elevation error stops improving significantly. The final correction is then being applied as shift vector to the coordinates of the unaligned DEM.

Tilt

The tilt correction applies a first-order polynomial function to the elevation offset between two DEMs. It estimates and corrects tilts and small rotations of the two-dimensional plane of the DEM to be aligned to the reference DEM. As it does not account for horizontal shifts, it is recommended to be combined with other coregistration approaches such as Nuth and Kääb (Mannerfeld et al. 2021b).

Vertical shift

The vertical shift performs a vertical correction based on statistics of the elevation offset between two DEMs. Its functionality is very similar to the z-component of the Nuth and Kääb approach but it allows to customize the statistical algorithm (e.g. weighted mean or median). As it only accounts for vertical shifts, it should always be combined with other approaches (Mannerfeld et al. 2021b).

Non-global bias corrections

The xDEM tool (xDEM contributors 2021) furthermore provides bias-correction methods that perform non-rigid non-affine transformations of the input DEMs. While global coregistration approaches are solely based on the information in the DEMs, bias corrections can include external variables. However, many methods still use information derived from the DEMs for e.g. along-track or elevation-dependant corrections. One possibility to account for non-global shifts is to perform any of the above mentioned coregistration algorithms in a blockwise manner. The DEMs get subdivided into an arbitrarily small grid and the coregistration algorithm is being applied to each block separately. The results are then being interpolated and warped to maintain the aligned DEM.

After testing and combining different coregistration and bias correction approaches, I decided to exclude some algorithms due to very high processing times or implausible coregistration results. For the most promising approaches, I estimated the coregistration quality statistically by calculating the median (Mdn) and the normalized median absolute deviation (NMAD) of the stable terrain elevation residuals after coregistration. The Mdn represents the central tendency of the residuals and therefore analyses the accuracy of the coregistered DEM, while the NMAD depicts the spread of the residuals and therefore shows the precision of the coregistration results. Both Mdn and NMAD are less sensitive to outliers than mean and standard deviation and are therefore useful when working with unfiltered DEMs (Mannerfeld et al. 2021b). Lower Mdn and NMAD values indicated higher accuracy and precision (Figure A.4). Besides these statistical parameters, I assessed the coregistration quality visually by comparing the differencing results from the aligned DEMs (Figure A.4). I chose the Nuth and Kääb algorithm for most alignments as it seemed to

perform best based on the statistical parameters. Only when aligning the 2010 to the 2020 DEM, I chose a combined approach of the tilt and Nuth and Kääb algorithms as I visually recognised relatively high subsidence trends towards the coast compared to the other DEMs.

A.4.3 Differencing and vertical offset correction

To calculate elevation changes, I subtracted the aligned DEM from the reference DEM. I expected DEM differencing results to be zero for bedrock outcrops after successful DEM alignment. For the alignment process, however, I also considered areas as stable that were likely to face small-scale elevation changes (Section A.4.2). Despite coregistration, vertical offsets were therefore still possible and needed to be accounted for. I calculated median vertical offsets for each aligned DEM by extracting the DEM differencing results for bedrock points that I GNSS-surveyed during the field campaign in summer 2023 (Section A.2.2, Figure 2). In the Bayelva basin, all aligned DEMs except for the 2019 DEM showed elevation gain on bedrock of several decimeter which I considered unrealistic. I therefore decided to correct these DEMs vertically by the median offset. Unfortunately, the 1995 DEM did not cover any bedrock measurements. I therefore manually identified areas that appeared stable in the aligned and offset-corrected DEMs from 2010 and 2008 and calculated the median offset from the 1995 DEM for these areas. Table A.6 summarises the final selection of coregistration approaches and vertical offset corrections.

Table A.6: Overview of the aligned DEMs - Aligned and reference DEMs, length of observation period, selected coregistration approach, and vertical offset correction. Coregistration results that involve the 2020 reference DEM cover the Bayelva basin. The 1936-2010 coregistration covers the Brøgger peninsula.

Aligned DEM	Reference DEM	Period length	Best-performing coregistration approach	Vertical offset correction
2019	2020	1 year	Nuth and Kääb	-
2010	2020	10 years	Nuth and Kääb + Tilt	-0.27 m
2008	2020	12 years	Nuth and Kääb	-0.33 m
1995	2020	25 years	Nuth and Kääb	-0.68 m
1936	2020	84 years	Nuth and Kääb	-5.35 m
1936	2010	74 years	Nuth and Kääb	-2.78 m

A.4.4 Assessing the temporal component of change

The absolute elevation differences cover periods of different lengths. In order to compare elevation change results across DEMs, I therefore calculated annual elevation change rates by dividing the differencing results by the length of the observation period. Most of my analyses were based on these annual elevation change values averaged for the period between aligned and reference DEM. These periods partially overlap as they all referred to the same reference DEM from 2020 (Figure A.5).

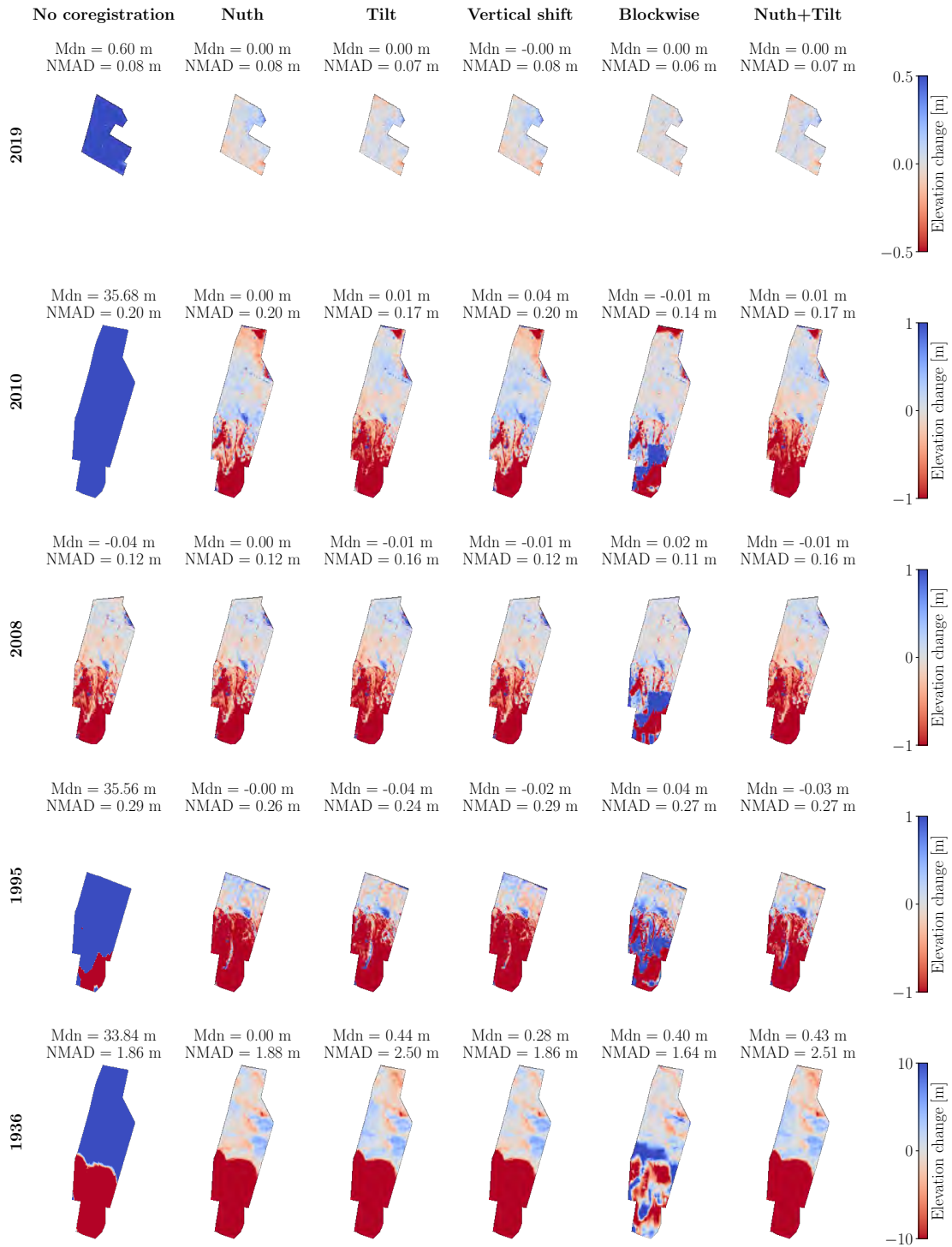


Figure A.4: Visual and statistical comparison of coregistration algorithms - Median (Mdn) and normalized median absolute deviation (NMAD) of stable terrain residuals indicate accuracy and precision of each approach statistically, the elevation differencing map compares the aligned DEM to the reference DEM from 2020 visually.

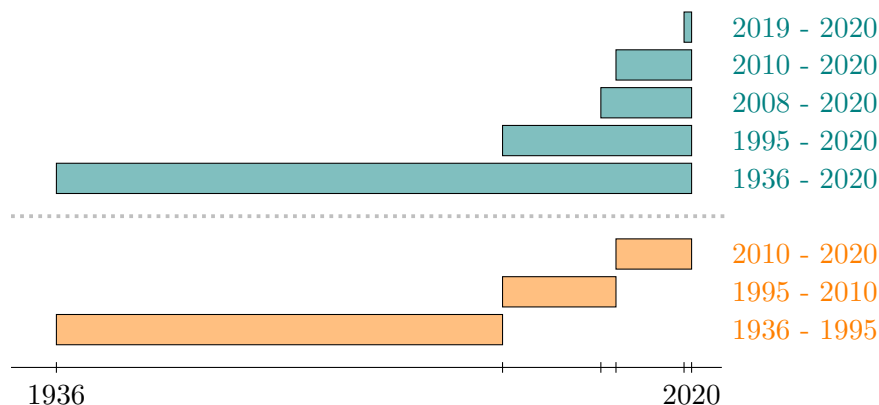


Figure A.5: Schematic overview of overlapping and non-overlapping observation periods - Elevation change was mainly calculated for the whole period between aligned DEM and reference DEM (blue), but for the assessment of the temporal component of change non-overlapping time periods (orange) were subsetting.

In order to further assess the temporal component of elevation change, I furthermore quantified elevation change for non-overlapping time periods. I therefore subtracted differencing results from each other to subset the differencing results into the three periods of 1936-1995, 1995-2010, and 2010-2020 (Figure A.5). I decided to exclude DEMs from 2008 and 2019 from the temporal subsets to ensure longer time periods of at least 10 years. To compare the time periods to each other, I again calculated annual averages for each period.

A.5 Processing of satellite imagery

I used four-band SkySat imagery (Planet Labs PBC 2023) from spring and summer 2023 (Section A.1.4) to detect vegetation and snow cover. Despite Planet’s orthorectification processes, I recognised a spatial offset between different SkySat scenes that varied in direction and reached up to 20 m (Figure A.6). In order to eliminate these offsets, I manually relocated each scene using the Freehand raster georeferencer tool (Vellut 2021) in QGIS and the aerial orthophotos from 2020 and 2010 as reference. To minimize spatial misfits, I decided to avoid any rotations or scaling of the images and restricted the relocation to shifts in x- and y-directions. The Freehand raster georeferencer tool exported a world file containing an affine transformation that I then applied to each image using GDAL’s SetGeoTransform function (GDAL/OGR contributors 2024).

A.6 Landscape classification

In order to analyse spatial variations in elevation change trends across the Bayelva basin (RQ1), I compared general elevation change across different landscapes. I therefore divided the footprint of the reference DEM into water bodies and ocean, mountains, glaciers, moraines, river beds, anthropogenic, and periglacial landscapes. I based the classification on topographic vector data provided by the Norwegian Po-

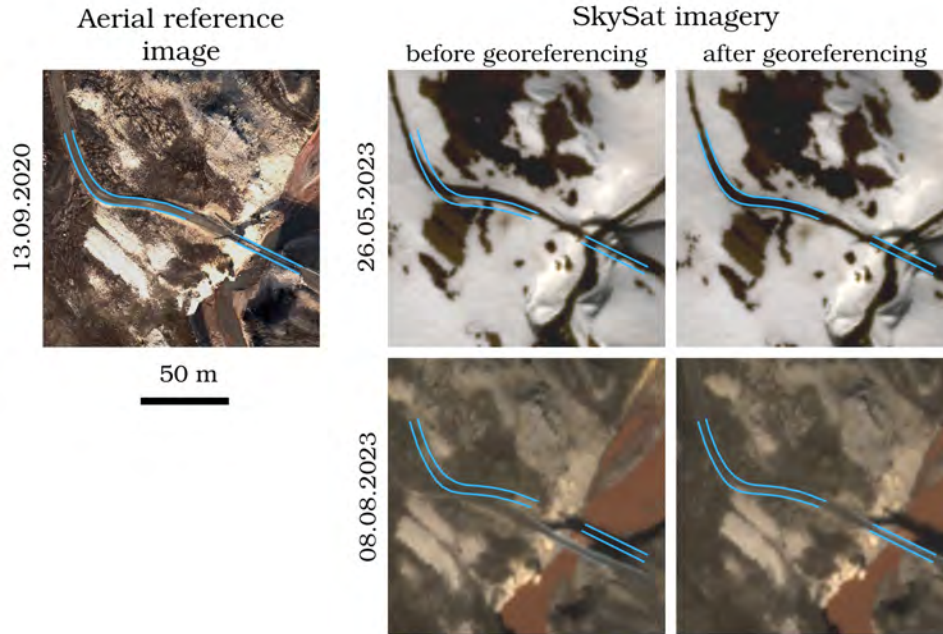


Figure A.6: SkySat imagery before and after manual georeferencing - The aerial reference image (left) with the blue outlines of a road and a bridge in the Bayelva basin shows the spatial offset in SkySat images of two example dates (right). Manual georeferencing improved the spatial fit of the images. (SkySat imagery: Planet Labs PBC (2023)).

lar Institute (2014b) that outlined glaciers, moraines, river beds, and shorelines. I furthermore manually classified mountains and anthropogenic areas through visual inspection of aerial imagery. I considered almost all terrain above 100m mountainous that was not included in the glacier or moraine classes. An exception was a high-elevation plateau in the northwest of the peninsula with similar tundra characteristics as the low-land. The mountainous landscape was generally rocky and rather steep. I classified areas as anthropogenic landscape that were visually dominated by non-natural processes. The anthropogenic landscape class therefore included the whole village of Ny-Alesund, the airport, artificial lakes, and other infrastructure such as roads, bridges, and buildings, as well as their direct surrounding. Through spatial differencing, I finally classified the remaining low-elevation areas as periglacial landscape which was mainly characterised by a hilly terrain and by low to moderate tundra vegetation cover. Patterned ground in the form of e.g. sorted circles or sorted stripes was a wide-spread phenomenon in the periglacial landscape and indicated the presence of permafrost. I extracted landscape class and elevation change results for 10000 random sample points across the footprint of the 2020 DEM to examine general elevation change in the Bayelva basin.

Both NPI's topographic data and my own landscape classifications were mainly based on aerial imagery from 2010. I used aerial imagery from 2020 to adjust the anthropogenic class for any infrastructure around Ny-Alesund that was built in more recent years. Some landscape classes - especially fast-changing glaciers - were likely to show variable outlines throughout the years that were not captured by this static classification. I assumed, however, that the spatial extent of the periglacial areas

was relatively stable throughout the study period as it was not directly impacted by glaciers. Due to the focus of my study on permafrost landscapes and for matters of consistency, I decided to use this static landscape classification although it may not correctly represent the different landscapes in all years. This deviation had to be considered in the different analysis steps and partially led to the exclusion of specific time steps (e.g. moraines in Figure 3).

A.7 Surface classifications

In RQ2, I aimed at further investigating elevation change in the periglacial landscape by investigating land surface properties. I therefore mapped terrain forms (Section A.7.1), vegetation cover (Section A.7.2) and snow disappearance timing (section A.7.3) in periglacial areas. I then created a sample of 5000 random points within a periglacial Bayelva core area that was covered completely by all DEMs except for the 2019 DEM (Figure 1). Through visual inspection of the orthophoto from 2020, I filtered about 500 sample points that were located in river beds, in anthropogenic areas, or at the edges of moraines (e.g. due to landscape changes or resolution of the landscape classification). I furthermore masked an area parallel to the airport that showed elevation gain of several decimeter. Due to its geometric form and location, I assumed an artificial earth deposit. I moreover identified snow patches in some orthophotos leading to elevation gain in some DEM differences that were not related to the actual surface elevation. This was particularly the case for the 2008 flight campaign that took place earlier during summer than the other campaigns. For the terrain form and vegetation analyses, I filtered all sample points within the remaining snow patches to eliminate potential bias. However, I decided to keep these samples for all DEMs except for the one from 2008 for the analysis of snow disappearance as they made up a majority of the class with the latest snow disappearance timing.

For the sake of simplicity, I used static classifications of terrain forms, vegetation cover, and snow disappearance timing. I assume that relative inter-annual vegetation and snow patterns were mainly controlled by parameters that did not change radically from year to year (e.g. topography, micro-climate) and were therefore persistent in space (Sturm and Wagner 2010). Especially since earlier observation periods, however, spatial patterns may have undergone change processes that cannot be captured adequately by a single classification. The comparison of the 1936 DEM to NDVI calculations and snow cover observations in 2023 could be biased in that respect.

A.7.1 Terrain forms

Terrain forms are land features with characteristic topographic patterns. I used the pattern-based classification tool Geomorphons (Jasiewicz and Stepinski 2013) to detect different terrain forms. For each pixel of a DEM, the Geomorphons tool compares its elevation to its visibility neighbours along the eight principal compass directions (Figure A.7). The tool assigns a tuple to each DEM cell indicating if the

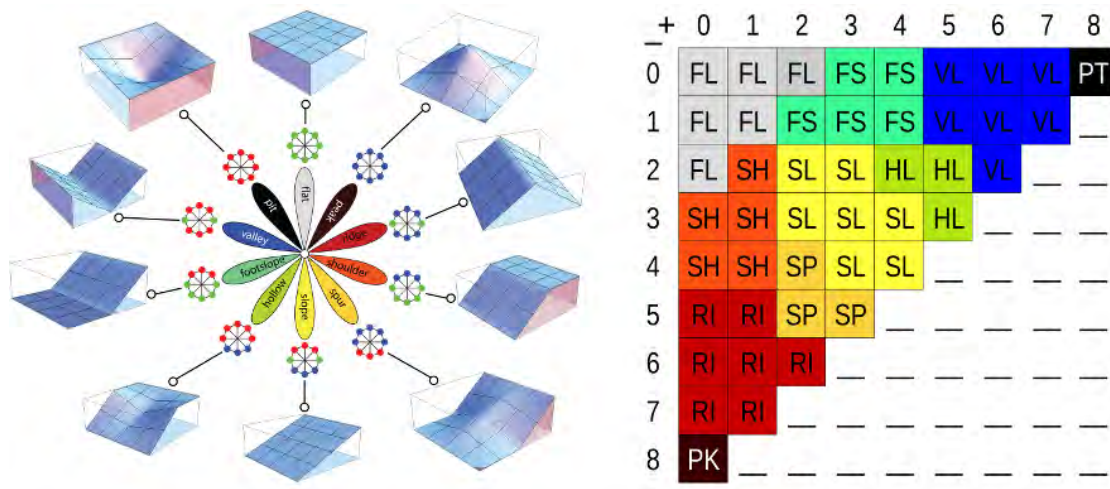


Figure A.7: Concept of Geomorphons by (Jasiewicz and Stepinski 2013) - There are ten terrain forms described by the Geomorphons tool: Flat, peak, ridge, shoulder, spur, slope, hollow, footslope, valley, and pit. The tool determines visibility neighbours of each pixel and indicates if they are lower (blue dots), higher (red dots), or at same elevation (green dots) as the respective pixel (left). Terrain forms are then set based on the sum of lower (-) and higher (+) neighbours (right) (image taken from Jasiewicz and Stepinski (2023)).

eight visibility neighbours show the same, a higher or a lower elevation. The different possible tuple combinations are then assigned to the ten most common terrain forms: peak, ridge, shoulder, spur, slope, hollow, footslope, valley, pit, and flat. Visibility neighbours are not the directly neighbouring pixels, but pixels determined from the line-of-sight principle. Size and shape of the neighbourhood therefore changes for each DEM pixel and self-adapts to the local topography which enables the identification of land forms at wider scales.

I classified the terrain forms based on the 2010 DEM as it covered the whole peninsula and I considered the resolution of 5 m sufficient to identify medium-scale patterns. Within the settings of the Geomorphons tool, I chose to skip the first three cells and set the maximum search radius to 50 cells for the determination of visibility neighbours. I considered slopes of less than 2 degrees as flat. In order to simplify my analysis, I furthermore merged related classes (peak and ridge, shoulder and spur, hollow and footslope, valley and pit), resulting in a terrain form map with a total of six classes (Figure 5a).

A.7.2 Vegetation cover

I assessed vegetation cover based the Normalized Difference Vegetation Index (NDVI), which indicates the greenness of vegetation cover and hence its density and productivity (Tucker and Sellers 1986). Its calculation is based on the visible red (RED) and near-infrared (NIR) bands:

$$NDVI = \frac{NIR - RED}{NIR + RED} \tag{2}$$

I calculated the NDVI from manually georeferenced SkySat imagery (Planet

Labs PBC 2023) (Section A.5). I chose a relatively cloud-free image from early August (08.08.2023) when I assumed vegetation activity to be highest. Before NDVI calculation, I masked cloud and cloud shadows using the quality assessment image provided by Planet (Planet Labs PBC 2023).

A.7.3 Snow detection

I also used SkySat imagery (Planet Labs PBC 2023) to map multi-temporal snow cover and to classify approximate timing of snow disappearance. For this purpose, I selected four relatively cloud-free Planet images between end of May and beginning of July with a temporal interval of roughly two weeks (11-15 days). On the first (26.05.2023) and the second date (06.06.2023), the study area was mainly snow-covered with first barely and then few isolated snow-free patches. On the third date (21.06.2023), the study area was about half snow-covered and half snow-free. The fourth date (04.07.2023) showed a mainly snow-free periglacial landscape with only very few remnants.

Snow cover is often detected by the Normalized Difference Snow Index (NDSI) which combines the visible green and a short-wave infrared band. The NDSI approach was not possible with the four-band SkySat imagery as it did not include a short-wave infrared band. Thaler et al. (2023) showed the possibility to identify snow cover on Planet's imagery using a blue-band threshold approach. However, their Blue Snow Threshold (BST) algorithm suggests a threshold for the blue band that failed to detect snow in some of the images that I used in my study. One reason might be the differences in brightness due to low sun angles in high latitudes. I therefore expanded their idea of thresholding the blue band and decided for an individual threshold on a scene basis. I manually collected 50 sample points from both snow-free and snow-covered areas. I then extracted the blue reflectance value at the point locations from each scene and calculated the minimum blue value for snow-covered and the maximum for snow-free pixels. I assumed that the threshold had to lay in the middle between the snow-covered minimum and the snow-free maximum blue value and therefore set the average as blue threshold. I masked each scene based on the blue threshold to generate binary snow cover information. As some scenes did not cover the whole study area, I created image composites resulting in one binary snow cover map for each of the four dates.

In order to derive the approximate timing of snow disappearance, I changed the snow information to date-specific values for snow-covered pixels: 1000 for snow cover on the first date, 100 on the second date, 10 on the third date, and 1 on the fourth date. Snow-free pixels showed the value 0. I then stacked and added the snow cover maps to each other to receive the following five-level snow melt classification: 0 as very early, 1000 as early, 1100 as medium, 1110 as late, and 1111 as very late snow melt (Table A.7). Some pixels did not fit into either of the five classes and were excluded from the analysis. The locations of excluded pixels in river beds or north of mountains suggest varying reflectance values for water and shadows. Other excluded pixels bordered snow structures and could result from inaccuracies in the

georeferencing procedure (Section A.5).

Table A.7: Classification of snow cover disappearance - Dates of the SkySat images (Planet Labs PBC 2023) used for snow cover detection and overview on the classification of approximate snow disappearance timing (0 for snow-free, 1 for snow-covered).

Snow disappearance timing	26.05.	06.06.	20.06.	04.07	Sum
very early	0	0	0	0	0
early	1	0	0	0	1000
medium	1	1	0	0	1100
late	1	1	1	0	1110
very late	1	1	1	1	1111

A.8 Transfer to the surrounding Brøgger peninsula

To answer RQ3, I compared periglacial elevation change rates in the Bayelva basin to its surrounding by transferring and adjusting most above-mentioned analysis steps (Sections A.4-A.7) to the broader Brøgger peninsula. I calculated elevation change from the two peninsula-covering DEMs from 1936 and 2010. Resampling was not necessary as both DEMs already shared the same spatial resolution and coordinate reference system (Table A.1). I aligned the 1936 DEM to the 2010 DEM using the xDEM tool (xDEM contributors 2021) with the Nuth and Kääb coregistration algorithm (Nuth and Kääb 2011). I then subtracted the aligned from the reference DEM and corrected the results for a vertical shift of -2.78 m (Table A.6) based on median offsets at bedrock locations in the Bayelva basin and on Kvadehuksletta (Figure 2). Finally, I calculated an annual average over the period of 74 years between the two DEMs.

Due to its diverse landscape characteristics, I divided the peninsula into three regions for further analyses (see Figure 1b). The Kvadehuksletta at the tip of the peninsula mainly encompasses periglacial landscapes with relatively flat terrain, few vegetation, and vast patterned ground. The rest of the peninsula is characterised by hilly and mountainous landscapes with glaciers and moraines (Section 2). In the orthophoto from the 1936 flight campaign, the southern coast of the peninsula was partially blurry and cloud-covered. As this may impact on the quality of the DEM and therefore also on the elevation change results, I excluded the southern peninsula from my analysis. To assess RQ3, I therefore compared elevation change trends between 1936 and 2010 from the Bayelva basin to the Kvadehuksletta and the northern peninsula only.

I extended the classification of landscapes (Section A.6) and surface properties (Section A.7) to the Brøgger peninsula. Landscape and terrain classifications were transferrable to the wider area as they were based on Svalbard-wide topographic data (Norwegian Polar Institute 2014b) and the peninsula-covering 2010 DEM (Norwegian Polar Institute 2014a). Expanding the vegetation cover and snow disappearance

classifications was more work-intensive, as they were based on SkySat imagery that did not cover the whole Brøgger peninsula. I therefore had to include SkySat scenes with different cloud-covers and illumination which posed many challenges in the process of georeferencing, NDVI calculation, and snow cover detection. In particular the transitions from one SkySat scene to the other were prone to error. Due to the different illumination of scenes, I decided to only include one SkySat image from 03.08.2023 in the vegetation cover estimation. The image was captured only five days earlier than the one used for the analysis in the Bayelva basin and covers most of the periglacial areas in the northern peninsula and on the Kvadehuksletta. For snow cover detection, I chose the same dates as for the Bayelva analysis. Only for the third snow date, I had to include two images from the 21.06.2023, as the northern tip of the peninsula was completely cloud-covered in the imagery from 20.06.2023. Nevertheless, I still had to mask large areas on the Kvadehuksletta and north of the Bayelva basin as snow detection was not possible for all dates due to data gaps. In the Bayelva basin, I used the minimum blue reflectance value of snow-covered and the maximum of snow-free areas to estimate a blue snow threshold as described in Section A.7.3. This approach did not succeed for peninsula-wide SkySat scenes as they covered wide areas with diverse snow, surface, and illumination characteristics. I therefore identified threshold values manually by applying, evaluating, and adjusting different threshold values on a scene-basis.

To finally assess elevation change among the regions, I sampled and compared annual elevation change results between 1936 and 2010 for the Kvadehuksletta, the northern peninsula, and the Bayelva basin. I created a random sample of 10000 points to compare all landscapes and another random sample of 10000 points to compare only periglacial elevation change. For the Bayelva basin, I used the same random sample of the core DEM area as in Section A.7. I then filtered the samples according to the data coverage and extracted elevation change values and landscape, terrain form, vegetation cover, and snow disappearance classes.

B Extended results

In the following, I provide further information on the observations presented in section 4. This section includes complementing figures on e.g. the spatial distribution of the observed changes and tables with detailed statistical parameters that are visualised in section 4.

B.1 General elevation change results in the Bayelva basin

Table B.1: Statistics of general elevation change results in the Bayelva basin - Sample count, median, mean, standard deviation, minimum, and maximum for each landscape and DEM differencing period (visualised in Figure 5).

Landscape	Period	Elevation change statistics [m/year]					
		count	median	mean	std	min	max
Periglacial	1936-2020	2200	-0.064	-0.067	0.058	-0.764	0.012
	1995-2020	971	-0.027	-0.027	0.022	-0.174	0.158
	2008-2020	1770	-0.028	-0.028	0.012	-0.129	0.085
	2010-2020	2200	-0.026	-0.026	0.017	-0.121	0.099
River beds	1936-2020	574	-0.082	-0.101	0.058	-0.434	-0.051
	1995-2020	397	-0.022	-0.023	0.016	-0.124	0.028
	2008-2020	574	-0.029	-0.026	0.023	-0.129	0.098
	2010-2020	574	-0.026	-0.025	0.027	-0.146	0.101
Anthropogenic	1936-2020	143	-0.023	-0.027	0.031	-0.093	0.156
	1995-2020	0	-	-	-	-	-
	2008-2020	124	-0.023	-0.005	0.114	-0.207	0.893
	2010-2020	143	-0.016	0.015	0.159	-0.049	1.499
Moraines	1936-2020	-	-	-	-	-	-
	1995-2020	1508	-0.129	-0.326	0.414	-2.111	0.086
	2008-2020	1508	-0.089	-0.209	0.353	-2.469	0.163
	2010-2020	1508	-0.114	-0.220	0.356	-2.593	0.065
Glaciers	1936-2020	575	-1.185	-1.190	0.076	-1.411	-1.014
	1995-2020	575	-1.704	-1.715	0.163	-2.172	-1.139
	2008-2020	572	-2.068	-2.016	0.335	-2.731	-0.610
	2010-2020	575	-2.238	-2.205	0.339	-2.917	-0.403

B.1.1 Quality of the 2019 DEM differencing results

Figure B.1 shows elevation change results from the DEM differences for 1936-2020, 1995-2020, 2008-2020, 2010-2020, and 2019-2020. Spatial elevation change patterns appeared similar for 1995-2020, 2008-2020, and 2010-2020. Elevation loss was generally more pronounced in 1936-2020. The 2019 DEM produced very noisy differencing results with both high positive and negative elevation changes compared to the other

DEM differences. In particular the elevation gain patterns were not captured by the other DEM differences. I clearly recognised geometric patterns along the flight lines of the aerial photography mission in the 2019-2020 differences. An insufficient large overlap of the aerial images could be one reason for an inadequate generation of the 2019 DEM resulting in noise. I therefore decided to exclude the 2019 DEM from the analyses.

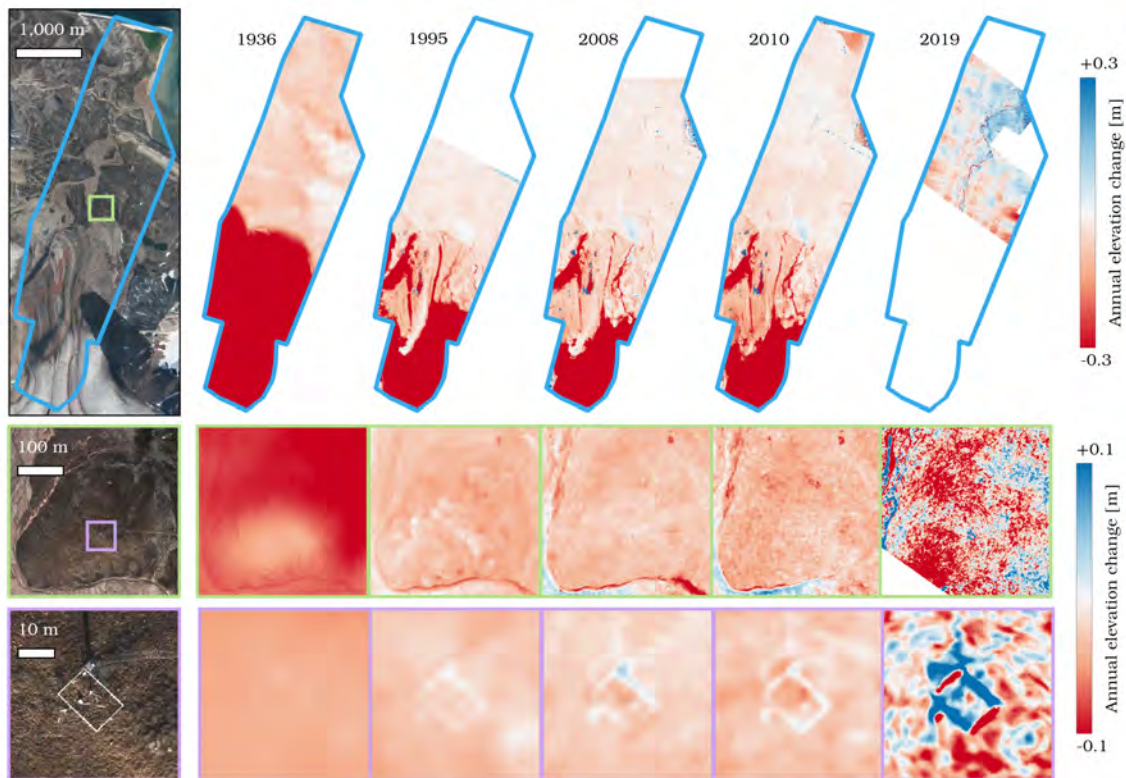


Figure B.1: Spatial patterns of general elevation change in the Bayelva basin - Aerial image (left) and maps of annually averaged elevation change results (right). Elevation change calculated from the 2020 reference DEM (blue outline) and the aligned DEMs from 1936, 1995, 2008, 2010, and 2019. Presented for different zoom levels: the whole Bayelva basin (top), the Leirhaugen hill (center), and the Bayelva observatory (bottom). (Aerial imagery and DEMs: Boike et al. (2018); Geyman et al. (2022); Norwegian Polar Institute (2014a), as well as unpublished DEMs by AWI, DLR, NORCE, and NPI).

B.1.2 Spatial distribution of GNSS-derived results

Figure B.2 shows the spatial distribution of the 39 repeated GNSS measurements in the surrounding periglacial area of the Bayelva observatory. During comparison to the 2019-2020 DEM differences, I recognised comparable local patterns at very different magnitudes of change. Both the repeated GNSS measurements and the 2019 DEM for example detected marginal elevation gain trends on a plateau northeast of Leirhaugen hill and heave and subsidence on two sides of a fence north of the Bayelva observatory (zoomed-in map in Fig. B.2). Despite its noise, the 2019 DEM seemed to capture valuable elevation change patterns on smaller spatial scales.

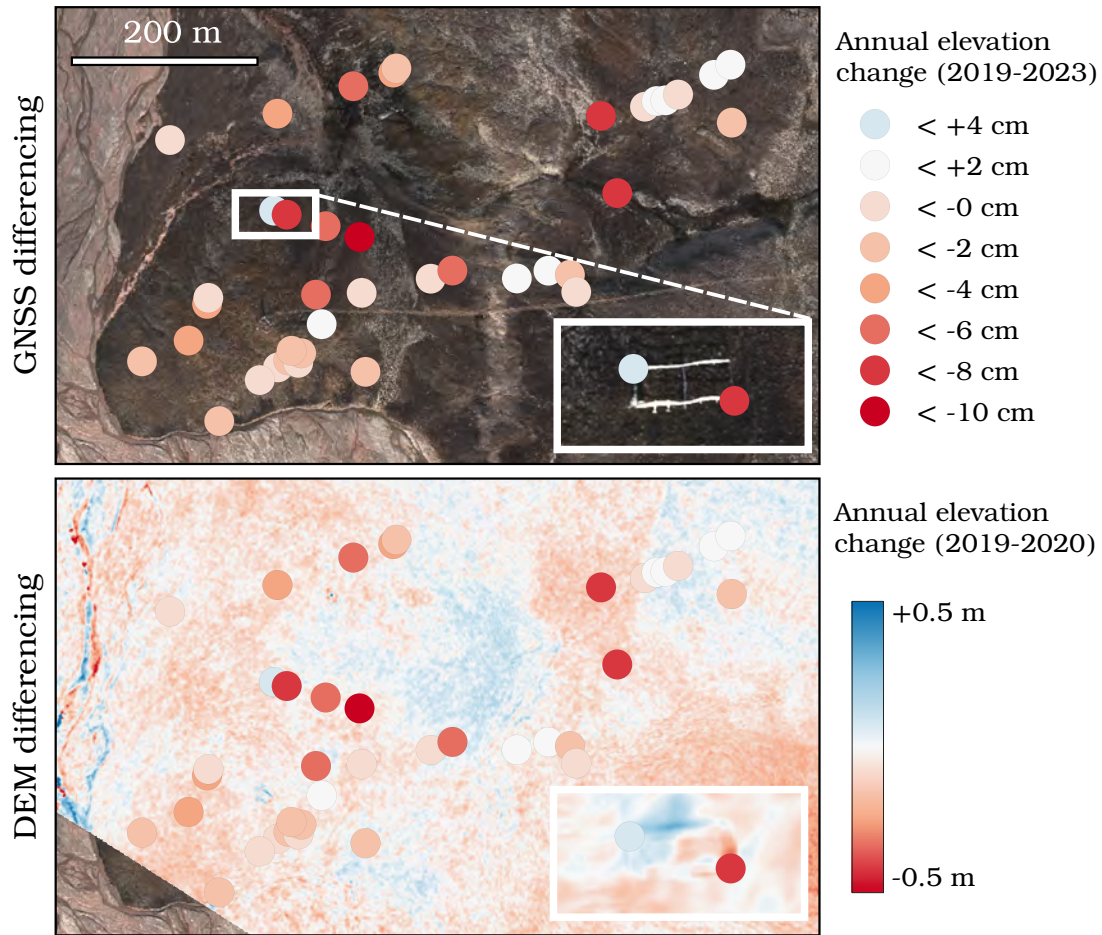


Figure B.2: *Spatial distribution of the repeated GNSS measurements - Annually averaged elevation change results (2019-2023) at point locations of repeated GNSS survey and its spatial distribution compared to an aerial image (top) and to 2019-2020 DEM differences (bottom) with zoom on fence north of the Bayelva observatory (bottom right corners). (Aerial imagery and DEMs by AWI, DLR, NORCE (unpublished), 2019 GNSS coordinates by Lange et al. (2020)).*

B.1.3 Comparison of DEM- and GNSS-derived elevation change results

Table B.2: *Statistics of elevation change results at GNSS measurement locations in the Bayelva basin - Point count, median, mean, standard deviation, minimum, and maximum for repeated GNSS measurements and extracted DEM differences at the same measurement locations (visualised in Figure 4).*

Method	Period	Elevation change statistics [m/year]					
		count	median	mean	std	min	max
GNSS differencing	2019-2023	39	-0.005	-0.007	0.008	-0.029	0.007
DEM differencing	1936-2020	39	-0.056	-0.057	0.034	-0.108	0.003
DEM differencing	1995-2020	39	-0.030	-0.029	0.012	-0.050	-0.004
DEM differencing	2008-2020	39	-0.029	-0.028	0.009	-0.055	-0.013
DEM differencing	2010-2020	39	-0.026	-0.027	0.016	-0.070	-0.003
DEM differencing	2019-2020	39	-0.021	-0.018	0.073	-0.194	0.188

B.1.4 Temporal component of general elevation change

To assess the temporal component of elevation change in the Bayelva basin further, I subsetting the differencing results into the three time periods of 1936-1995, 1995-2010, and 2010-2020 (Fig. A.5). Figure B.3 and Table B.3 compare elevation change rates across landscapes and time periods. For periglacial landscapes and river beds, elevation loss rates decreased by -6 cm/year and -8 cm/year, respectively, from the first to the second period before stabilising. Anthropogenic terrain was barely covered by the 1995 DEM and therefore could not be compared across time periods. Moraines showed consistent elevation loss rates during the second and third periods, but had to be excluded from the first as they were still glaciated in 1936. Glacial elevation loss rates increased from -97.3 ± 5.9 cm/year in 1936-1995 to -220.3 ± 36.0 cm/year in 2010-2020. Observed temporal patterns were similar for both overlapping (i.e. period between aligned DEM and 2020 reference DEM) and non-overlapping observation periods (Figure 3). For reasons of simplicity, I therefore decided to restrict the temporal component to this extended results section.

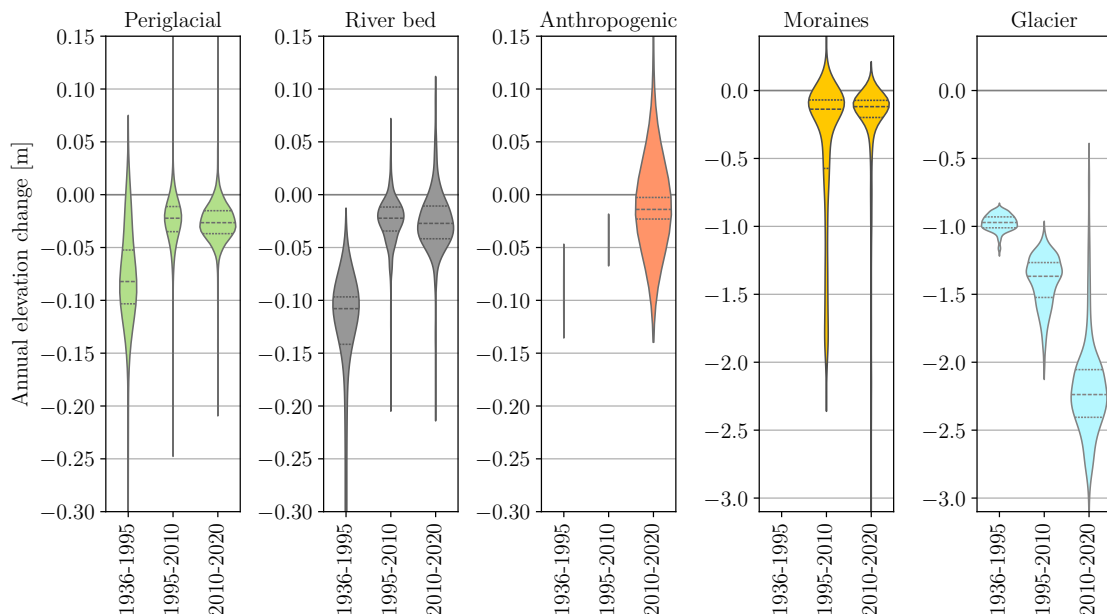


Figure B.3: Temporal component of elevation change in the Bayelva basin - Elevation change results from DEM differencing subsetting into three time periods (1936-1995, 1995-2010, and 2010-2020) and compared across landscapes. Please note that in 1936 glaciers covered parts of the current moraine area and the moraine changes are therefore excluded at this time frame. (Landscape classification based on Norwegian Polar Institute (2014b)).

Table B.3: Statistics of general elevation change results for non-overlapping time periods - Sample count, median, mean, standard deviation, minimum, and maximum for each landscape and subsetting for non-overlapping time periods of 1936-1995, 1995-2010, and 2010-2020 (visualised in Figure B.3).

Landscape	Period	Elevation change statistics [m/year]					
		count	median	mean	std	min	max
Periglacial	1936-1995	2097	-0.082	-0.092	0.111	-1.062	0.027
	1995-2010	2097	-0.022	-0.021	0.039	-0.231	0.301
	2010-2020	4448	-0.026	-0.026	0.019	-0.202	0.177
River beds	1936-1995	835	-0.108	-0.147	0.101	-0.623	-0.066
	1995-2010	835	-0.022	-0.024	0.021	-0.194	0.061
	2010-2020	1143	-0.027	-0.025	0.029	-0.200	0.098
Anthropogenic	1936-1995	2	-0.091	-0.091	0.018	-0.104	-0.078
	1995-2010	2	-0.043	-0.043	0.010	-0.050	-0.036
	2010-2020	262	-0.014	0.009	0.131	-0.054	1.481
Moraines	1936-1995	-	-	-	-	-	-
	1995-2010	3163	-0.137	-0.423	0.556	-2.140	0.422
	2010-2020	3163	-0.119	-0.234	0.378	-2.969	0.062
Glaciers	1936-1995	984	-0.971	-0.973	0.059	-1.189	-0.859
	1995-2010	984	-1.367	-1.408	0.187	-2.033	-1.057
	2010-2020	984	-2.238	-2.203	0.360	-3.094	-0.571

B.2 Surface classifications in the Bayelva basin

B.2.1 Sample size per surface property class in the Bayelva basin

To analyse elevation change across different surface properties, I sampled the periglacial core DEM area in the Bayelva basin at 5000 random locations. Figure B.4 shows the sample size of each surface class. As the sample was randomly stratified, I assumed sample sizes to be proportional to the actual area covered by the respective surface class. Some classes clearly prevailed, while others made up only marginal shares of the periglacial landscape in the Bayelva basin. One third of the terrain forms were slopes, while less than 5 % were valley forms. About half of the vegetation samples had NDVI values between 0.2 and 0.4 while negative values and values greater than 0.5 were barely present. The great majority of the samples showed a medium or late snow disappearance while the very early, early, and very late classes together made up less than 10 %.

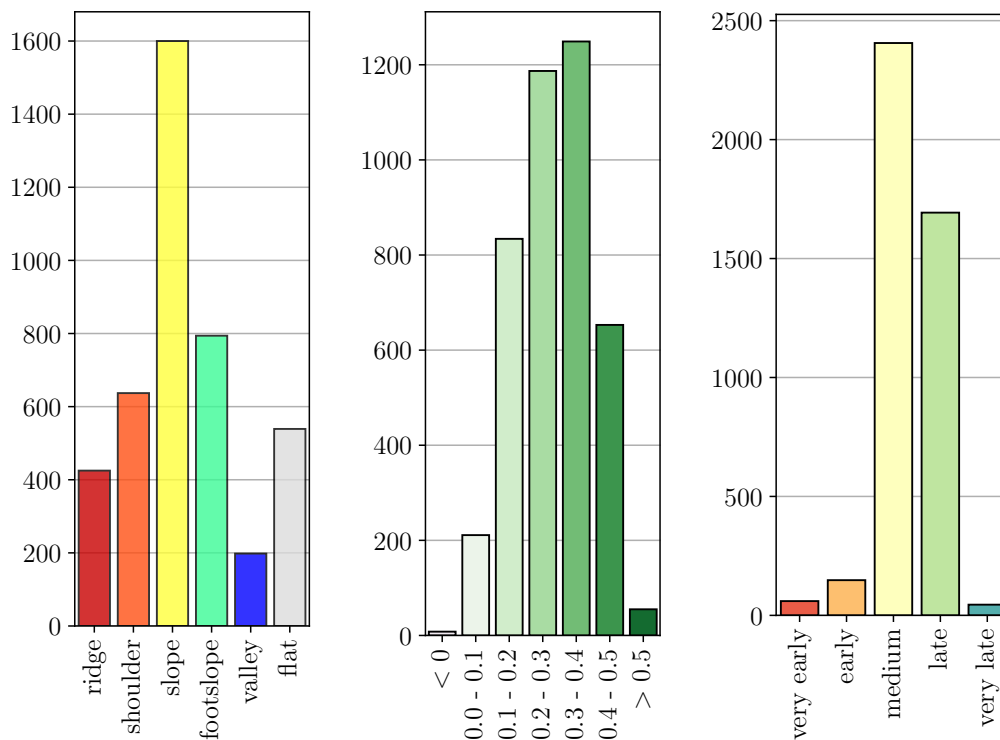


Figure B.4: Sample size per surface property class in the Bayelva basin- Number of randomly sampled points in the periglacial core DEM area for terrain forms (left), vegetation cover (center), and timing of snow disappearance (right).

B.2.2 Simplification of terrain forms

The Geomorphons tool (Jasiewicz and Stepinski 2013) originally created ten terrain forms visualised in Figure B.5. As the peak, shoulder, and pit classes were very small, I decided to simplify the Geomorphon classification by merging similar classes as described in section A.7.1. Due to reasons of consistency, I merged the hollow and footslope classes although they were sufficiently large to be meaningful

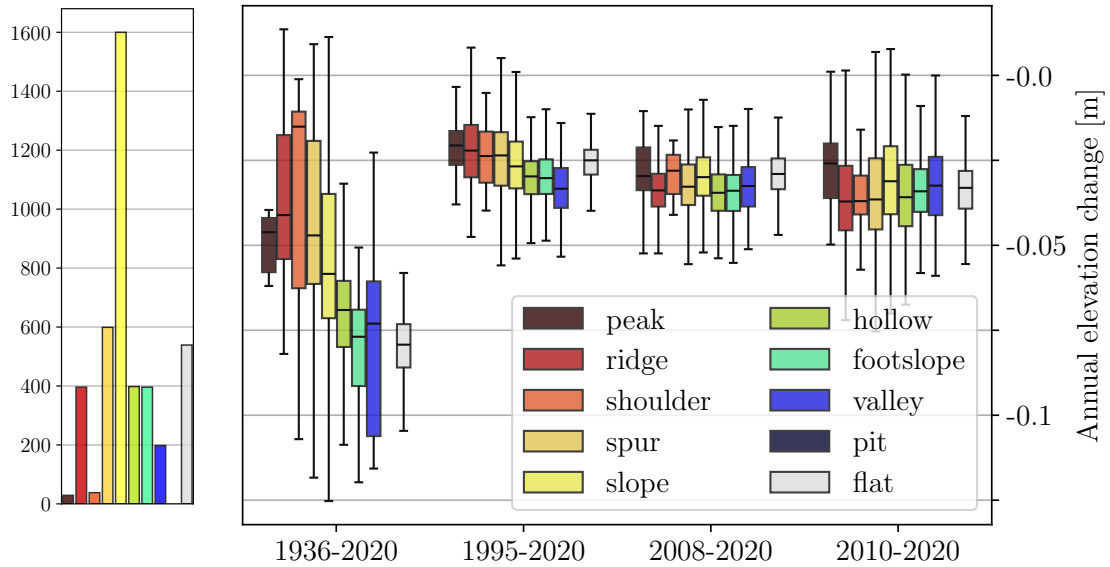


Figure B.5: Elevation change across terrain forms before simplification - Sample sizes (left) and and elevation changes for DEM differences (right) for the original ten terrain forms (*Geomorphons tool by Jasiewicz and Stepinski (2013)*).

by themselves. In this case, the simplification concealed the individual signals of the two classes that can be retraced in Figure B.5. The hollow and footslope forms showed similar subsidence trends in the 1995 and 2008 DEM differencing results. Footslopes showed more subsidence than hollow forms in the 1936 DEM, but slightly less subsidence in the 2010 DEM.

B.2.3 Elevation change statistics across surface properties

Tables B.4, B.5, and B.6 provide spatial statistics on elevation change across terrain forms, vegetation cover classes, and snow disappearance timing referred to in Section 4.2 and visualised in Figure 5.

Table B.4: Statistics of periglacial subsidence results across terrain forms in the Bayelva basin - Sample count, median, mean, standard deviation, minimum, and maximum for each terrain form (geomorphon) and DEM differencing period.

Terrain form	Period	Elevation change statistics [m/year]					
		count	median	mean	std	min	max
ridge/peak	1936-2020	425	-0.042	-0.038	0.024	-0.160	0.014
	1995-2020	425	-0.022	-0.021	0.014	-0.055	0.057
	2008-2020	425	-0.034	-0.033	0.008	-0.056	-0.006
	2010-2020	425	-0.037	-0.035	0.016	-0.117	0.034
shoulder/spur	1936-2020	637	-0.046	-0.043	0.030	-0.178	0.009
	1995-2020	637	-0.024	-0.024	0.014	-0.068	0.081
	2008-2020	637	-0.033	-0.032	0.009	-0.056	-0.003
	2010-2020	637	-0.037	-0.034	0.016	-0.075	0.034
slope	1936-2020	1600	-0.058	-0.054	0.024	-0.153	0.011
	1995-2020	1600	-0.027	-0.026	0.012	-0.080	0.048
	2008-2020	1600	-0.030	-0.030	0.009	-0.087	0.004
	2010-2020	1600	-0.031	-0.031	0.015	-0.090	0.049
footslope/hollow	1936-2020	794	-0.074	-0.074	0.022	-0.156	-0.007
	1995-2020	794	-0.030	-0.030	0.009	-0.075	0.008
	2008-2020	794	-0.034	-0.035	0.008	-0.078	-0.008
	2010-2020	794	-0.035	-0.034	0.013	-0.091	0.017
valley/pit	1936-2020	198	-0.073	-0.079	0.025	-0.116	-0.023
	1995-2020	198	-0.033	-0.033	0.009	-0.071	0.005
	2008-2020	198	-0.033	-0.033	0.008	-0.056	-0.006
	2010-2020	198	-0.032	-0.032	0.013	-0.059	0.024
flat	1936-2020	539	-0.079	-0.080	0.012	-0.141	-0.058
	1995-2020	539	-0.025	-0.026	0.006	-0.048	-0.001
	2008-2020	539	-0.029	-0.029	0.007	-0.057	-0.010
	2010-2020	539	-0.033	-0.034	0.010	-0.096	0.011

Table B.5: Statistics of periglacial subsidence results for different vegetation index values in the Bayelva basin - Sample count, median, mean, standard deviation, minimum, and maximum for binned vegetation index (NDVI) values and DEM differencing period.

NDVI	Period	Elevation change statistics [m/year]					
		count	median	mean	std	min	max
<0	1936-2020	8	-0.093	-0.094	0.013	-0.115	-0.073
	1995-2020	8	-0.032	-0.033	0.011	-0.055	-0.022
	2008-2020	8	-0.039	-0.042	0.015	-0.078	-0.028
	2010-2020	8	-0.034	-0.038	0.024	-0.091	-0.014
0.0-0.1	1936-2020	211	-0.066	-0.062	0.026	-0.134	-0.001
	1995-2020	211	-0.029	-0.030	0.015	-0.071	0.057
	2008-2020	211	-0.033	-0.032	0.010	-0.061	0.004
	2010-2020	211	-0.033	-0.032	0.020	-0.117	0.036
0.1-0.2	1936-2020	834	-0.065	-0.061	0.028	-0.170	0.008
	1995-2020	834	-0.028	-0.028	0.012	-0.066	0.047
	2008-2020	834	-0.030	-0.030	0.009	-0.087	-0.005
	2010-2020	834	-0.033	-0.032	0.014	-0.082	0.024
0.2-0.3	1936-2020	1187	-0.064	-0.058	0.028	-0.178	0.014
	1995-2020	1187	-0.025	-0.025	0.010	-0.066	0.049
	2008-2020	1187	-0.031	-0.031	0.008	-0.057	-0.002
	2010-2020	1187	-0.033	-0.033	0.013	-0.098	0.030
0.3-0.4	1936-2020	1249	-0.061	-0.058	0.027	-0.164	0.014
	1995-2020	1249	-0.026	-0.026	0.011	-0.080	0.081
	2008-2020	1249	-0.033	-0.032	0.008	-0.063	0.001
	2010-2020	1249	-0.034	-0.034	0.014	-0.096	0.049
0.4-0.5	1936-2020	653	-0.060	-0.059	0.027	-0.148	0.010
	1995-2020	653	-0.028	-0.026	0.011	-0.054	0.048
	2008-2020	653	-0.032	-0.033	0.010	-0.068	-0.006
	2010-2020	653	-0.033	-0.032	0.015	-0.076	0.034
>0.5	1936-2020	55	-0.073	-0.073	0.024	-0.112	-0.029
	1995-2020	55	-0.028	-0.027	0.011	-0.060	-0.002
	2008-2020	55	-0.032	-0.033	0.010	-0.056	-0.015
	2010-2020	55	-0.034	-0.033	0.013	-0.055	-0.003

Table B.6: Statistics of periglacial subsidence results across snow disappearance classes in the Bayelva basin - Sample count, median, mean, standard deviation, minimum, and maximum for each snow disappearance class and DEM differencing period.

Snow disappearance	Period	Elevation change statistics [m/year]					
		count	median	mean	std	min	max
very early	1936-2020	60	-0.038	-0.036	0.029	-0.111	0.011
	1995-2020	60	-0.015	-0.012	0.020	-0.045	0.047
	2008-2020	60	-0.031	-0.031	0.008	-0.051	-0.011
	2010-2020	60	-0.029	-0.026	0.018	-0.072	0.033
early	1936-2020	148	-0.046	-0.044	0.029	-0.140	0.014
	1995-2020	148	-0.020	-0.019	0.016	-0.057	0.081
	2008-2020	148	-0.032	-0.032	0.008	-0.053	-0.011
	2010-2020	148	-0.029	-0.028	0.016	-0.079	0.013
medium	1936-2020	2406	-0.063	-0.058	0.028	-0.178	0.014
	1995-2020	2406	-0.026	-0.026	0.010	-0.080	0.057
	2008-2020	2406	-0.032	-0.032	0.009	-0.068	0.004
	2010-2020	2406	-0.034	-0.033	0.014	-0.117	0.049
late	1936-2020	1693	-0.066	-0.063	0.026	-0.170	0.012
	1995-2020	1693	-0.028	-0.028	0.012	-0.075	0.049
	2008-2020	1693	-0.032	-0.032	0.010	-0.133	0.001
	2010-2020	1693	-0.034	-0.033	0.015	-0.133	0.036
very late	1936-2020	45	-0.069	-0.064	0.027	-0.112	-0.007
	1995-2020	45	-0.034	-0.032	0.019	-0.086	0.039
	2008-2020	-	-	-	-	-	-
	2010-2020	45	-0.039	-0.042	0.030	-0.129	0.020

B.3 Surface classifications on the Brøgger peninsula

B.3.1 Spatial distribution and coverage of the classes

Figure B.6 shows the spatial distribution and coverage of the surface classes that I compared across regions of the Brøgger peninsula (section 4.3). I excluded the southern peninsula due to its data quality and compared the Kvadehuksletta, the northern peninsula and the Bayelva basin to each other with Bayelva being a sub-region of the northern peninsula. While I sampled the whole footprint of the 2020 DEM for the landscape comparisons (Fig. 6), I focused the analysis of the surface characteristics on periglacial terrain and only compared the core DEM area to the other subregions (see Fig. B.6). The terrain form classification covered the periglacial landscape peninsula-wide, while vegetation and snow classifications were spatially limited due to data qualities (see section 3.3).

B.3.2 Sample size per surface property class on the Brøgger peninsula

The regions showed different distribution patterns of surface properties that are outlined by Figure B.7. While the terrain of the Bayelva basin and the rest of the northern peninsula was dominated by slopes, the Kvadehuksletta was predominantly flat. Valleys made up the smallest terrain class throughout the regions. All regions also showed almost exclusively positive NDVI values. The Bayelva basin appeared to be slightly more and the Kvadehuksletta slightly less vegetated than the northern peninsula. Medium snow disappearance was the largest snow disappearance class throughout the regions. But while snow disappearance was predominantly medium or late in the Bayelva basin, there were much more samples with very early and early snow disappearance on the Kvadehuksletta and on the northern peninsula. Very late and late snow disappearance was rare on the Kvadehuksletta but common on the northern peninsula.

B.3.3 Elevation change statistics across surface properties

Tables B.7, B.8, B.9, and B.10 provide spatial statistics on elevation change (1936-2010) on the Brøgger peninsula across landscapes terrain forms, vegetation cover classes, and snow disappearance timing referred to in Section 4.3 and visualised in Figures 7 and B.6.

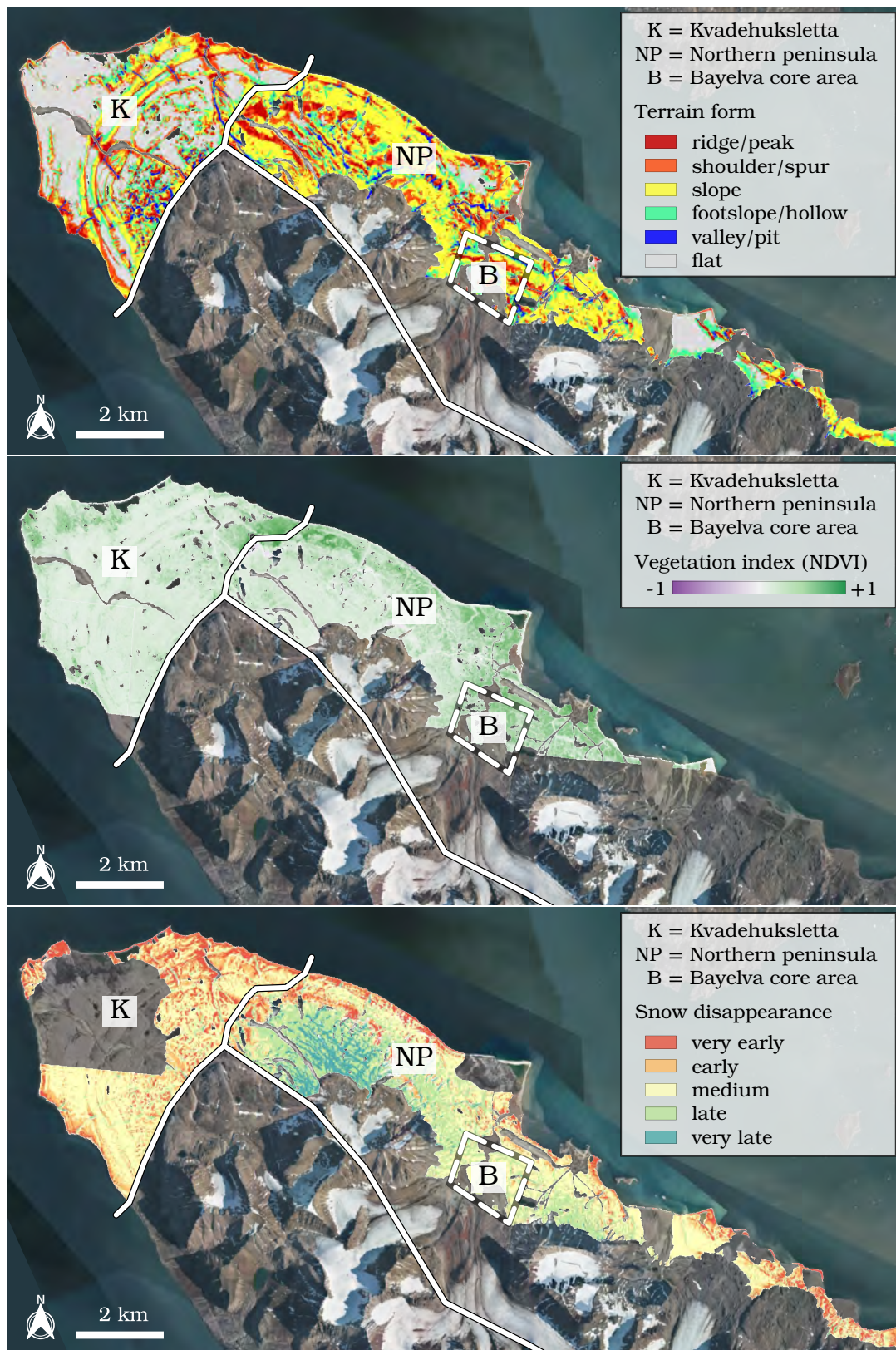


Figure B.6: Surface classification maps for the Brøgger peninsula -Classified terrain forms (top), NDVI (center), and snow disappearance timing (bottom) for periglacial areas on the Kvadehuksletta (K), the northern peninsula (NP), and the Bayelva core area (B). Please note that vegetation index and snow disappearance classification do not cover the whole periglacial terrain due to data gaps. (Terrain forms based on Jasiewicz and Stepinski (2013) and Norwegian Polar Institute (2014a), NDVI and snow cover derived from Planet Labs PBC (2023)).

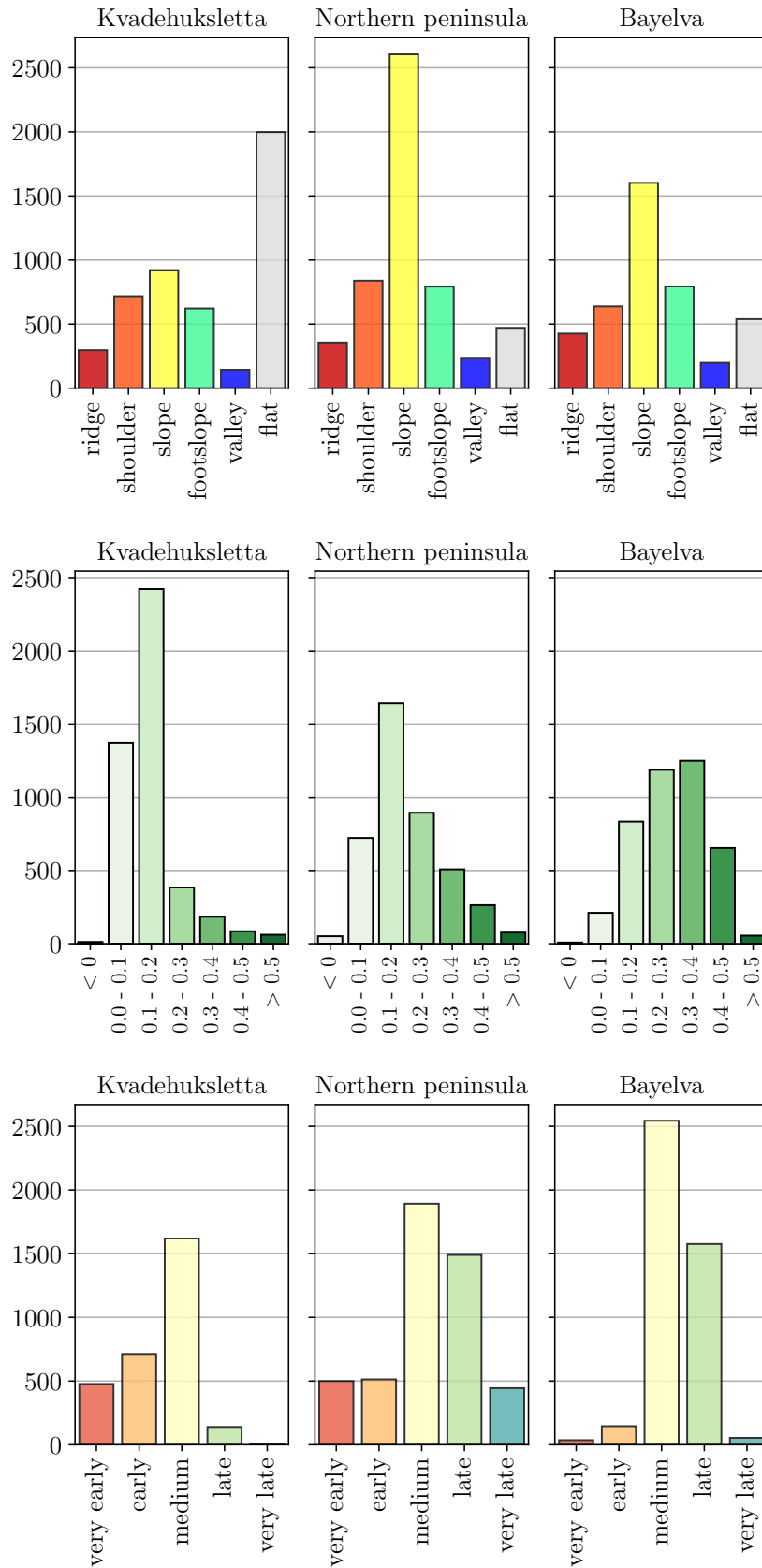


Figure B.7: Sample size per surface property class on the Brøgger peninsula - Number of randomly sampled points in periglacial areas on the Kvadehuksletta, the northern peninsula, and the Bayelva basin for terrain forms (left), NDVI (center), and snow disappearance timing (right).

Table B.7: Statistics of general elevation change results on the Brøgger peninsula - Sample count, median, mean, standard deviation, minimum, and maximum for each landscape and region during the DEM differencing period of 1936-2010.

Landscape	Region	Elevation change statistics [m/year]					
		count	median	mean	std	min	max
Periglacial	Bayelva	4448	-0.052	-0.057	0.066	-0.874	0.036
	Kvadehuksletta	2437	-0.046	-0.047	0.017	-0.191	0.017
	North	2817	-0.038	-0.042	0.102	-1.296	0.302
River beds	Bayelva	1143	-0.075	-0.100	0.075	-0.514	-0.037
	Kvadehuksletta	57	-0.050	-0.050	0.009	-0.069	-0.018
	North	380	-0.034	-0.061	0.107	-0.871	0.024
Anthropogenic	Bayelva	262	-0.005	-0.012	0.027	-0.087	0.037
	Kvadehuksletta	0	-	-	-	-	-
	North	98	-0.041	-0.033	0.029	-0.100	0.029
Moraines	Bayelva	3163	-1.041	-0.966	0.266	-1.435	-0.113
	Kvadehuksletta	0	-	-	-	-	-
	North	1847	-0.374	-0.485	0.397	-1.393	0.212
Glaciers	Bayelva	984	-1.047	-1.055	0.081	-1.349	-0.900
	Kvadehuksletta	0	-	-	-	-	-
	North	2364	-0.344	-0.434	0.313	-1.607	0.254

Table B.8: Statistics of periglacial subsidence results across terrain forms on the Brøgger peninsula - Sample count, median, mean, standard deviation, minimum, and maximum for terrain form classes (geomorphons) and region during the DEM differencing period of 1936-2010.

Terrain form	Region	Elevation change statistics [m/year]					
		count	median	mean	std	min	max
ridge/peak	Bayelva	426	-0.029	-0.022	0.029	-0.166	0.037
	Kvadehuksletta	296	-0.039	-0.042	0.019	-0.139	-0.007
	Northern peninsula	357	-0.029	-0.021	0.082	-1.270	0.270
shoulder/spur	Bayelva	638	-0.033	-0.028	0.036	-0.197	0.030
	Kvadehuksletta	717	-0.043	-0.045	0.019	-0.130	0.008
	Northern peninsula	839	-0.032	-0.024	0.074	-1.159	0.278
slope	Bayelva	1602	-0.047	-0.042	0.028	-0.165	0.031
	Kvadehuksletta	921	-0.040	-0.044	0.023	-0.227	0.014
	Northern peninsula	2605	-0.036	-0.032	0.062	-1.110	0.256
footslope/hollow	Bayelva	794	-0.065	-0.064	0.025	-0.167	0.012
	Kvadehuksletta	622	-0.045	-0.049	0.020	-0.239	-0.009
	Northern peninsula	793	-0.045	-0.070	0.180	-1.284	0.177
valley/pit	Bayelva	198	-0.064	-0.069	0.028	-0.107	-0.005
	Kvadehuksletta	144	-0.047	-0.052	0.019	-0.127	-0.008
	Northern peninsula	237	-0.054	-0.077	0.132	-0.836	0.070
flat	Bayelva	539	-0.072	-0.073	0.014	-0.150	-0.042
	Kvadehuksletta	1998	-0.049	-0.050	0.015	-0.099	-0.008
	Northern peninsula	471	-0.036	-0.057	0.128	-1.309	0.021

Table B.9: Statistics of periglacial subsidence results for different vegetation index values on the Brøgger peninsula - Sample count, median, mean, standard deviation, minimum, and maximum for binned vegetation index (NDVI) values and region during the DEM differencing period of 1936-2010.

NDVI	Region	Elevation change statistics [m/year]					
		count	median	mean	std	min	max
<0	Bayelva	8	-0.085	-0.085	0.014	-0.103	-0.061
	Kvadehuksletta	12	-0.093	-0.109	0.068	-0.227	-0.027
	Northern peninsula	51	-0.031	-0.026	0.116	-0.441	0.272
0.0-0.1	Bayelva	211	-0.059	-0.053	0.029	-0.149	0.020
	Kvadehuksletta	1369	-0.044	-0.045	0.018	-0.239	-0.010
	Northern peninsula	722	-0.043	-0.041	0.084	-0.802	0.241
0.1-0.2	Bayelva	834	-0.055	-0.051	0.033	-0.189	0.034
	Kvadehuksletta	2423	-0.044	-0.045	0.016	-0.130	0.014
	Northern peninsula	1642	-0.040	-0.031	0.046	-0.225	0.278
0.2-0.3	Bayelva	1187	-0.053	-0.046	0.033	-0.197	0.037
	Kvadehuksletta	384	-0.056	-0.056	0.016	-0.106	-0.003
	Northern peninsula	894	-0.042	-0.035	0.041	-0.150	0.131
0.3-0.4	Bayelva	1249	-0.049	-0.045	0.032	-0.174	0.036
	Kvadehuksletta	184	-0.058	-0.062	0.018	-0.100	-0.023
	Northern peninsula	508	-0.039	-0.034	0.041	-0.120	0.139
0.4-0.5	Bayelva	653	-0.047	-0.046	0.031	-0.146	0.032
	Kvadehuksletta	85	-0.074	-0.071	0.020	-0.098	-0.031
	Northern peninsula	263	-0.055	-0.049	0.037	-0.133	0.100
>0.5	Bayelva	55	-0.065	-0.062	0.028	-0.104	-0.007
	Kvadehuksletta	61	-0.084	-0.078	0.016	-0.099	-0.022
	Northern peninsula	76	-0.074	-0.068	0.026	-0.104	0.053

Table B.10: Statistics of periglacial subsidence results across snow disappearance classes on the Brøgger peninsula - Sample count, median, mean, standard deviation, minimum, and maximum for each snow disappearance class and region during the DEM differencing period of 1936-2010.

Landscape	Region	Elevation change statistics [m/year]					
		count	median	mean	std	min	max
very early	Bayelva	36	-0.013	-0.017	0.030	-0.064	0.032
	Kvadehuksletta	477	-0.061	-0.062	0.025	-0.239	-0.007
	Northern peninsula	500	-0.028	-0.035	0.074	-0.494	0.182
early	Bayelva	146	-0.030	-0.028	0.033	-0.143	0.034
	Kvadehuksletta	713	-0.049	-0.050	0.021	-0.143	0.008
	Northern peninsula	513	-0.029	-0.024	0.062	-0.170	0.278
medium	Bayelva	2543	-0.052	-0.047	0.033	-0.197	0.037
	Kvadehuksletta	1619	-0.043	-0.046	0.019	-0.112	0.014
	Northern peninsula	1892	-0.034	-0.034	0.059	-0.836	0.270
late	Bayelva	1576	-0.055	-0.051	0.030	-0.189	0.034
	Kvadehuksletta	140	-0.047	-0.049	0.019	-0.139	-0.016
	Northern peninsula	1490	-0.039	-0.031	0.046	-0.441	0.183
very late	Bayelva	54	-0.053	-0.050	0.026	-0.098	-0.004
	Kvadehuksletta	3	-0.052	-0.051	0.019	-0.070	-0.032
	Northern peninsula	444	-0.044	-0.049	0.078	-0.802	0.151

Erklärung

Ich erkläre, dass ich die vorliegende Arbeit oder Teile davon nicht für andere Prüfungs- und Studienleistungen eingereicht, selbständig und nur unter Verwendung der angegebenen Literatur und Hilfsmittel angefertigt habe. Sämtliche fremde Quellen inklusive Internetquellen, Grafiken, Tabellen und Bilder, die ich unverändert oder abgewandelt wiedergegeben habe, habe ich als solche kenntlich gemacht. Mir ist bekannt, dass Verstöße gegen diese Grundsätze als Täuschungsversuch bzw. Täuschung geahndet werden.

Berlin, den